Universität Stuttgart
5. Physikalisches Institut

# An Atomic Faraday Filter as a Beam Splitter for Photon Pairs

Ioannis Caltzidis

Masterarbeit

21.Oktober.2019
Hauptberichter: Prof. Dr. Tilman Pfau
Mitberichter: Prof. Dr. Martin Dressel

# Declaration

I declare that this thesis was written by myself independently. It does not contain any material previously submitted by myself for a degree in this or any other university.

I also declare that I did not use outside content in the process of creating this thesis other than cited.

I clearly marked and separately listed all of the literature and all of the other sources which I employed when producing this work, either literally or in content.

Stuttgart, October 21, 2019 Ioannis Caltzidis

# Abstract

The generation of heralded single photons in hot atomic vapours via a four-wave mixing (FWM) process has been demonstrated. Other efforts to increase yield in such systems involve the use of hollow-core micro-structured fibres. This method delivers a significantly higher efficency. However, the two photons overlap due to their generation in the fibre and are very close in frequency to each other. Therefore it is difficult to spatially separate them with common tools such as interference filters.

For this purpose a scheme was identified using an atomic vapour in the hyperfine Paschen-Back regime as a highly dispersive beam splitter for the photon pairs. In the scope of this thesis, *ElecSus* and an optimisation module of *Scipy* are used to find the most favourable working conditions for the scheme. The required high magnetic fields in the order of 7 kG made it necessary to use two custom designed top head magnets with opposing polarisation in close proximity to the cell. The effects of inhomogeneity in the magnetic field on the resulting spectra are briefly discussed and shown to be negligible. The resulting beam splitter is characterised in terms of stability and shows high performance with a wide range of tunability. This makes it an interesting tool for other narrow band applications and where low loss components are essential.

# Zusammenfassung

Die Erzeugung von angekündigten Einzelphotonen in heißen atomaren Dämpfen durch ein Vierwellenmischverfahren (FWM) wurde bereits nachgewiesen. Weitere Versuche die Ausbeuten solcher Systeme zu steigern liefen über die Verwendung mikrostrukturierter Hohlkernfasern. Diese Methode liefert eine deutlich höhere Effizienz, die beiden Photonen überschneiden sich jedoch räumlich aufgrund ihrer Entstehung in der Faser und ihre Wellenlängen liegen sehr nahe beieinander. Daher ist es schwierig, sie mit gängigen Werkzeugen wie Interferenzfiltern räumlich zu trennen.
Zu diesem Zweck wurde ein Schema mit einem atomaren Dampf im hyperfeinen Paschen-Back-Regime als hochdispersem Strahlteiler für die Photonenpaare identifiziert. Darüber hinaus wurden, im Rahmen dieser Thesis, *ElecSus* und ein Optimierungsmodul von *Scipy* verwendet, um die günstigsten Arbeitsbedingungen für das System zu finden. Die erforderlichen hohen Magnetfelder in der Größenordnung von 7 kG machten es notwendig, zwei maßgeschneiderte Permanentmagnete mit entgegengesetzter Polarität in unmittelbarer Nähe der Zelle zu verwenden.
Der daraus resultierende Strahlteiler wurde durch Stabilitätsmessungen charakterisiert und zeigt eine hohe Leistung mit einem breiten Spektrum an Stimmbarkeit. Dies macht ihn zu einem interessanten Werkzeug für andere Schmalbandanwendungen, bei denen verlustarme Komponenten unerlässlich sind.

# Contents

# About this thesis

The aim of this thesis is to demonstrate the feasibility of an atomic Faraday filter as a beam splitter for photon pairs. The thesis consists of 9 chapters.

**Chapter 1** contains a short introduction into atomic vapours and continues with a clarification of the terminology *'Heralded single photon sources'* as well as a very short excursion to four-wave mixing (FWM) and the advantages of an atomic Faraday filter over bandpass and interference filters.

**Chapter 2** aims to link the macroscopic effect of light propagating through a medium with the microscopic quantum phenomena via the electric susceptibility.

**Chapter 3** introduces and explains the Faraday effect, which is exploited in this thesis to realise the atomic Faraday beam splitter.

**Chapter 4** exhibits the tools (experimental and conceptual) used to design and test the Faraday filter.

**Chapter 5** shows how computational optimisation is used to design the best possible atomic vapour to accommodate the atomic Faraday beam splitter.

**Chapter 6** introduces the experimental apparatus used to produce and stabilise the magnetic field and temperature necessary for the operation of the atomic Faraday beam splitter.

**Chapter 7** exhibits and discusses the spectroscopic results acquired. Furthermore a stability estimate is performed and analysed to testify the long term reliability of the atomic Faraday beam splitter.

**Chapter 8** summarises the content of this thesis and gives an outlook into further optimisation and use case possibilities.

**Chapter 9** provides supplemental material.

# 1 Motivation

Hot atomic vapours have been used in numerous optical applications for example in hybrid quantum systems [1, 2], where narrow band filters are of interest [3] , in the realisation of macroscopic entanglement [4], in off-resonant frequency stabilisation [5, 6] and many more. The focus of this thesis is the realisation of an atomic Faraday filter as a beam splitter for photon pairs generated by a four-wave mixing (FWM) process in a hollow-core fibre, which can be used as a heralded single photon source.

## 1.1 Heralded single photon sources

Heralded single photon sources are devices that produce correlated photon pairs. The photon pair generation in such sources is not on demand. However, the produced photons are correlated in time. Such single photon sources are very useful in timing sensitive experiments or for improvements in secure telecommunication [7, 8]. Different methods and systems exist to generate single photons like quantum dots [1, 9] and colour centers in diamonds [10] and more. All of them, on demand or heralded, have their advantages and disadvantages in terms of accessibility, purity and intensity. One of the methods is four-wave mixing in rubidium vapours[11, 12, 13].

## 1.2 Four-wave mixing

In this system an intense laser is directed at a rubidium vapour cell. While the light propagates it forces a non-linear response from the medium. In this non-linearity two photons experience a parametric process as depicted in figure 1.1. The photons converted

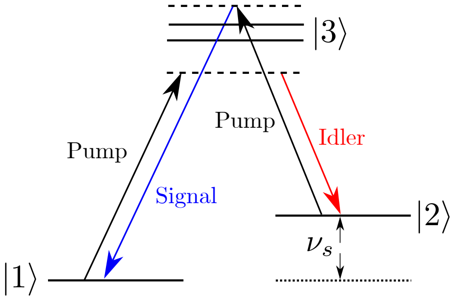

Figure 1.1: Energy level scheme of a FWM process in an atomic rubidium vapour at the $D_1$-line. Idler and signal are separated by two times the ground state splitting of either $^{85}$Rb ($\nu_s = 6.8\,\mathrm{GHz}$) or $^{87}$Rb ($\nu_s = 3.0\,\mathrm{GHz}$).

by this method (signal and idler) will be separated in frequency by two times the ground state splitting. The absolute frequency of the produced photons is tunable by changing the detuning of the pump laser. The phase matching condition $\boldsymbol{k}_p^1 + \boldsymbol{k}_p^2 = \boldsymbol{k}_s + \boldsymbol{k}_i$, where $\boldsymbol{k}_p^1$ and $\boldsymbol{k}_p^2$ are the wavevectros of the pump photons, determines the propagation direction of the produced photon pairs (wavevector $\boldsymbol{k}_s$ and $\boldsymbol{k}_i$) [14]. By placing optics in one of the possible paths defined by the phase matching condition this process can be harnessed to create a heralded single photon source. However, the placement of the optics in itself preselects and limits the amount of usable photons.

A way to increase yields is to introduce a hollow core fibre, in which FWM can take place [12, 13]. The fibre will accumulate the converted photons and guide them along the pump laser propagation axis. The spatial separation, however, is not maintained any more. A device is needed to facilitate the separation of the photon pairs. Available solutions like band pass filters or interference filters are unfortunately not narrow enough, or reject one of the photons, which complicates the experimental setup and introduces losses. In the search for a suitable system, atomic Faraday filters made from rubidium vapour cells, seemed to provide the most promise.

## 1.3 Advantages of the atomic Faraday filter

The advantages of the atomic Faraday filter are, that it introduces only a minimal amount of additional optics in the path of the photon pair, ideally just the vapour cell. Also important is the fact that the photons produced by the FWM device described in section 1.2 are already in the scope of the rubidium $D_1$-line. This has the effect, that a rubidium based atomic Faraday filter can be deployed without any concern towards compatibility.

With the appearence of open scource software like *scipy* [15] and computational tools like *ElecSus* [16, 17] the possibility of computational optimisation for such systems became accessible. This pushes the competitiveness of vapour based devices for use cases where high transmission and narrowband characteristics are of essence. This thesis utilises these advantages to design a tailored atomic Faraday filter as a beam splitter for photon pairs.

# 2 Light propagation through a medium

Atomic media are subjects of thorough studies and a lot of the underlying theories have already been discussed in numerous publications. This chapter is therefore closely orientated towards [18] and [19] and aims to establish a link between the macroscopic phenomenology of light propagating through a medium and the quantum mechanical description of atomic transitions. This is achieved by describing the problem classically at first and using a simple two level system as an introduction into the quantum world. The implications for more complex atomic systems, as well as the effects of temperature to the medium, will also be briefly discussed.

## 2.1 Beer–Lambert law

The Beer–Lambert law describes the dampening effect a medium has on the transmission of monochromatic light. To understand the origin of this effect, the influence of a medium on a monochromatic plane light wave will be investigated. The wave can be written as

$$\boldsymbol{E}\left(z,t\right) = \boldsymbol{E}_0 \cdot e^{i(kz-\omega t)}, \tag{2.1}$$

where $z$ describes the propagation direction, $\omega$ the angular frequency and $k$ the wave number. $\boldsymbol{E}_0$ describes a polarisation and amplitude which lies in the xy-plane (perpendicular to the propagation direction $z$). Is is a solution to Maxwell's wave equation [20] and a sufficient approximation to the Gaussian laser beams used in this thesis [18, 21]. The wave number in a medium can be calculated by[22],

$$k = n_c \cdot k_0, \tag{2.2}$$

where $k_0$ represents the wave number in vacuum with

$$n_c = n + i\beta. \tag{2.3}$$

The real part of $n_c$ is the refractive index $n = c/v_p$ where $v_p$ is the phase velocity of the light in a medium and $c$ is the speed of light in vacuum. $\beta$ is the imaginary part and contains information about the effect of the medium on the phase of the light. Combining the equations (2.1) and (2.2), we get

$$\boldsymbol{E}\left(z,t\right) = \boldsymbol{E}_0 \cdot e^{-\beta k_0 z} e^{i(nk_0 z-\omega t)}. \tag{2.4}$$

The use of a complex refractive index reveals an attenuation $e^{-\beta k_0 z}$ and an induced phase shift $\Delta\phi = (1-n) \cdot k_0 z$ of the travelling light by the medium compared to light travelling through vacuum. The transmission of the light through the medium with the length $l$ is given by

$$T = \frac{I}{I_0} = \frac{\left|E\left(l, t_1\right)\right|^2}{\left|E\left(0, t_0\right)\right|^2} = e^{-2\beta k_0 l}. \tag{2.5}$$

For dispersive media $n_c$ is a function of the frequency $n_c\left(\omega\right)$. This implies that the phase velocity,

$$v_p = \frac{\omega}{k}, \tag{2.6}$$

changes for light with different $\omega$. Any two light waves with different frequencies $\omega_1$ and $\omega_2$ experience different retardations and thus a phase shift

$$\Delta\phi' = \left(n\left(\omega_1\right) - n\left(\omega_2\right)\right) \cdot k_0 z. \tag{2.7}$$

If the medium is atomic, then the dispersive behaviour occurs only around atomic transitions. Therefore the attenuation factor $\alpha = 2\beta k_0$ can also be written as

$$\alpha = \epsilon\left(\Delta\right) c\left(T\right), \tag{2.8}$$

where $\epsilon\left(\Delta\right)$ represents the dispersive absorptivity and $c\left(T\right)$ the temperature dependant density of the medium. The detuning $\Delta$ refers to a frequency difference between a convenient 0 point (often near atomic transitions) and the frequency $\omega$ of the incident light.

## 2.2 The two-level atom

To gain a better understanding of the dependencies in equation (2.8) we consider an atom with exactly two levels. The ground state $|g\rangle$ and the excited state $|e\rangle$, as shown in figure 2.1.

The two states are separated by the energy $\mathcal{E} = \hbar \cdot \omega_0$. When a resonant electromagnetic wave interacts with this two level atom, an electron can be coherently excited from the ground into the excited state $|g\rangle \rightarrow |e\rangle$.

After a finite amount of time the electron returns to the ground state by emitting a photon. Due to the probabilistic nature of the lifetime of the excited state this process is best described by a decay rate $\Gamma$. It is important to keep in mind, that the spontaneous decay is a de-coherent process and thus introduces dephasing into the system.

Another atomic transition case is the stimulated emission. In this scenario an excited atom emits a photon in the presence of a light field coherently and the decay of the excited state takes place faster than the spontaneous emission. In regimes with high laser powers the electron cannot stay at the ground manifold since it will once again get

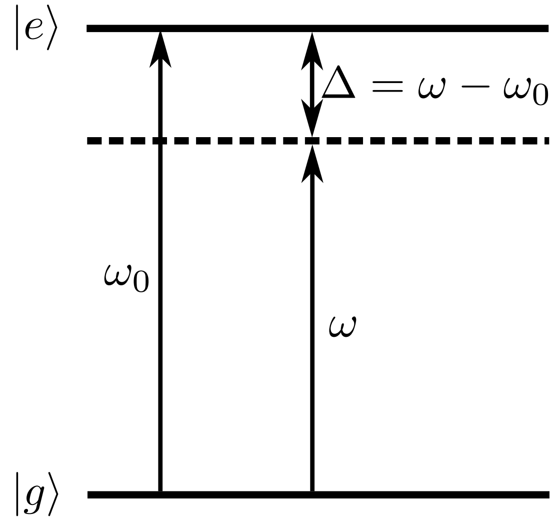

Figure 2.1: Energy level scheme of a two level atom with the indicated transition frequency $\omega_0$, the incident light frequency $\omega$ and the resulting detuning $\Delta$. The ground state is introduced as $|g\rangle$ and the excited state as $|e\rangle$.

excited by the light field. The electron therefore starts to oscillate between $|g\rangle$ and $|e\rangle$ with the Rabi frequency

$$\Omega = -\frac{d \cdot E_0}{\hbar}, \tag{2.9}$$

where $d$ describes the electric dipole moment and $E_0$ the electric field of the incident electromagnetic wave. This oscillation does not continue indefinitely, since ultimately the dephasing introduced by the spontaneous decay dampens the oscillations in an atomic ensemble.

In the density matrix formalism the interaction between light and a two-level system is described by population and coherence changes of the two level system [19, 23]. The optical Bloch equations [19, 24] describe the time evolution of the populations and coherences for the interaction Hamiltonian $\hat{\boldsymbol{H}}_{int} = -\hat{\boldsymbol{d}} \cdot \boldsymbol{E}$ (here $\boldsymbol{E}$ describes the classical electric field) within the rotating-wave approximation,

$$\begin{aligned}
\dot{\rho}_{gg} &= \frac{i\Omega}{2} \cdot (\tilde{\rho}_{ge} - \tilde{\rho}_{eg}) + \rho_{ee}\Gamma, \\
\dot{\tilde{\rho}}_{ge} &= \frac{i\Omega}{2} \cdot (\rho_{gg} - \rho_{ee}) + \tilde{\rho}_{ge}\left(-i\Delta - \frac{\Gamma}{2}\right), \\
\dot{\tilde{\rho}}_{eg} &= \frac{i\Omega}{2} \cdot (\rho_{ee} - \rho_{gg}) + \tilde{\rho}_{eg}\left(i\Delta - \frac{\Gamma}{2}\right), \\
\dot{\rho}_{ee} &= \frac{i\Omega}{2} \cdot (\tilde{\rho}_{eg} - \tilde{\rho}_{ge}) - \rho_{ee}\Gamma.
\end{aligned} \tag{2.10}$$

The coherences are defined as $\tilde{\rho}_{ge} = \rho_{ge}e^{-i\omega t}$ and $\tilde{\rho}_{eg} = \rho_{eg}e^{i\omega t}$. The steady-state solutions provide a suitable case study, where $\dot{\rho}_{gg} = \dot{\tilde{\rho}}_{ge} = \dot{\tilde{\rho}}_{eg} = \dot{\rho}_{ee} = 0$ [18, 25]. Furthermore, the system is considered to be closed, therefore $\rho_{gg}+\rho_{ee} = 1$ and $\dot{\rho}_{gg}+\dot{\rho}_{ee} = 0$. Since the subject of this thesis resides in the weak probe regime [26] the population changes in the atomic system can be neglected. Therefore $\rho_{gg} = 1$ and $\rho_{ee} = 0$. A solution of the optical Bloch equations is then given by

$$\tilde{\rho}_{ge}^{\dagger} = \tilde{\rho}_{eg} = -\frac{i\Omega/2}{\Gamma/2 - i\Delta}. \tag{2.11}$$

The atomic two level system can now be described by the expectation value of the dipole operator $\langle\hat{\boldsymbol{d}}\rangle$. Again the density matrix formalism provides a comprehensive way to do so [23],

$$\langle\hat{\boldsymbol{d}}\rangle = \mathrm{Tr}\left(\hat{\boldsymbol{d}}\hat{\boldsymbol{\rho}}\right) = \boldsymbol{d}_{ge}\left(\rho_{ge} + \rho_{eg}\right) = \boldsymbol{d}_{ge}\left[\tilde{\rho}_{ge}e^{i\omega t} + \tilde{\rho}_{eg}e^{-i\omega t}\right]. \tag{2.12}$$

The diagonal matrix elements of $\boldsymbol{d}$ are 0 [23] and the expectation value is now written as $\langle g|\,\hat{\boldsymbol{d}}\,|e\rangle = \boldsymbol{d}_{ge} = \boldsymbol{d}_{eg}$.

To link the macroscopic regime described in section 2.1 with the microscopic two level atom the polarisation of the medium has to be considered. This approach seems natural since the electric field of the propagating light wave intuitively has to cause a polarisation of the atomic medium. The polarisation $\boldsymbol{P}$ can be approximated by

$$\boldsymbol{P} = \sum_i \mathcal{N}_i \left\langle\boldsymbol{d}\right\rangle_i \tag{2.13}$$

for low number density (no local fields), where $\mathcal{N}_i$ is the number density of the $i^{\text{th}}$ type of two level atoms. Since only one type of atom is considered the sum collapses into one term. The proportional relation of the applied electric field $\boldsymbol{E}$ and the polarisation in isotopic media,

$$\boldsymbol{P} = \epsilon_0\chi\boldsymbol{E}, \tag{2.14}$$

is also well known [20]. The proportionality consists of the vacuum permittivity $\epsilon_0$ and the dimensionless electric susceptibility $\chi$. The latter is in general a complex number. The response of a medium to an electric field in equation (2.14) is not necessarily linear. In fact, the FWM introduced in section 1.2 originates in the $\chi^{(3)}$ non-linearity of the response of the atomic medium [27]. However, the weak probe regime used in this thesis justifies the linear approximation.

By substituting the plane wave in equation (2.1) into equation (2.14) we get

$$\boldsymbol{P} = \frac{1}{2}\epsilon_0\boldsymbol{E}_0\left[\chi e^{-i\omega t} + \chi^{\dagger}e^{i\omega t}\right], \tag{2.15}$$

for the macroscopic regime. In the microscopic regime we need to insert equation (2.12) into equation (2.13). Now we have two expressions for the polarisation which we can equate:

$$\mathcal{N}\boldsymbol{d}_{ge}\left[\tilde{\rho}_{ge}e^{i\omega t}+\tilde{\rho}_{eg}e^{-i\omega t}\right]=\frac{1}{2}\epsilon_0\boldsymbol{E}_0\left[\chi e^{-i\omega t}+\chi^{\dagger}e^{i\omega t}\right]. \tag{2.16}$$

By comparing the coefficients we immediately get

$$\begin{aligned}\chi\left(\Delta\right)&=\frac{2\mathcal{N}d_{ge}}{\epsilon_0E_0}\rho_{eg}\\&=\frac{d_{ge}^2\mathcal{N}}{\epsilon_0\hbar}f\left(\Delta\right)\\f\left(\Delta\right)&=\frac{i}{{}^{\Gamma}/_{2}-i\Delta}.\end{aligned} \tag{2.17}$$

The only parameter left to calculate is $d_{ge}$ which is closely connected to the decay rate $\Gamma$ by [28]

$$d_{eg}=\sqrt{\frac{3\pi\epsilon_0\hbar c^3\Gamma}{\omega^3}}. \tag{2.18}$$

Since those rates are obtainable through measurement and well known for alkali metal atoms the link of the two regimes is established by using the definition of the complex refractive index $n_c$ which, according to [20], can be written as

$$n_c=\sqrt{1+\chi}. \tag{2.19}$$

By comparing equation (2.19) and (2.3) it becomes clear that the attenuation factor $\alpha$ can now be written as

$$\alpha=2k_0\beta\approx k_0\chi_{\mathrm{im}}\left(\Delta\right). \tag{2.20}$$

Also the phase shift is given by

$$\Delta\phi=\left(-n_0\right)k_0l\approx\frac{1}{2}\chi_{\mathrm{re}}k_0l. \tag{2.21}$$

Now that the link of the macroscopic and microscopic behaviour of a two level medium is established, the implications for a multilevel system can be discussed.

### 2.2.1 Multilevel atom

The multilevel atom is a complicated system due to a lange number of coupled Bloch equations. The steady-state approximation becomes unjustifiable because of slow processes like off-resonant optical pumping [18]. Beam shape and beam crossing times have also to be taken into account expanding the problem further. Though solvable [18, 29, 30], a more easy approach is using the weak probe approximation, since no optical pumping occurs for the amount of time the atoms spend in the laser beam [18, 31, 26]. The weak pobe laser used in this thesis also justifies this approach. The multilevel atom can then be treated as a mixture of two level atoms with $\omega_i$ and relative strength factors $C_i$ corresponding to the transitions of the multilevel atoms. With $C_i$ extracted from $|\langle g|\, \boldsymbol{d}\, |e\rangle|^2$ [18] equation (2.17) can be modified to

$$\begin{aligned} \chi_i(\Delta) &= \frac{C_i^2 d^2 \mathcal{N}_a}{\epsilon\hbar} f(\Delta) \\ f(\Delta_i) &= \frac{i}{\Gamma/2 - i\Delta_i}. \end{aligned} \tag{2.22}$$

The new variables $d$ and $\mathcal{N}_a$ correspond to the reduced dipole matrix element and the number density of identical atoms, respectively. The latter can be derived from the elemental number density $\mathcal{N}$ by

$$\mathcal{N}_a = \frac{F_a \mathcal{N}}{2(2I+1)}, \tag{2.23}$$

where $F_a$ describes the isotope fraction and $I$ the nuclear spin [18]. The detuning $\Delta_i = \omega - \omega_i$ is now defined for each transition separately. With this the link between the multilevel atom, the two level system and the macroscopic response of a medium to an electromagnetic wave is established. The effect of the temperature on the system, however, is not negligible and will be discussed in the next chapter specifically for atomic vapours.

### 2.2.2 Temperature and density effects

This thesis focuses solely on rubidium vapours, therefore we narrow our view to the effects temperature has on rubidium. The boiling point of rubidium is 688 °C[32], which is significantly higher than the temperature of interest (163 °C). The focus therefore can be constrained to the effects of temperature on the liquid and solid phases of rubidium (melting point 39.3 °C).

#### Number density

The temperature influences the number density in the atomic medium through the vapour pressure given by [16]

$$\log_{10}(p\,[atm]) = A + B\,(T\,[K])^{-1} + C\log_{10}(T\,[K])\,. \tag{2.24}$$

Equation (2.24) is used to calculate the atomic number density $\mathcal{N}$ assuming an ideal gas:

$$\mathcal{N} = \frac{p}{k_B T}. \tag{2.25}$$

$A$, $B$ and $C$ are element and phase (solid or liquid) specific and are copied from [16] into table 9.1 located in the appendix. It is important to note that equation (2.25) shows a near exponential temperature dependence.

To extract the density of a specific isotope one simply multiplies by the corresponding isotope fraction (also known as isotopic abundance). In natural abundance rubidium that would be 0.7217 for $^{85}$Rb and 0.2783 for $^{87}$Rb, which are the two main isotopes rubidium consists of.

## Doppler broadening

While the temperature was neglected previously it is now necessary to address it since, it is notable in the temperature of interest. An atomic vapour has the temperature $T$. A single atom however has no temperature, only kinetic energy expressed by its velocity $\boldsymbol{v}$. The Doppler effect causes the atom to see a different $\omega$ of the incoming photon depending on its relative motion. In a thermal ensemble the velocity distribution in direction of light propagation of the atoms takes on a Gaussian shape [33]

$$g\left(v\right) = \frac{1}{U\sqrt{\pi}} e^{-\frac{v^2}{U^2}}, \tag{2.26}$$

with $v$ being the velocity component in direction of light propagation and $U = \sqrt{2k_B T/m}$ the root mean square (rms) of the speed of atoms, where $m$ is the mass of the atom. This results in an atomic line-shape $\mathcal{V}$ which is given by the convolution between the Lorentzian line-shape $f$ from equation (2.22) and the Gaussian velocity distribution $g$,

$$\begin{aligned} \chi_i\left(\Delta_i\right) &= \frac{C_i^2 d^2 \mathcal{N}_a}{\epsilon\hbar} \mathcal{V}\left(\Delta_i\right) \\ \mathcal{V}\left(\Delta_i\right) &= \int\limits_{-\infty}^{\infty} f\left(\Delta_i - kv\right) g\left(v\right) \mathrm{d}v. \end{aligned} \tag{2.27}$$

It is important to note that the rms $U$ has a square root dependency of the temperature, meaning that the exponential dependency in equation (2.25) is the dominant factor of the temperature effects.

The line shape of the atomic spectrum is also governed by other effects like dipole-dipole induced self broadening, broadening due to buffer gases and more [29, 34]. Discussing them all would lead behind the scope of this thesis. Furthermore, the software used to calculate the spectra in this thesis, called *ElecSus* [16, 17], takes those effects into account, so no further work is needed.

# 3 The Faraday effect

This effect was discovered by Michael Faraday September 13, 1845 [35]. Phenomenologically, it describes a rotation of the polarisation of light travelling through a medium within an applied magnetic field. A complete explanation emerged out of quantum mechanical observations many years later. They revealed a close relationship of the Faraday effect and the Zeeman splitting. To describe this relation the atomic Hamiltonian is a good point to start from.

## 3.1 Atomic Hamiltonian

The Hamiltonian of an atomic system is given by the sum of the underling interaction Hamiltonians,

$$\hat{\boldsymbol{H}} = \hat{\boldsymbol{H}}_0 + \hat{\boldsymbol{H}}_f + \hat{\boldsymbol{H}}_{hf} + \hat{\boldsymbol{H}}_Z, \tag{3.1}$$

where $\hat{\boldsymbol{H}}_0$ is the energy of the atomic system with no interactions, $\hat{\boldsymbol{H}}_f$ and $\hat{\boldsymbol{H}}_{hf}$ describe the fine and hyperfine structure. $\hat{\boldsymbol{H}}_Z$ contains the interactions with a magnetic field. The operators of the orbital angular momentum, electron spin and nuclear spin are given by $\hat{\boldsymbol{L}}$, $\hat{\boldsymbol{S}}$ and $\hat{\boldsymbol{I}}$, respectively. Equation (3.1) is a well known problem in atomic physics and has been discussed extensivly in various literature [18, 19, 23]. Here we will briefly summarise the findings beginning with the **fine structure** Hamiltonian,

$$\hat{\boldsymbol{H}}_f = \frac{\gamma_f}{\hbar^2}\left(\hat{\boldsymbol{L}} \cdot \hat{\boldsymbol{S}}\right), \tag{3.2}$$

which describes the spin-orbit coupling, with $\gamma_f$ the spin-orbit constant. Due to the interaction $L$ and $S$ cease to be good quantum numbers, $J = S + L$ and the corresponding eigenvalue $m_J$, however, are. The eigenstates of this Hamiltonian take the shape $|J, m_J\rangle$.

The **hyperfine structure** Hamiltonian,

$$\hat{\boldsymbol{H}}_{hf} = \hat{\boldsymbol{H}}_d + \hat{\boldsymbol{H}}_q, \tag{3.3}$$

consists of $\hat{\boldsymbol{H}}_d = \frac{A_{hf}}{\hbar^2}\hat{\boldsymbol{I}} \cdot \hat{\boldsymbol{J}}$, which describes the interaction between the nuclear spin and the magnetic field produced by the orbiting electron at the position of the nucleus and the electric quadrupole interaction Hamiltonian $\hat{\boldsymbol{H}}_q$. The nuclear spin interaction Hamiltonian $\hat{\boldsymbol{H}}_d$ is here the dominant term and it evokes a change of the base to $|F, m_f\rangle$, with $F = I + L + S = J + I$. Each of the interactions above cause energy shifts. Since different combinations of $L$, $S$ and $I$ can lead to the same quantum numbers $F$ and $J$ also quantum degeneracies to appear [23, 22, 18, 19].

In this thesis the **Zeeman interaction** Hamiltonian,

$$\hat{\boldsymbol{H}}_Z = \frac{\mu_B}{\hbar}\left(g_L\hat{\boldsymbol{L}} + g_S\hat{\boldsymbol{S}} + g_I'\hat{\boldsymbol{I}}\right)\cdot\boldsymbol{B}, \tag{3.4}$$

is in focus, since it gives rise to the Faraday effect. The corresponding $g$-factors for rubidium are listed in the appendix in table 9.2 together with various atomic constants of rubidium. $\boldsymbol{B}$ represents the applied magnetic field. By defining the quantisation axis along the direction of the magnetic field equation (3.4) simplifies to

$$H_Z = \frac{\mu_B}{\hbar}\left(g_L L_z + g_S S_z + g_I' I_z\right)\cdot B_z. \tag{3.5}$$

The Hamiltonian in equation (3.5) is special in the regard that each quantum number couples separately to the external magnetic field, such that it become possible to lift degeneracy introduced by the other interactions. Thus the following magnetic field regimes can be identified:

- $H_Z < H_{hf} < H_f \rightarrow$ Hyperfine linear Zeeman regime (HLZ)
- $H_{hf} < H_Z < H_f \rightarrow$ Hyperfine Paschen-Back regime (HPB)
- $H_{hf} < H_f < H_Z \rightarrow$ Fine Paschen-Back (FPB)

The FPB regime is accessible in rubidium at magnetic field strengths of $B > 218\,\mathrm{T}$ [19] and therefore not in the scope of this thesis. In the HLZ regime the wave function is best described by $|\Psi\rangle = |F, m_f\rangle$ and the magnetic field causes an energy shift given by

$$\Delta\mathcal{E}_Z = g_F m_F \mu_B B. \tag{3.6}$$

Entering the HPB regime, the Zeeman splitting becomes strong enough to decouple $F$ into $J$ and $I$. The new energy shift takes the shape

$$\Delta\mathcal{E}_Z = \left(g_J m_J + g_I' m_I\right)\mu_B B, \tag{3.7}$$

while the wave function is best described by $|\Psi\rangle = |m_J, m_I\rangle$. It is to note that both energy shifts (equation (3.6) and (3.7)) depend linearly on the magnetic field, since they consider only the fully coupled or uncoupled case. At an intermediate field strength, where neither $F$, nor $J$ and $I$ are good quantum numbers, the dependency is not linear, as the Breit-Rabi formula shows.

### 3.1.1 Breit-Rabi formula

The Breit-Rabi formula is an analytical equation, which describes the energy shift $\Delta E$ of an atomic state $|J = 1/2, I, m_F\rangle$ in an external magnetic field $B$ [36, 37, 38]:

$$\begin{aligned}\Delta\mathcal{E}_{F=I\pm 1/2,m_F} = &-\frac{h\Delta W}{2\left(2I+1\right)} + g_I' m_F \mu_B B \\ &\pm \frac{h\Delta W}{2}\sqrt{1+\frac{4m_F B\delta}{\left(I+1/2\right)\Delta W}+\left(\frac{B\delta}{\Delta W}\right)^2},\end{aligned} \tag{3.8}$$

with $\delta = \left(g_J - g_I'\right)\mu_B$ and $\Delta W = A_{hf}\left(I + 1/2\right)$. In the limits $B \to 0$ and $B \to \infty$ both equations (3.6) and (3.7) are represented by the Breit-Rabi formula. The first term describes the hyperfine structure and the second and third terms represent the HLZ and HPB regime. Figure 3.1 shows the evolution of the $5S_{1/2}$ ground state in $^{85}$Rb calculated by the Breit-Rabi formula.

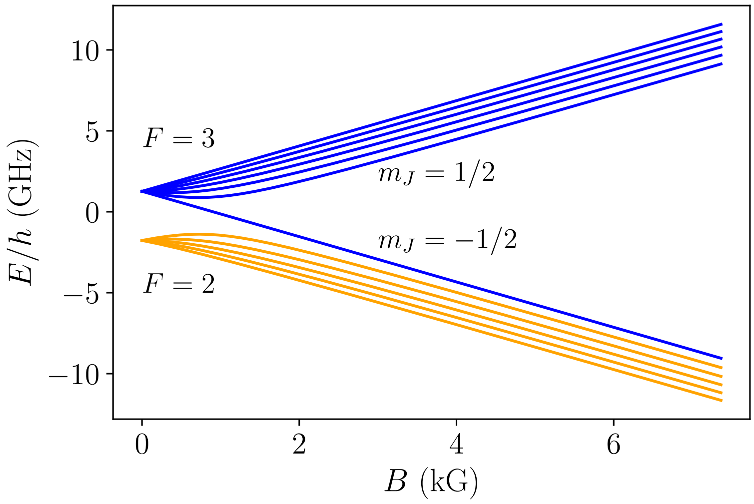

Figure 3.1: Energy splitting of the $5S_{1/2}$ ground state in $^{85}$Rb. The quantum number $F$ loses its validity with increasing magnetic field $B$ until $m_J$ and $m_I$ become good quantum numbers.

### 3.1.2 Implications of a magnetic field for the atom light interaction

The atom light interaction is described by the dipole operator $\hat{\boldsymbol{d}}$ (section 2.2).
By evaluating $\langle\Psi|\,\hat{\boldsymbol{d}}\,|\Psi'\rangle$, where $|\Psi\rangle = |L, m_L, m_S, m_I\rangle$ and $\hat{\boldsymbol{d}} = e\hat{\boldsymbol{r}}$ ($e$ is the elementary charge) we get the section rules $\Delta m_L = \pm 1, 0$, $\Delta m_S = 0$ and $\Delta m_I = 0$. $\Delta m_L = \pm 1, 0$ corresponds to $\sigma^+$, $\sigma^-$ and $\pi$ transitions, respectively. The frequency required to drive the transition is given by the energy difference $(\mathcal{E}_e - \mathcal{E}_g)$ of the states.

By applying a magnetic field the transitions shift due to the Zeeman effect and the degeneracies will be lifted. In the hyperfine Paschen-Back regime, for instance, the $2(F+1)$ fold degeneracy of the states is lifted and they split into the different $|m_J, m_I\rangle$. Recalling the selection rules from above we get $\Delta m_J = \pm 1, 0$. The energy shifts influence $\sigma^+$ and $\sigma^-$ transitions differently, which in turn affects the refractive index ($n^+ \neq n^-$) associated with those transitions. This behaviour, also known as circular birefringence, gives rise to a macroscopic phase shift shown in equation 2.7. Furthermore, linear polarised light can be described as a composition of two in phase left- and right-hand circular polarised light waves. So one component will also be shifted in respect to the other, causing a rotation of the polarisation (see section 4.1). This phenomenon carries the name Faraday effect. An energy level scheme of the main transitions of $^{85}$Rb in a magnetic field is given in figure 3.2. A more detailed representation is found in figure 7.6 in section 7.1.

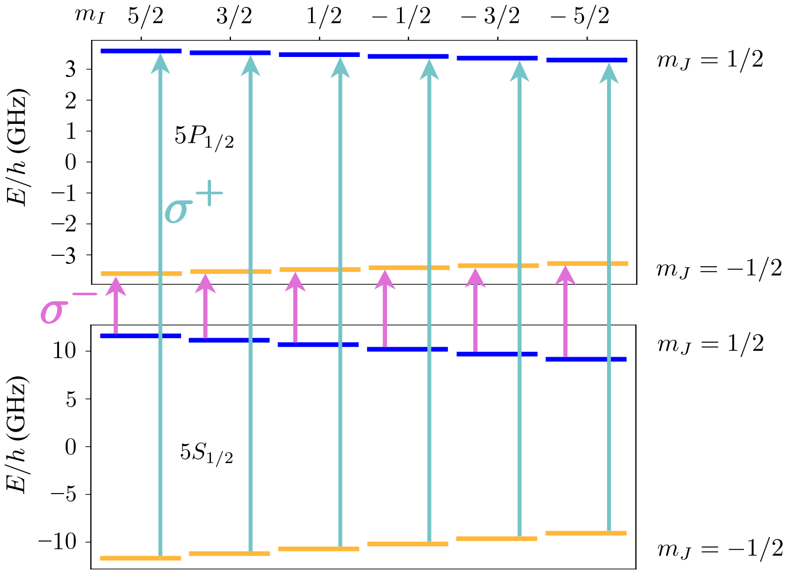

Figure 3.2: Energy levels and main transitions of the $^{85}$Rb D$_1$-line in a magnetic field of $B = 7.366\,\mathrm{kG}$. The respective eigenvalues are given as $m_J$ and $m_I$.

In the HPB regime the basis is not completely decoupled, as is visible in equation (3.8). The wave function of a state is therefore given by $|\Psi\rangle = a\,|m_J, m_I\rangle + b\,|m'_J, m'_I\rangle$, where $a > b$ and $m_J + m_I = m'_J + m'_I$. This admixture gives rise to the ‘weak transitions’ observed in the experiments. The admixture vanishes with increasing $B$-field.

# 4 Spectroscopy tools

This chapter gives a short introduction into the notations and spectroscopy techniques used to calibrate the experimental data. It is important to note, that from now on whenever the term frequency $\nu$ or detuning $\Delta$ is used, ordinary frequency (Hz), not angular frequency ($\omega$) is meant. All detunings are also given in ordinary frequency.

## 4.1 Stokes parameters

The polarisation of light is best visualised in a Poincaré sphere where the Stokes parameters $S_0$ to $S_3$ [39, 40, 41] represent the coordinates. The Stokes parameters for light propagating through a medium with length $L$ are defined as:

$$\begin{aligned}
S_0 &= I_- + I_+ = I_x + I_y = I_0 \frac{1}{2}\left(e^{-\alpha^- l} + e^{-\alpha^+ l}\right) \\
S_1 &= I_x - I_y = I_0 \cos(2\phi) e^{-\frac{1}{2}(\alpha^- + \alpha^+) l} \\
S_2 &= I_{\nearrow} - I_{\searrow} = I_0 \sin(2\phi) e^{-\frac{1}{2}(\alpha^- + \alpha^+) l} \\
S_3 &= I_+ - I_- = I_0 \frac{1}{2}\left(e^{-\alpha^+ l} - e^{-\alpha^- l}\right).
\end{aligned} \tag{4.1}$$

The parameters $\alpha^+$ and $\alpha^-$ are the absorption coefficients for left and right circular polarised light at a particular detuning respectively. $I_x$, $I_y$, $I_{\nearrow}$, $I_{\searrow}$, $I_-$ and $I_+$ represent the transmission in the respective polarisation. $I_x$ and $I_y$ mean $x$ and $y$ polarised. $I_+$ means left-, $I_-$ right-circular polarised. $I_{\nearrow}$ and $I_{\searrow}$ are ±45° polarised, respectively. Furthermore, $S_i' = S_i/S_0$ is the normalised Stokes parameter for $i \in \{1, 2, 3\}$. $\phi$ is the rotation angle caused from the phase shift of the left- and right-polarised components $\Phi^\pm = k_0 n^\pm l$ of the linear polarised light by the medium. $\theta_0$ is the initial rotation angle, $n^\pm$ is the refractive index for left- and right-circular polarised light, respectively. In our case $\theta_0 = 0$ and $I_0 = 1$.

$$\phi = \frac{1}{2}\left(\Phi^+ - \Phi^-\right) + \theta_0 \tag{4.2}$$

Equation (4.2) allows one to plot the rotation angle as a function of the medium length and detuning. The parameters, absorption coefficients $\alpha^\pm$ and refractive indices $n^\pm$ are calculated by *ElecSus* and the wave number is fixed to $k_0 = \frac{2\pi}{795\,\mathrm{nm}}$ since only the $\mathrm{D}_1$ transition is examined in this thesis. This approximation is valid since the wavelength $\lambda$ changes significantly less than $\Delta\lambda < 1\,\mathrm{nm}$ over the scanning range in this thesis.

## 4.2 Calibration of the frequency axis

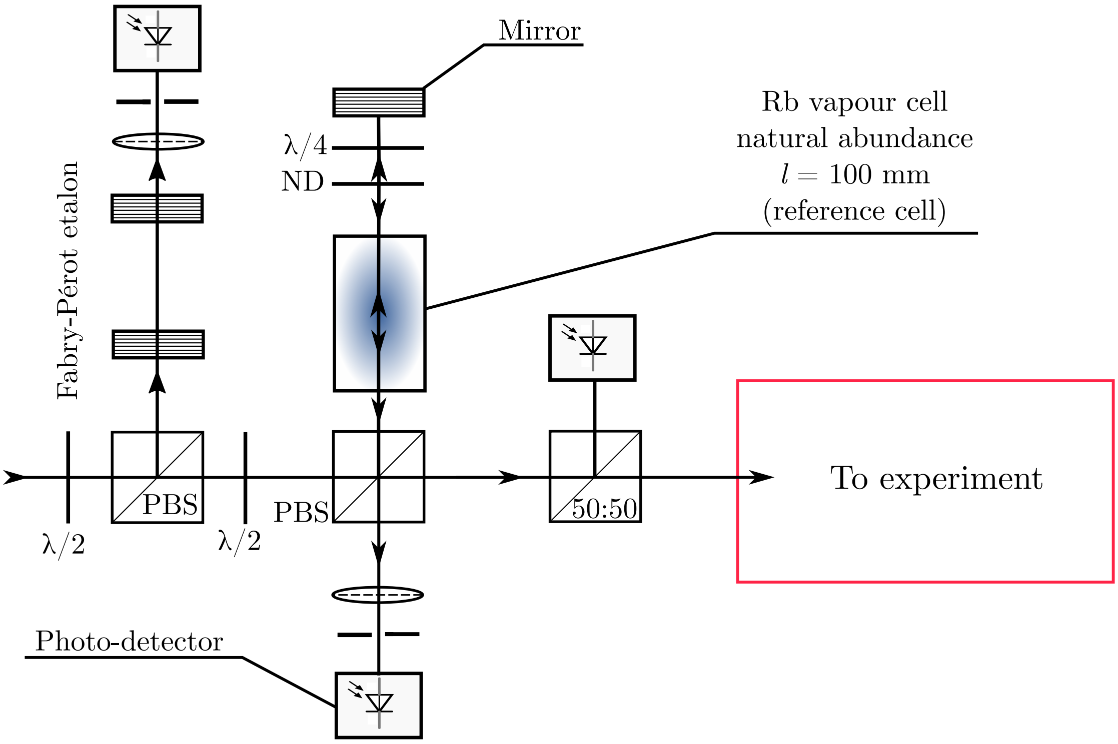

Figure 4.1: Setup for the calibration of the frequency axis. The $\lambda/2$-plates and the polarising beam splitters (PBS) allow the amount of power directed in each direction to be controlled. The 50 : 50 beam splitter and the corresponding photo-detector monitor the laser scan profile $I_0(\Delta)$. The residual light is transmitted to the experiment. The Fabry–Pérot etalon and the rubidium vapour cell are enabling the frequency calibration.

The calibration of the frequency axis becomes necessary since the oscilloscope records the time dependent signal from the photo-detectors

$$V(t) = R \cdot I(t) . \tag{4.3}$$

Here, $R$ is the constant transimpedence amplification factor of the photo-detector. By scanning the laser $V(t)$ effectively transforms into a detuning dependent $V(\Delta)$. This transformation is typically not linear. The goal of this section is to find the transformation rule $t \rightarrow \Delta$. To do so a relative and an absolute frequency marker can be used as described in [19].

Figure 4.1 shows the part of the experimental setup required to calibrate the data. The Fabry–Pérot etalon is discussed first in the following paragraph.

### 4.2.1 Fabry–Pérot etalon

The Fabry–Pérot etalon in figure 4.1 consists of two parallel planar mirrors. It is used as a relative frequency-marker, since the distance between the peaks, also known as free spectral range, is given by

$$\Delta\nu = \frac{c}{2nL}, \tag{4.4}$$

where $n$ is the refractive index of the medium between the mirros, in our case air ($n = 1$), and $L$ the distance between the mirrors [42]. The transmission through the etalon peaks every time the wavelength $\lambda$ of the laser fulfils

$$s\lambda = 2n \cdot L, \tag{4.5}$$

where $s \in \mathbb{N}$. An example of the signal of such a device is displayed in figure 4.2. The etalon peaks are equidistant in frequency and if the scan is linear, they should be also equidistant in the time domain. However, as mentioned earlier, the scan is not linear. In this thesis a polynomial of the $5^{th}$ order was used to fit the non-linearity.
With the relative frequency marker at hand one can linearise the scan as described in [19]. Now what is left is to find an absolute frequency reference to link the linearised axis to the frequency axis. To our advantage rubidium itself can provide us with one, as described in the next paragraph.

### 4.2.2 Saturated absorption spectroscopy

The resolution of transmission measurements is typically Doppler-limited. This limitation can be overcome by using a counterpropagating pump and weak-probe configuration [31]. In this technique the pump, when resonant, excites the atoms, introducing a population depletion of the ground sate. At the same time the counterpropagating weak probe beam is not absorbed as strongly any more by atoms in the velocity class $v_p = 0$, scince they are already excited or have relaxed into the other ground state. The transmission of the weak probe is then enhanced within a natural linewidth of the transition. This allows resolutions which are no longer Doppler-limited. Other than the hyperfine structure, cross-over resonances [31] are also among the features attainable by the saturated absorption spectroscopy. Those resonances originate from velocity classes $v_p \neq 0$ where, due to the Doppler-shift, the pump beam is resonant with one transition and the probe beam is resonant with the other. The crossover resonances behave as if additional states were present with energies in-between the atomic ground states. The Lamb-dips 2, 5, 8, 11 in figure 4.2 are crossover resonances of the rubidium isotopes.

In this thesis the saturated absorption spectroscopy has been conducted in a 10 cm long cell filled with a natural rubidium mixture (see figure 4.1). For long cells room temperature is sufficient to produce a noticeable optical depth, therefore no heating is needed. In case of the rubidium $D_1$-line the recorded spectrum is displayed in figure 4.2, including the 12 sub-Doppler features with well known frequencies [31]. The frequency axis calibrated by this process shows accuracies of around $\Delta\nu < \pm 10\,\mathrm{MHz}$.

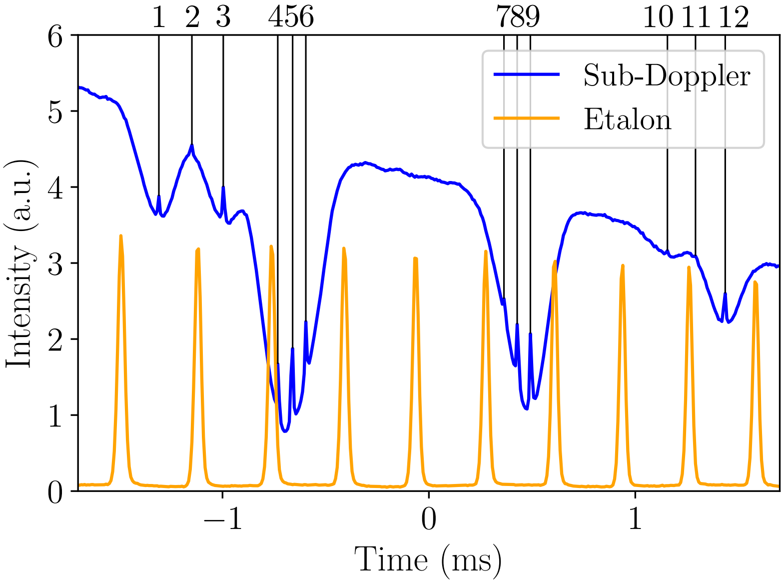

Figure 4.2: Example of etalon and saturated absorption spectroscopy signal used to linearise and transform the time axis into a detuning axis. The twelve features (Lamb-dips) used as absolute frequency markers are also displayed. They consist of the hyperfine structure and four crossover resonances (2,5,8,11).

### 4.2.3 Weighted line-center

The weighted line-center is chosen as 0 detuning. The spectral position is given by the $\nu$ where the atomic transitions would reside if no ground state splitting would exist [43]. For the rubidium $D_1$-line the frequency of the weighted line-center is given in table 4.1

Table 4.1: Weighted line-center of the rubidium $D_1$-line [18]

| | |
|---|---|
| Line-center wavelength | 794.978969380(82) nm |
| Line-center frequency | 377.107407299(39) THz |

### 4.2.4 Laser scan profile

Other than the the non-linearity discussed above the intensity of the laser varies during the scan. This leads to the scan profile shown in figure 4.3. The scan profile is not trivial, since it consists not only of the non-linear behaviour of the laser, but also picks up shape distortions of any kind from the optics in the laser path, until the detection. In order to correct for the scan profile a photo-detector monitors it along with the etalon and reference cell. The transmission through a cell is obtainable by

$$T \equiv \frac{I}{I_0} \propto \frac{R \cdot I(\Delta)}{R' \cdot I_0(\Delta)}, \tag{4.6}$$

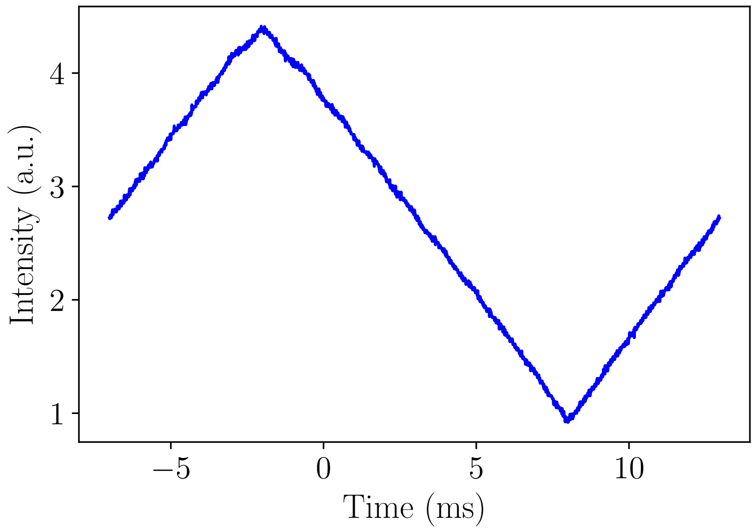

Figure 4.3: Trace of the laser intensity before the experiment, captured by the photodetector at the 50:50 beam splitter in figure 4.1. Scan reversal points are clearly visible.

where $I_0\left(\Delta\right)$ describes the scan profile and $I\left(\Delta\right)$ the signal after the cell. The ratio ${}^{R}/_{R'}$ refers to scaling imperfections due to alignment. Ideally ${}^{R}/_{R'} = 1$, however, in practice it deviates slightly.

# 5 Design by computational optimisation

Transmission spectra of an atomic rubidium vapour are very accurately predicted by software like *ElecSus* [16, 17]. With the adjustment of only the applied magnetic field $B$, temperature $T$ and the parameters of the incoming light (polarisation, detuning, angle) a wide variety of experiments and devices such as optical isolators [44, 45, 46], optical filters and rotators [47, 45, 48] are computable.
The aim of this thesis is to design and construct an atomic Faraday filter as a beam splitter for photon pairs. Similar work has been demonstrated to be feasible by [49, 50]. However, this thesis goes further and utilises computational optimisation with *ElecSus* [16, 17] and *scipy.optimize.minimize*[1] [15] in order to find the best possible performance regime. The modelled setup is shown in figure 5.1. Due to the direction of the applied magnetic field only $\Delta m_J = \pm 1$ transitions are allowed. Some of the parameters have to be constrained in order to ensure the feasibility of the device. In this thesis a 2 mm long cell filled with rubidium at the different isotope ratios of 1.8 %, 72.17 % and 99.89 %

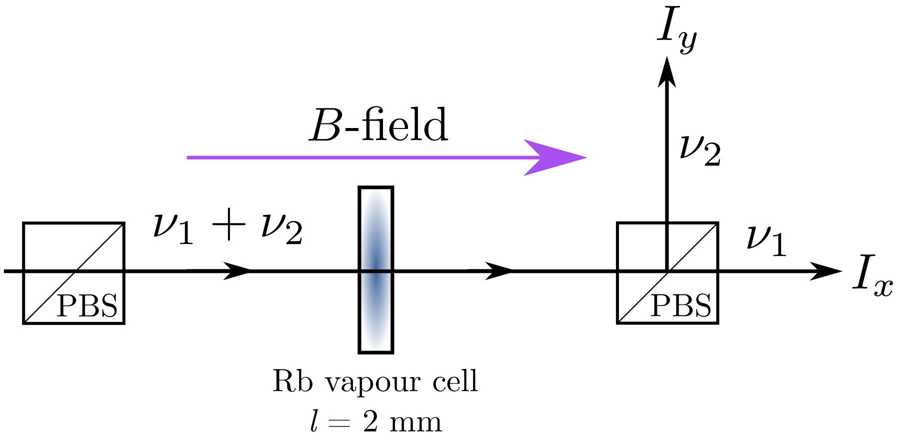

Figure 5.1: Simplified experimental setup of the Faraday filter. Two photons with $\nu_1$ and $\nu_2$ in the same polarisation travel through a thermal vapour cell in a magnetic field. Here, each photon experiences a different amount of rotation due to the frequency dependant Faraday effect. Finally the two photons are separated due to their different polarisation states at the second PBS. Ideally the photons are rotated by $\pi/2$ in respect to each other. $I_x$ corresponds to the transmission of $x$-polarised light through the vapour cell (PBS).

---

[1] *scipy.optimize.minimize*: Refers to the *minimize* function in the *optimize* module of the *scipy* Python library (v 1.1.0).

$^{85}$Rb are discussed. The ratios 1.8 % and 99.89 % are chosen since such enrichments are commercially available and 72.17 % is the natural abundance. The temperature is constrained to a maximum of 250 °C in order to minimise reactions of the rubidium with compounds of the borosilicate cell walls in the actual experiment. The magnetic field was constrained to a maximum of 10 kG because it has been shown that this is achievable with two neodymium magnets in Helmholz configuration [18, 51].

Short cells allow a larger magnetic field strength than longer cells, because the magnets can be placed closer together (see section 5.4). The light input to this Faraday beam splitter will come from a four-wave mixing (FWM) device capable of producing a photon pair 6 GHz or 13.6 GHz apart (see section 1.2). To briefly summarise the FWM device produces two photons in a parametric process which are separated by two times the ground state splitting $\nu_s$ of the rubidium isotope involved. One of the photons experiences a parametric down conversion $\nu_p - \nu_s$ and the other a parametric up conversion $\nu_p + \nu_s$ in respect to the pump frequency $\nu_p$. From here onward the photon with a frequency of $\nu_p - \nu_s$ will be referred to as the red channel and the one with a frequency of $\nu_p + \nu_s$ as the blue channel. The input light is constrained to be horizontally polarised, because it simplifies the construction of the actual experimental setup.

## 5.1 Cost function and implementation of a global optimisation routine

To construct an atomic Faraday filter as beam splitter using *ElecSus* an appropriate function has to be found which assigns a cost value to an arbitrary spectrum of any given $T$ and $B$. By comparing the assigned cost values of all calculated combinations ($T$,$B$) the optimal working conditions are identified. It is necessary to mention that the minimisation routine will maximise the absolute value of terms with negative signs. Therefore we can split our cost function into two terms, one with negative and one with positive sign (see equation (5.1)), to accommodate both, channel suppression and channel transmission, in one equation. To increase cost function fidelity the terms are squared before the sign is assigned. The Faraday filter has to ideally satisfy the following conditions in order to display the best possible performance for the photon pair separation:

The transmission $I_x(\nu_1)$ of one channel has to drop to zero, while $I_y(\nu_1)$ becomes 1. At the same time the other channel's transmissions $I_x(\nu_2)$ and $I_y(\nu_2)$ have to display inverse behaviour to the first channel in order to get a high performance beam splitter, as shown in figure 5.8 b) and c). The indices $x$ and $y$ refer to horizontal and vertical polarisation of the out coming light, respectively. Since it is not important which channel is vertically or horizontally polarised the cost function consists of two parts $C_1$ and $C_2$.

$$C = \begin{cases} C_1 &= \left(I_y(\nu_1) + I_x(\nu_2)\right)^2 - \left(I_x(\nu_1) + I_y(\nu_2)\right)^2, C_1 < C_2 \\ C_2 &= \left(I_x(\nu_1) + I_y(\nu_2)\right)^2 - \left(I_y(\nu_1) + I_x(\nu_2)\right)^2, C_2 < C_1 \end{cases} \tag{5.1}$$

The cost function (equation (5.1)) vanishes if both channels are equally transmitted with the same polarisation. In case both channels are transmitted lossless in the desired polarisations the cost function reaches its lowest possible value $C = -4$.

In order to find the best possible parameters the *scipy* module *scipy.optimize.minimize* is used to minimise the cost function of the system. The parameter space is evaluated by briefly mapping it (100 G and 1 °C steps) from 0 to 10 kG and from 0 to 250 °C in order to find the region with the most promising cost values. The point with the lowest cost value is passed to the *scipy.optimize.minimize* module which uses the Nelder-Mead method [52] to minimise the cost function further, thus optimising the filter. In figure 5.2 the cost functions have been mapped separately for an arbitrary pump detuning of $-1$ GHz in respect to the weighted line center [16, 17] and a 2 mm cell filled with 99.89 % $^{85}$Rb with $\nu_s = 6.8$ GHz. It is to emphasise, that the $\nu_s$ corresponds to the isotope involved in the FWM process and not to the filling of the atomic Faraday filter. It is noticeable that the minima of the cost function are appearing somewhat periodically in temperature. Each consecutive minimum corresponds to an additional $\pi/2$ rotation of the output signal. It is caused by the increase of number density in the atomic vapour leading to more rotation per unit length.
Furthermore the two regimes $B > 4$ kG and $B < 4$ kG are emerging, separated by a region around 4 kG with bad cost values, caused by the absorption lines being Zeeman shifted right on top of the blue and red channel. The origin of the two magnetic regimes is found by investigating the rotation angle while the light propagates through the medium. The rotation angle is calculated by equation (4.2) and displayed in figure 5.3 at the corresponding minimum. It is to note that the map shown in figure 5.3 corresponds to a pump detuning of $-1.4$ GHz (see section 5.3). The different magnetic field regimes represent the cases were the red channel is rotated more than the blue or vice versa. The magnitude and direction of rotation at any given magnetic field for each channel, however, depends on the channel frequency. This frequency in turn is determined by the pump detuning in the case of a FWM device. Atomic media are also known for 'anomalous rotation'[2], which also depends on the spectral position of the channel and the magnetic field [53].

In an attempt to map the pump detuning dependency of the cost function the optimisation routine is repeated for detunings from $\Delta_p = -3.8$ GHz to $\Delta_p = 6.4$ GHz in 100 MHz steps. Figure 5.4 shows the parameters with the lowest cost value of each pump detuning for a 99.89 % $^{85}$Rb cell. The results for 72.17 % $^{85}$Rb and 1.8 % $^{85}$Rb are shown in the appendix (figure 9.1 and 9.2 respectively). Discontinuities in the magnetic field and temperature plot in figure 5.4 can be explained by a jump from one of the minima to another with similar or better cost values. Due to the discrete nature of the mapping routine it is also possible to miss the global minimum if a second minimum with similar cost value exists in the system. The latter becomes a problem in particular when the initial discrete mapping steps are large. In that case the global minimum is missed. With bigger pump detuning the performance of the system increases as well as the required

---

[2] Anomalous rotation occours when $n^+ > n^-$. This happens around the line-center for large magnetic fields as shown in figure 5.8 d). At this region the rotation of the light is not along the usual direction.

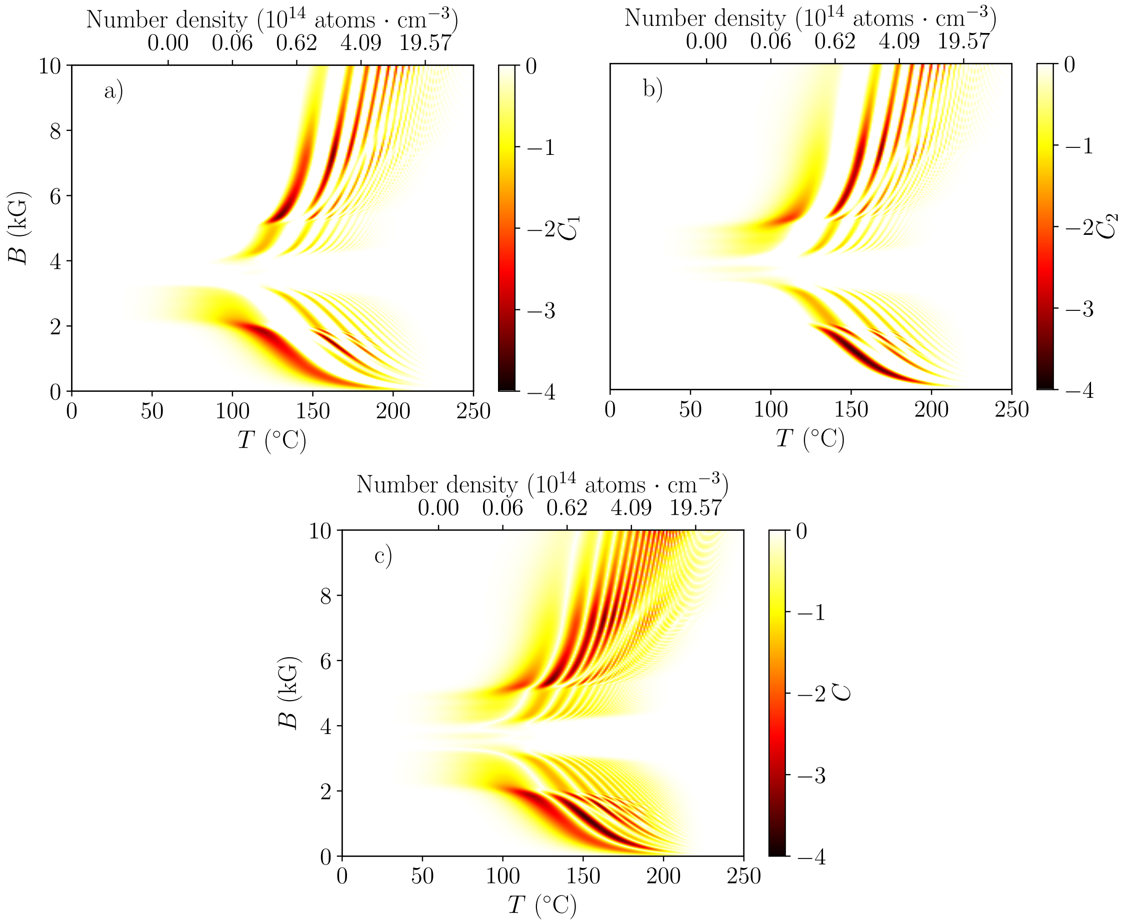

Figure 5.2: a) Map of $C_1$ over temperature ($0 - 250\,°\mathrm{C}$ in $1\,°\mathrm{C}$ steps) and magnetic field ($0 - 10\,\mathrm{kG}$ in $1\,\mathrm{G}$ steps) for a pump detuning of $-1\,\mathrm{GHz}$, a cell length of $2\,\mathrm{mm}$, in case of $\nu_s = 6.8\,\mathrm{GHz}$ separation of the channels. b) Map of $C_2$ in the same parameter constraints. c) Combination of $C_1$ and $C_2$, only the lowest value was considered for every combination of $T$ and $B$.

magnetic field.

An interesting feature in figure 5.4 is the absence of suited coordinates $(T, B)$ for the realisation of an atomic Faraday beam splitter at a pump detuning of $0\,\mathrm{GHz}$. The optimal parameters according to figure 5.4 c) are found to be $T = 158.9\,°\mathrm{C}$ and $B = 4.894\,\mathrm{kG}$ with a very high cost value of $C = -2.2$. In an attempt to explain this high cost value the rotation magnitude and direction of the light after it passed the $2\,\mathrm{mm}$ long vapour cell is investigated[3]. At optimal parameters a symmetry in rotation is revealed,

---

[3] Note that at the atomic resonances, the definition of a rotation angle $\phi$ breaks down in case of an optically thick medium, since circular polarised light has no defined polarisation axis which could be rotated.

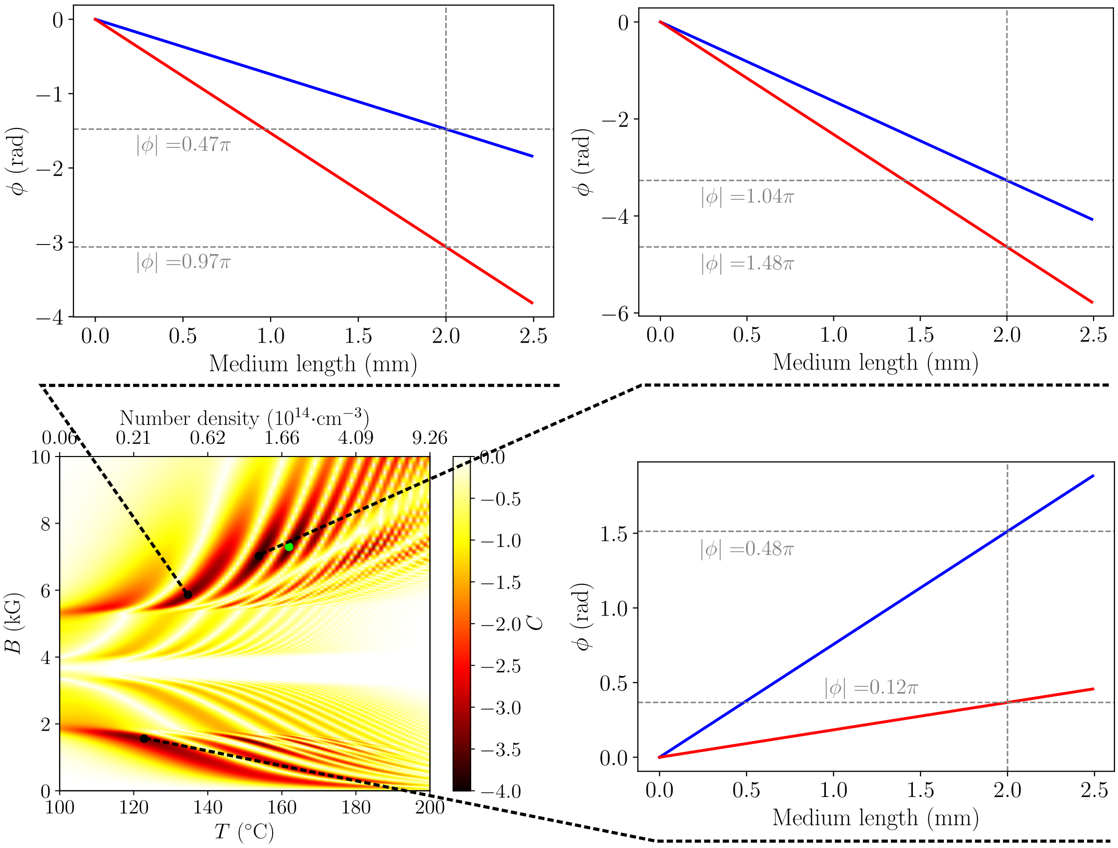

Figure 5.3: The colour map shows the cost values for a pump detuning of $\Delta_p = -1.4\,\mathrm{GHz}$. Each minimum in the upper part ($B > 4\,\mathrm{kG}$) of the map corresponds to a regime where the red channel has always been rotated $\pi/2$ further than the blue channel. The bottom part ($B < 4\,\mathrm{kG}$) displays the reversed case, also the rotation direction changes. Each consecutive minimum (from left to right) corresponds to an additional $\pi/2$ absolute rotation of both channels changing their respective polarisation from horizontal to vertical or vice versa. The green dot indicated the coordinate used to realise the atomic Faraday beam splitter at a cost value of $C = -3.8$. The spectrum and the rotation angle of the optimal parameters are depicted in figure 5.8 and 5.10 in section 5.3 respectively.

as shown in figure 5.5. This symmetry solidifies with growing $B$ since the HPB-term of the Breit-Rabi equation (3.8) dominates with growing field strengths.

The ratio $\phi(\nu_1)/\phi(\nu_2) = 1.07$ extracted from figure 5.5 shows that both channels are rotated in the same direction with similar magnitude. For weaker $B$-fields the absorption at the channels increases since they become more resonant with the transitions. This vicinity to the transitions leads to an elliptically polarised output and ultimately to a higher cost value. In the case displayed in figure 5.4 f) a weak magnetic field should

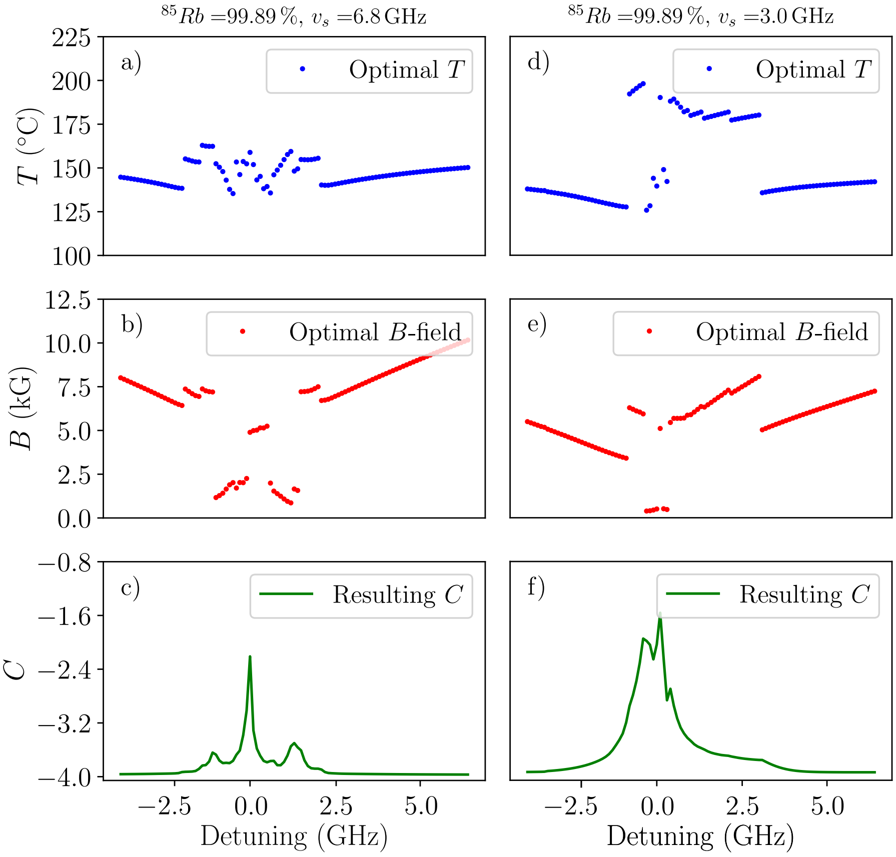

Figure 5.4: Optimised parameters for a 99.89 % $^{85}$Rb cell $l = 2$ mm. a) - c): For $\nu_s = 6.8$ GHz, d) - e): For $\nu_s = 3$ GHz over the pump detuning. Each pump detuning is assigned a lowest possible cost value in c) and f) found by the optimisation routine. a), d) and b), e) display the temperature and $B$-field to the corresponding lowest cost value of each pump detuning, respectively. The weighted line-center of the $D_1$-line coincides with 0 GHz detuning [16, 17].

be able to separate the photons, since non-linearities of the Zeeman splitting for low fields cause a difference in rotation magnitude as shown in figure 5.6. However, the temperature required to reach a relative angle of $\pi/2$ at the end of the 2 mm cell leads to more absorption. This diminishes the performance of the atomic Faraday beam splitter significantly. Therefore no good separation is possible at a pump detuning of 0 GHz. The cost values for a cell with natural abundance and with 1.8 % $^{85}$Rb in the appendix show similar behaviour (figure 9.1). Solely the vapour cell filled with 1.8 % $^{85}$Rb abundance and $\nu_s = 6.8$ GHz is providing a low cost value ($C = -3.69$). A possible explanation for this non-intuitive behaviour is provided in the appendix (section 9.2).

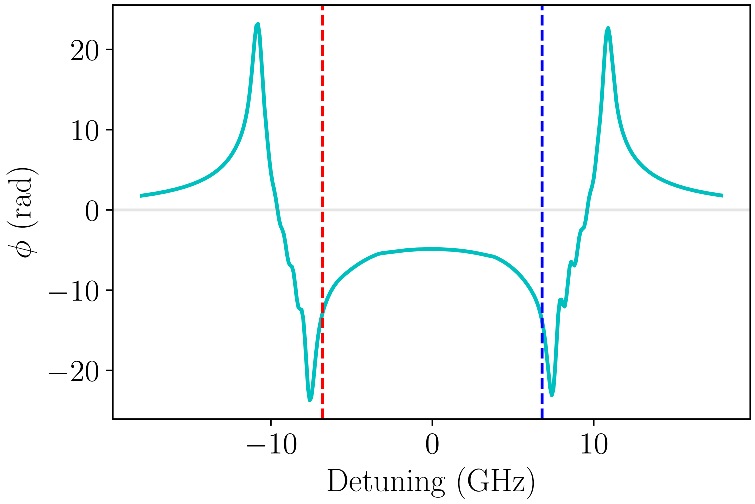

Figure 5.5: Rotation angle over pump detuning for a 99.89 % $^{85}$Rb cell (2 mm). Parameters of the vapour: (159 °C, 4.894 kG). Dashed vertical lines indicate the position of the red and blue channel for $\nu_s = 6.8$ GHz. Both channels are rotated by roughly the same magnitude in the same direction by the Faraday effect. Together with the vicinity of the channels to the transitions this causes a high cost value ($C = -2.2$).

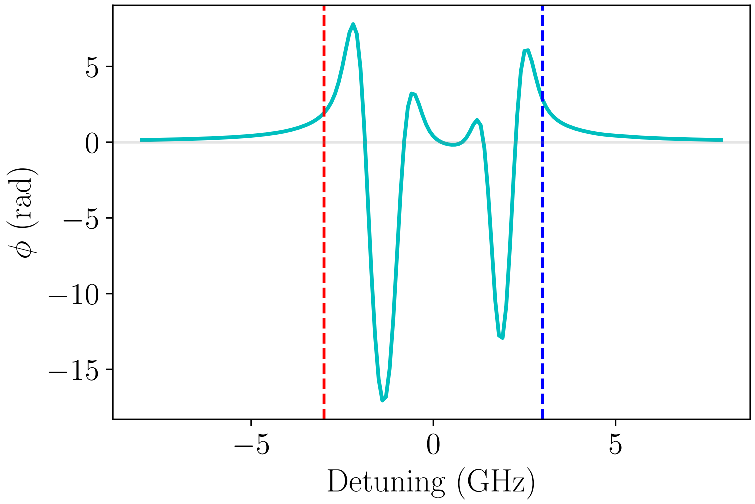

Figure 5.6: Rotation angle over pump detuning for a 99.89 % $^{85}$Rb cell (2 mm), $\nu_s =$ 3.0 GHz. Parameters of the vapour: (140 °C, 250 G). Due to the non linear Zemman effect in low magnetic fields the symmetry is broken. However the vicinity of the channels to the transitions still causes a high cost value ($C = -2.0$), due to absorption.

## 5.2 Introduction of channel impurity and attenuation

For the evaluation of the atomic Faraday filter as a beam splitter it is handy to introduce a measure, other than the cost function, which tells us how well the photons get separated. Here this is done with the impurity, defined as

$$\gamma_{1,2} = \frac{I_{x,y}\left(\nu_{1,2}\right)}{I_{x,y}\left(\nu_{2,1}\right)}, \tag{5.2}$$

which describes how much of the light from the signal photon leaks into the light path of the idler photon and vice versa. It is to note that $\gamma_{1,2}$ only describes a minimal limit, since the linewidth of the emitted photons is not taken into account.

An important parameter for the performance of the Faraday filter is the stability. In this thesis the stability was estimated by evaluating the suppression (attenuation),

$$L = 20 \cdot \log_{10}\left(\frac{I_{x,y}\left(\nu_1, \nu_2\right)}{I_{y,x}\left(\nu_1, \nu_2\right)}\right) \mathrm{dB}, \tag{5.3}$$

the filter causes for a given photon of the generated photon pair.

## 5.3 Working regime

A pump detuning of $-1.4\,\mathrm{GHz}$ is chosen since it is resonant with the transition from the ground manifold $5S_{1/2}$ $F = 3$ to the excited manifold $5P_{1/2}$ in $^{85}$Rb. This detuning has been identified to show the best compromise in performance ($C < -3.8$) of the atomic Faraday beam splitter while ensuring the removal of the pump laser from the fibre output via a separate isotopically pure $^{85}$Rb cell. The optimal parameters are found to be $B = 7.374\,\mathrm{kG}$ and $T = 162.9\,°\mathrm{C}$ and a 99.89 % $^{85}$Rb, 2 mm cell. Figure 5.7 displays good agreement of the mapping with the subsequent *scipy.optimize.minimize* method. Furthermore, it shows that for a magnetic field deviation of $\Delta B \approx 80\,\mathrm{G}$ around the optimised coordinates the cost value does not exceed $C_{max} = -3.8$. This is important since it gives a margin of error regarding the optimal parameters. If not reached the atomic Faraday beam splitter will only experience small degradation of performance within this margin of error.

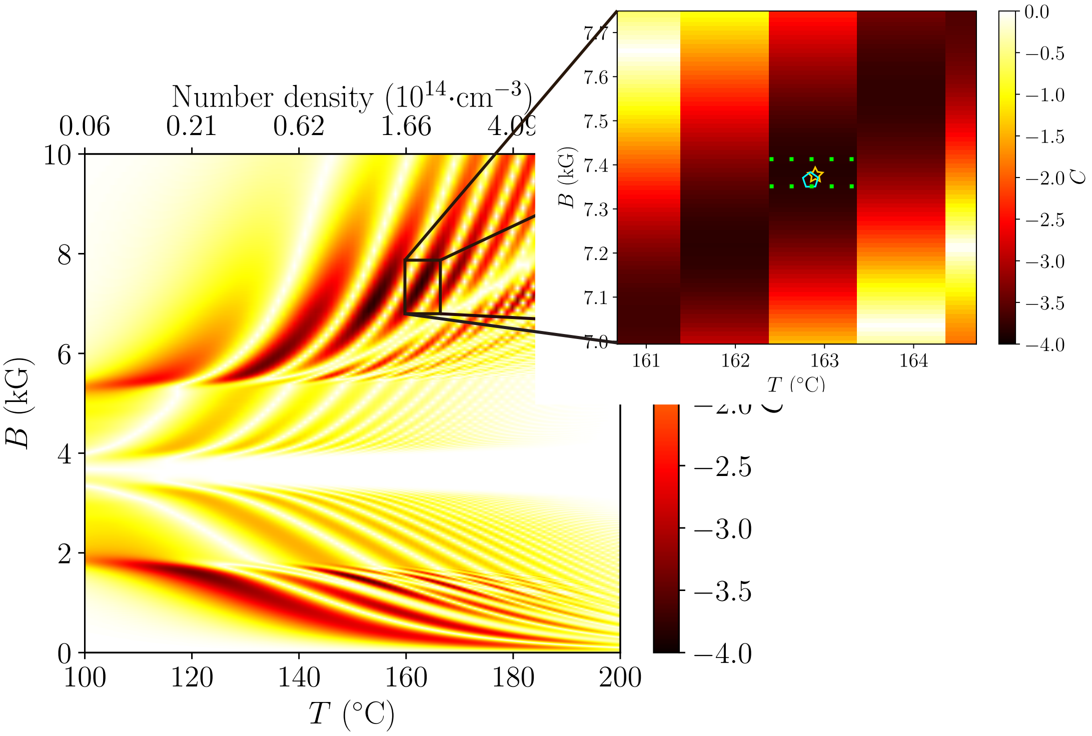

Figure 5.7: Minimal cost found after mapping $(7.390\,\mathrm{kG}, 163\,°\mathrm{C})$. Optimised minimal cost after using *scipy.optimize.minimize* with the initial parameters from the map $(7.374\,\mathrm{kG}, 162.9\,°\mathrm{C})$. In between the green markers ($\Delta B \approx 80\,\mathrm{G}$) the cost value does not exceed $C_{max} = -3.8$.

The expected spectra are presented in figure 5.8. An interesting feature is that the incoming light from detunings beyond $\Delta = \pm 20\,\mathrm{GHz}$ is still effected in its polarisation by the medium (figure 5.8 a, b, c) even though the transmission spectrum does not show any significant absorption. The position of the blue and red channel between the two absorption minima shows negative $n^-$ component (figure 5.8 d) and indicates anomalous rotation.

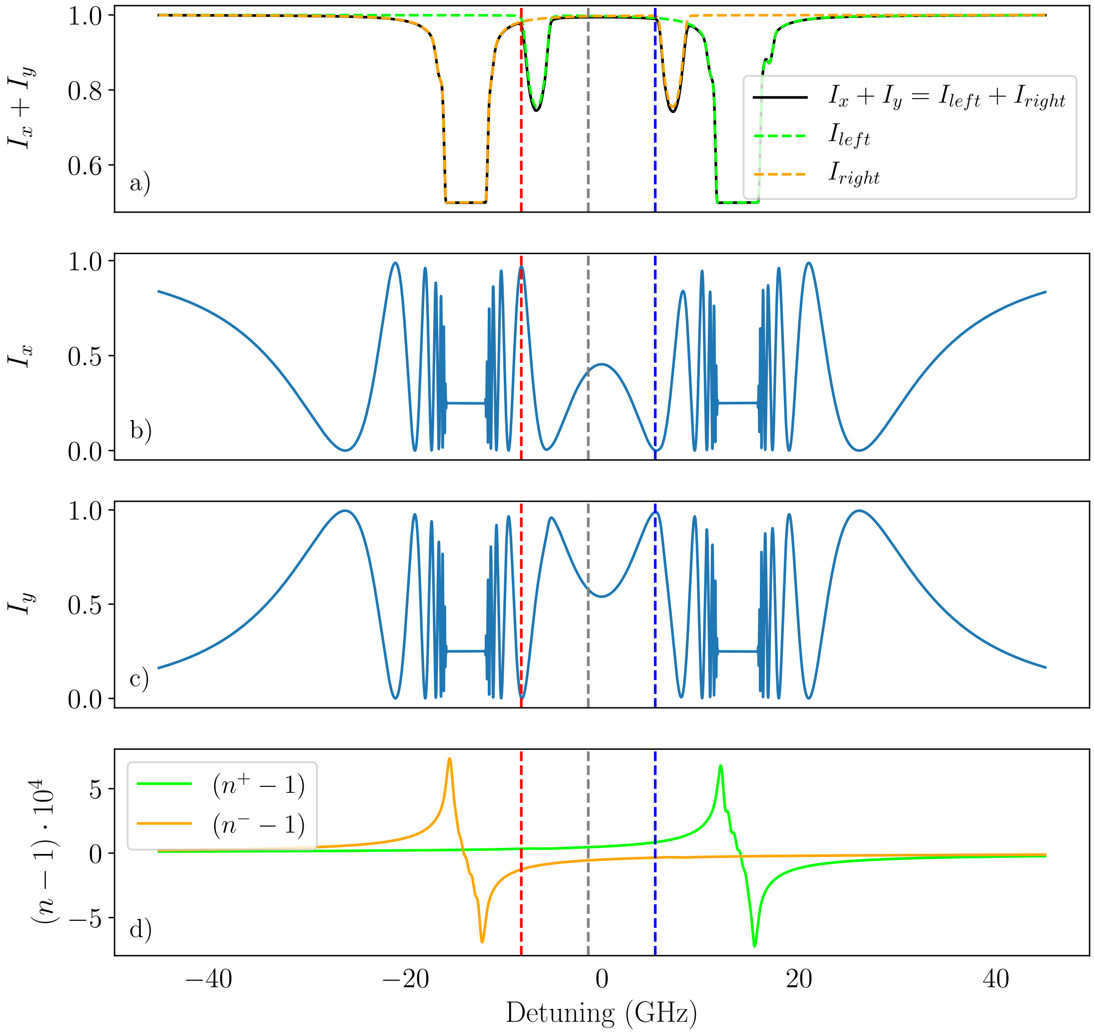

Figure 5.8: Expected transmission spectrum (top) calculated by *ElecSus* with the optimised parameters (7.374 kG, 162.9 °C). Including the transmission spectra expected if the incoming light was left or right circular polarised. $I_x$ and $I_y$ are plotted underneath respectively. The red, grey and blue vertical dashed lines are the positions of the red, pump, and blue channel frequencies, respectively. The last plot shows the refractive index of the $\sigma^+$ and $\sigma^-$ component.

The Poincaré spheres in figure 5.9 show the expected polarisation behaviour of the light propagating through a 2 mm vapour cell. The light is essentially linear polarised while crossing the cell, therefore the $S_3$ component vanishes. Figure 5.10 also shows the rotation angle as a function of the cell length calculated by equation (4.2). It is estimated that the red channel will rotate by an absolute angle of $2\pi$ while the blue channel will rotate by $3\pi/2$ by the time the photons reach the end of the cell. Possible dichroic effects of the windows are not taken into account. To estimate the expected performance of the beam splitter it is necessary to know how much of the incoming light

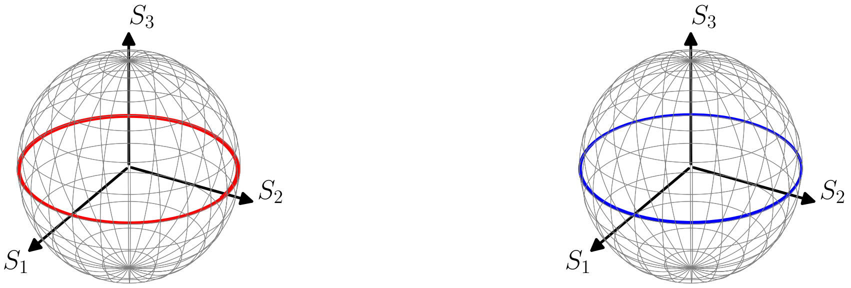

Figure 5.9: Poincaré representation of the polarisation changes of the light in the red and blue (left and right respectively) channel propagating through the 2 mm vapour cell at 7.374 kG and 162.9 °C. The polarisation stays linear thus the $S_3$ component vanishes.

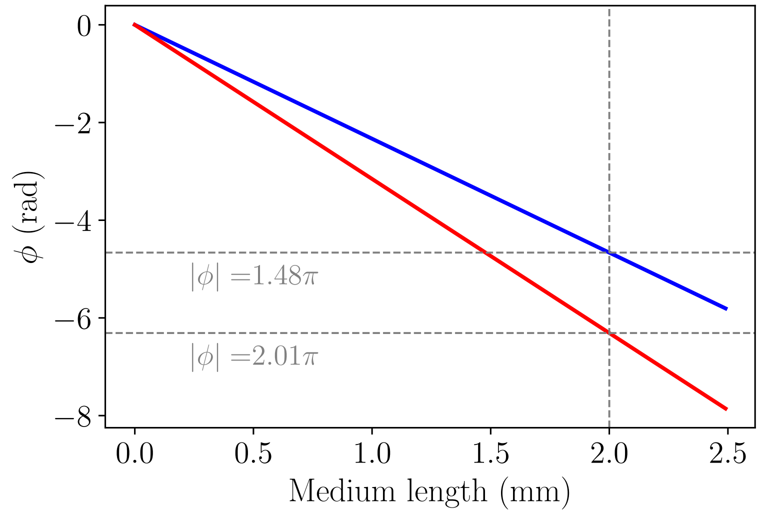

Figure 5.10: Rotation angle introduced to the light in the red and blue channel (top to bottom) by the vapour in the 2 mm cell at 7.374 kG and 162.9 °C. Both channels are rotated in the same direction, however, the rotation magnitude differs by $\approx \pi/2$.

of one channel leaks into the path of the other channel after the last PBS. Assuming the PBS splits the light perfectly, the performance is limited only by the vapour. Table 5.1 shows an estimate of the impurity calculated by equation (5.2). Another accessible property is the extinction introduced in equation (5.3), also present in the table.

Table 5.1: Transmission at the red and blue channel for each polarisation and the resulting impurity of the respective channel for a $^{85}$Rb vapour.

| | $I_x$ | $I_y$ | Impurity | Extinction (dB) |
|---|---|---|---|---|
| Red channel | 0.97 | $8.8 \cdot 10^{-4}$ | $2.2 \cdot 10^{-3}$ | -60.82 |
| Blue channel | $2.1 \cdot 10^{-3}$ | 0.99 | $8.9 \cdot 10^{-4}$ | -53.32 |

According to [54] a typical PBS performs better than an extinction ratio of 1000:1 ($-60\,\mathrm{dB}$) in respect to the polarisation which gets transmitted.

## 5.4 Design of the magnets

To approach the static magnetic fields predicted in section 5.3 for the operation of the cell as an atomic Faraday beam splitter, neodymium magnets are required. These magnets are subdivided into categories which give information about the maximum operating temperature, the temperature-dependent demagnetisation, the brittle nature and magnetic field strength of the respective magnet. In this work magnets of grade N52 were used. This category is assigned to maximum working temperature of 60 °C. Beyond this temperature, irreversible demagnetisation occurs [55].

The magnets were designed to take the shape of the grey area in figure 5.11. This shape allows a design of the magnet holder with a minimal adjustable distance between the magnets [18, 51] as shown in figure 6.2. The drawback of this design is that if the cell holder or magnets are positioned incorrectly, there is a risk of a direct contact between magnet and heat source. In this case the magnets heat up and the loss of magnetisation may become irreversible. Neodymium magnets should be operated in a temperature range were the magnetisation loss due to temperature changes is reversible. In general that is the range between 20 °C and 60 °C for N52 were the demagnetisation is approximately linear [55]. In case of a magnetic field at the position of the cell of 7.374 kG it is $\approx -8.9\,{}^{G}/_{°C}$.

For the calculations of the magnetic field along the propagation axis of the light the equation for a ring magnet is used [44, 56]. By placing four of such cylindrical pieces in the right positions to form magnets pairs like in figure 5.11, separated by a gap, the desired magnetic fields are reachable. The equation for the first segment reads as follows:

$$B(z) = \frac{B_0}{2}\left(\frac{z+\frac{L_1}{2}}{\sqrt{\left(z+\frac{L_1}{2}\right)^2+R_1^2}} - \frac{z-\frac{L_1}{2}}{\sqrt{\left(z-\frac{L_1}{2}\right)^2+R_1^2}}\right) - \frac{B_0}{2}\left(\frac{z+\frac{L_1}{2}}{\sqrt{\left(z+\frac{L_1}{2}\right)^2+r^2}} + \frac{z-\frac{L_1}{2}}{\sqrt{\left(z-\frac{L_1}{2}\right)^2+r^2}}\right). \tag{5.4}$$

$B_0$ represents the remanence of the magnets which is assumed to be $B_0 = 14\,\mathrm{kG}$. $L_1$ is the length of the segment. $R_1$ is the outer radius and $r$ is the radius of the bore through the segment. The gap $g$ between the magnets, were the cell will be positioned in, is adjustable by rotating the magnet mount with the small handle depicted in figure 6.2. Furthermore $z' = z + {}^{L_1}/_2 + L_2 + {}^{g}/_2$ shifts the origin to the position of the cell center. The full equation used to calculate the magnetic field profile is displayed in the appendix, equation (9.1). By constructing a cost function including the lengths and radii of equation (9.1) and minimising it with the *scipy.optimize.minimize* tool, a magnet pair will be obtained, which approaches the target magnetic field very well. The cost function for the magnets is in the appendix subsection 9.3.1 equation (9.2). By placing the constrain $R_1 > R_2$ the desired shape is ensured. In case of a target field of 7.374 kG the optimal parameters found are listed in table 5.2.

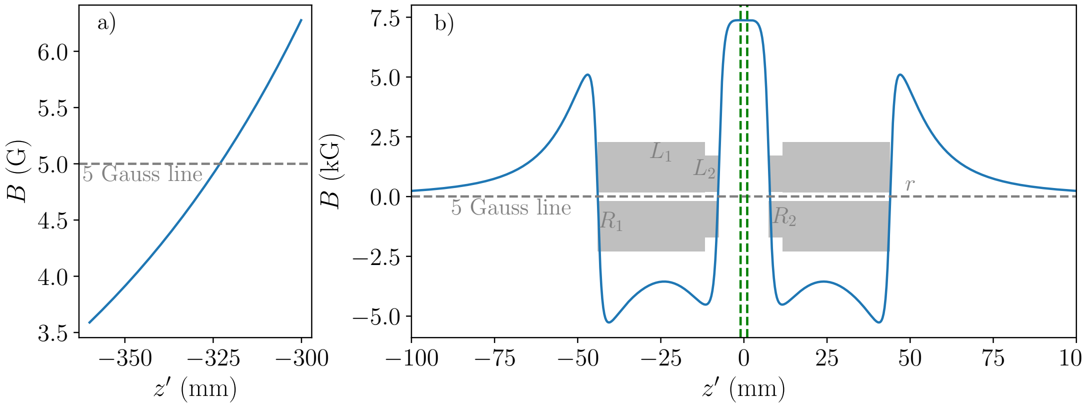

Figure 5.11: The magnetic field profile of the magnet pair. a) The horizontal dashed line is the 5 G-line. The 5 G-line is crossed at a distance of 323 mm in both directions. b) The vertical dashed lines indicate the position of the vapour cell. The grey area is a cross-section of the optimised magnets.

The parameters $R_1$ to $L_2$ are constrained by an upper limit to ensure feasibility in the later experiment. The gap $g$ and the bore radius $r$ have a minimum of 15 mm and 1.5 mm to ensure that vapour cell and heater will fit between the magnets and to ensure that

Table 5.2: Optimised magnet dimensions in [mm].

| $R_1$ | $R_2$ | $L_1$ | $L_2$ | $r$ | $g$ |
|---|---|---|---|---|---|
| 18.24 | 13.66 | 32.33 | 4.15 | 1.5 | 15 |

the laser light can enter the setup. The resulting $B$-field profile is plotted in figure 5.11. Figure 5.12 shows the magnetic profile at the position of the vapour cell. The $B$-field deviates from the target only by $\Delta B \approx 2\,\mathrm{G}$ in the cell interior.

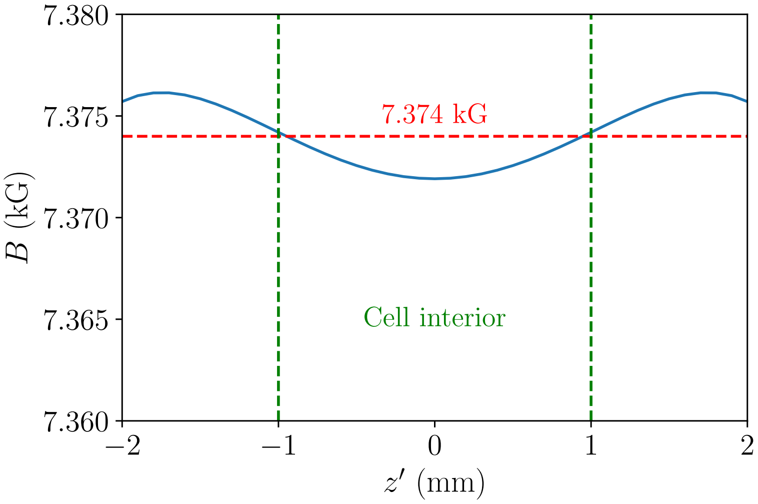

Figure 5.12: Zoom into the magnetic field profile around the cell. The target magnetic field of 7.374 kG is reached. Maximum deviation from target $\Delta B \approx 2\,\mathrm{G}$.

## 5.5 Inhomogeneous magnetic field

Due to possible imperfections in the fabrication process of the magnets, it is important to investigate how the inhomogeneities in the magnetic field will affect the spectra. *ElecSus* has an already implemented function to calculate spectra of a medium within an inhomogeneous $B$-field called *fit_fieldgradient.fieldgrad_fitfn*. For that purpose *ElecSus* uses equation (5.4) to calculate the magnetic field profile inside the cell. Next, the algorithm divides the cell into 25 segments and then calculates the mean magnetic field inside the segments. By consecutively calculating the rotation and absorption in each cell segment and forwarding the results as an input to the next segment a spectrum is generated which fits the observation described in [17].

In this thesis a magnetic field profile with a relatively high inhomogeneity is constructed to investigate the effect of inhomogeneity on the resulting spectra. By reducing the gap to $g = 12\,\mathrm{mm}$ a field profile, as plotted in figure 5.12, is produced. The average of the magnetic field inside the cell is 7.931 kG. Using this profile the spectra in figure 5.14

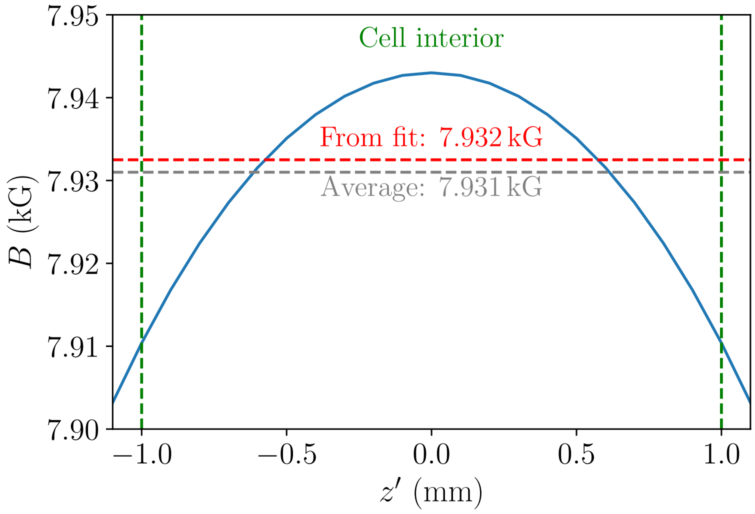

Figure 5.13: Created inhomogeneous magnetic field profile at the cell position. Average magnetic field inside the cell is 7.931 kG. The fit with *ElecSus* converged to 7.932 kG

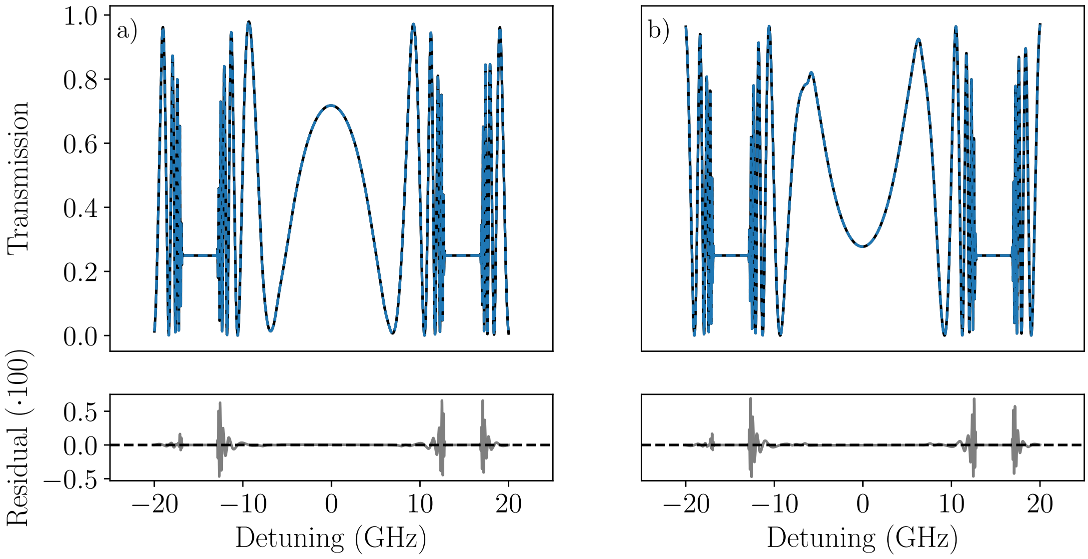

Figure 5.14: Simulated spectra from inhomogeneous magnetic field from figure 5.13 inside the vapour cell. The cell temperature is 163 °C. Both polarisations $I_x$ in a), $I_y$ in b) and their respective fits (dashed lines) show excellent agreement with an rms deviation of 0.07 %. The resulting field strength from the fit is 7.932 kG ($\Delta B \approx 1$ G).

are calculated with 25 segments while constraining $T$ to 163 °C. The resulting data is fitted with *ElecSus* assuming a homogeneous magnetic field. The resulting effective field from the fitting routine leads to 7.932 kG. The difference is $\Delta B \approx 1\,\mathrm{G}$. Furthermore, the residuals of the fits in figure 5.14 are $\approx 5 \cdot 10^{-4}$, showing that the magnetic field inhomogeneity is not the limiting factor in terms of fit accuracy.
If the cell were not exactly aligned in the middle of the magnetic field only affects the strength of the effective $B$-field and is not affecting the fit accuracy.

# 6 Experimental apparatus

Previous experiments which reached similar magnetic fields in vapour cells have already been conducted by [18, 51, 49, 57]. Rubidium vapour cells were used as atomic Faraday beam splitters in preceding works as well [50]. This experimental setup aims to observe the transmission spectra of an isotopically pure $^{85}$Rb vapour cell with and without an applied magnetic field. The recorded spectra will give information on if the desired properties of the vapour, predicted in chapter 5, are attainable. In addition, this study goes further and quantitatively characterises the stability of the setup by measuring the overall suppression of the blue channel in the wrong polarisation over time. These results will be useful for future experiments with atomic vapours in high magnetic fields from permanent magnets. In section 7.1 it is shown that the $^{85}$Rb content in the cell is $(99.844 \pm 0.003)\,\%$. Because of this slight deviation from the assumed parameters discussed in section 5.3, the optimised magnetic field and temperature deviate slightly from 162.9 °C and 7.374 kG to 162.8 °C and 7.366 kG. This has no notable consequence for the performacne of the atomic faraday filter. The photo-detectors used are constructed

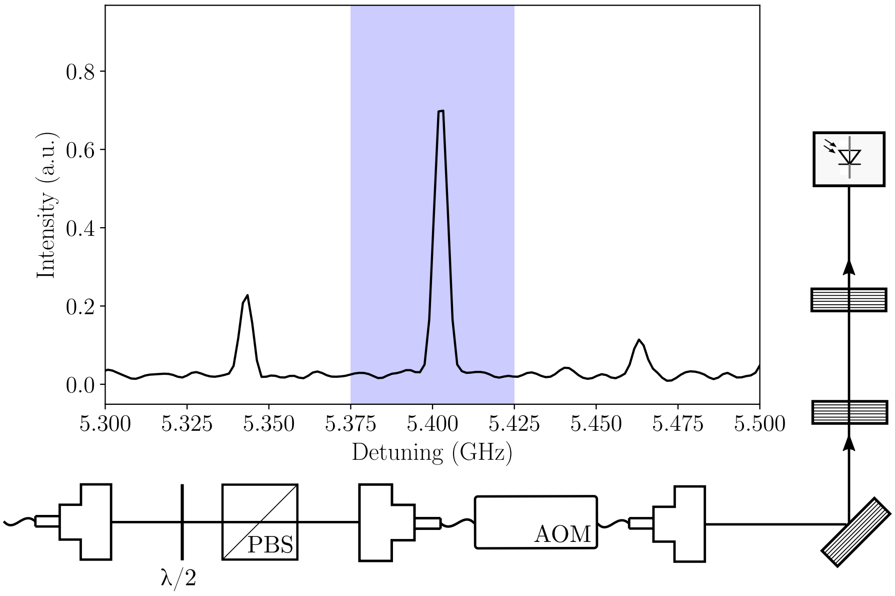

Figure 6.1: Setup to create the reference peaks for side-of-fringe laser locking. The insert shows the signal from the ultra low expansion (ULE) cavity at the region of interest (blue marker) at 5.4 GHz ±25 MHz detuning (blue channel). Etalon peaks are present in this range.

and designed as part of the work for this thesis. The schematics and parts used are listed in the appendix section 9.4. Spectra recorded by photo-detectors other than the ones previously mentioned are identified as such. The laser used throughout this thesis is a Toptica DL pro grating stabilised at 795 nm. The laser is operated in both scanning and locked mode. However, since the magnetic field shifts our spectrum away from the reference resonances it is impractical to lock the laser on the red or blue channel using a simple reference cell. A temperature stabilised ultra low expansion (ULE) cavity in combination with an acousto-optical modulator (AOM) is used to circumvent this limitation. Another possible solution would be to use a second cell in a similar magnetic field for laser locking as mentioned in [58]. By locking on a side-band, generated by the AOM, close to the blue channel an estimation of the stability of the atomic Faraday filter is possible (see section 7.3). Figure 6.1 shows a simplified version of the setup used for the laser locking with a sample of the position of the transfer cavity resonances of this setup. The blue area marks the region of interest. The used 2 mm vapour cell has no anti-reflective coating. The loss through the cell is measured to be ≈ 13 %, measured with a cold cell by an off resonant laser.

## 6.1 Design of the magnet mount

The inspiration for the magnet mount was taken from [18, 51]. The final design is depicted in figure 6.2. As previously stated in section 5.4 the magnets have to be in close proximity (≈ 15 mm) to each other. At this distance there is a considerable force ($F \approx 100\,\mathrm{N}$)[1] acting on the magnets. Therefore the mount has to be stable enough to not budge under the weight. Equation (6.1) describes the shear modulus $G$ and allows to roughly estimate, if the design is capable of handling the force.

$$G = \frac{F \cdot l'}{A \cdot \Delta x}. \tag{6.1}$$

$F$ is the applied force and $l'$ the height of the point of application relative to base plate $A$. $\Delta x$ represents the transverse displacement. The shear modulus of aluminium is $G_{\mathrm{Al}} = 26,49\,\mathrm{GPa}$ [60]. The area of the base plate is extracted from the technical drawing (appendix 9.5). It amounts to $A = 120\,\mathrm{mm} \cdot 30\,\mathrm{mm} = 3600\,\mathrm{mm}^2$, tolerances not considered. The point of application of the force coincides with the center of the magnets at $l' = 105\,\mathrm{mm}$ height. This corresponds to a transversal displacement of $\Delta x = 1.1 \cdot 10^{-4}\,\mathrm{mm}$ on each side, therefore it can be considered stable. Additional Peltier-elements are installed at both sides of the magnet holders pedestal. A Pt-100 thermistor monitors the temperature at a position on the magnet holder insert (figure 6.2) close to the magnets. A proportional–integral–derivative controller (PID) then stabilises the temperature of the magnet holder by regulating the Peltier-elements. Four heat pipes transfer the excess heat from the thermoelectric devices to two fan coolers. With this electronic cooling solution it is possible to control the temperature of the magnets in a precise manner.

---

[1] The force was calculated in *FEMM v 4.2. Results shown in the appendix subsection 9.3.2* [59].

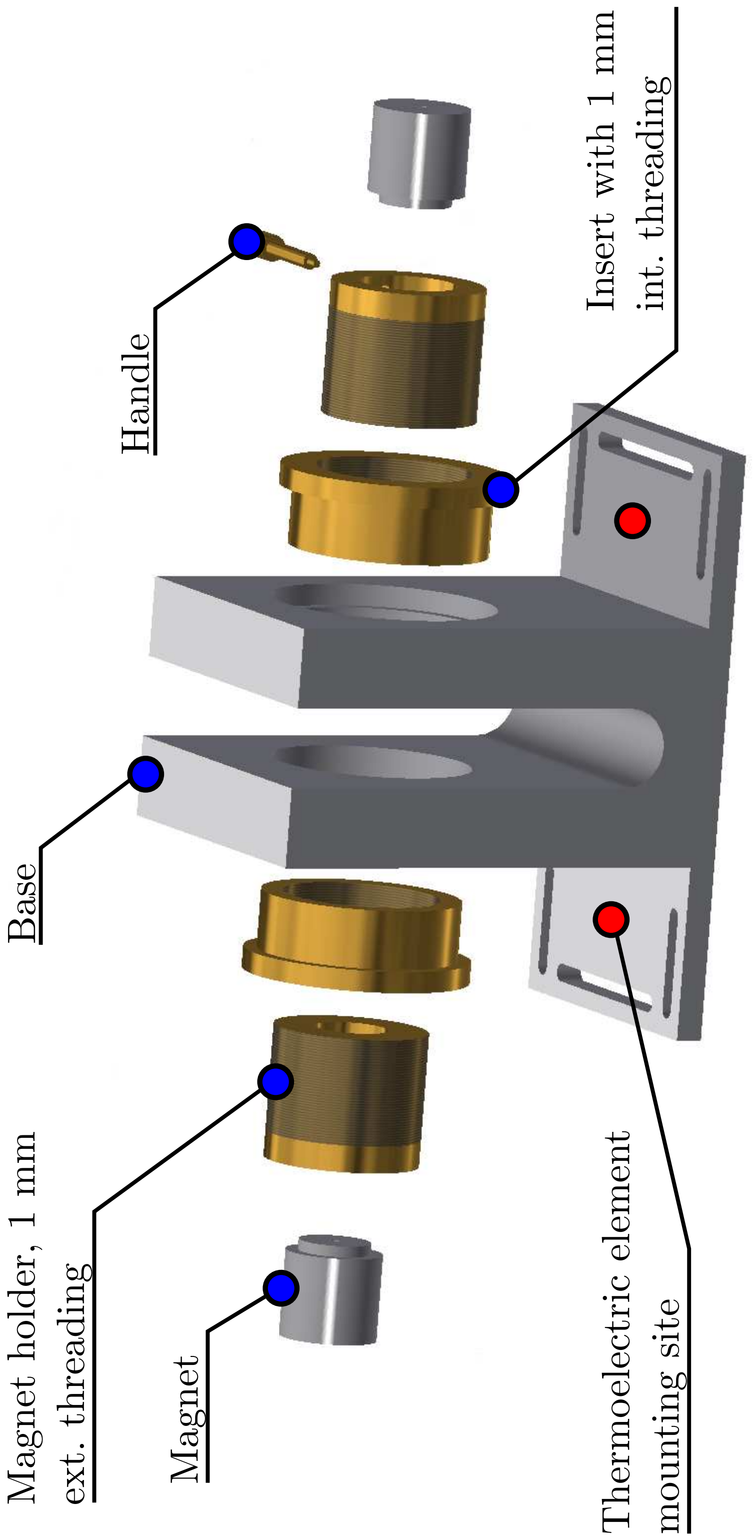

Figure 6.2: Explosion drawing of the magnet holder. From left to right: magnet (grey), magnet holder with 1 mm exterior threading (brass), magnet holder insert with 1 mm interior threading (brass), table mount (big grey object).

## 6.2 Temperature related reversible demagnetisation

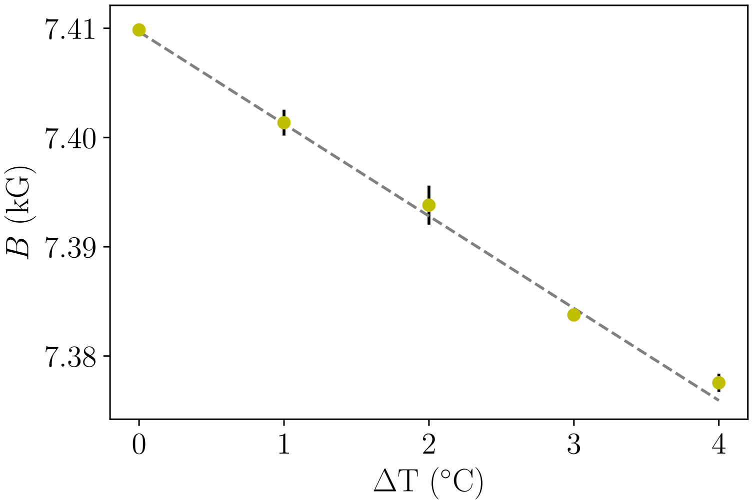

Figure 6.3: Magnetic field at different temperatures. The temperature difference $\Delta T = 0\,^\circ\mathrm{C}$ corresponds to room temperature ($21\,^\circ\mathrm{C}$). Each data point consists of the average of five consecutive measurements. The standard error for each data point from the five measurements is represented by the black bars. A linear function was fitted to the data with a weighted least-square fitting routine. The intercept and demagnetisation rate amount to $(7.410 \pm 0.001)\,\mathrm{kG}$ and $(-8.4 \pm 0.4)\,{}^{\mathrm{G}}/_{\mathrm{K}}$, respectively.

To demonstrate the temperature dependent demagnetisation, the magnets are temperature stabilised near room temperature $21\,^\circ\mathrm{C}$ ($\Delta T = 0\,^\circ\mathrm{C}$) by the thermoelectric elements and the PID controller to define the reference magnetic field. The magnetic field is determined by the fitting of the spectroscopy data from the setup in section 7.2 with *Elecsus*. Each polarisation component $(I_x, I_y)$ is fitted separately and the mean value was taken as the measurement point. The set point of the temperature controller is increased by $1\,^\circ\mathrm{C}$. After approximately 1 h the setup temperature is not fluctuating any more and the spectra are recorded. Additional data points are taken in the same manner. Each point in figure 6.2 consists of the average of five consecutive measurements. For each point the standard error is calculated and included in the figure. The data points are then fitted linearly with a weighted least-square fitting routine. The resulting demagnetisaion rate is $(-8.4 \pm 0.4)\,{}^{\mathrm{G}}/_{^\circ\mathrm{C}}$ the resulting intercept is $(7.410 \pm 0.001)\,\mathrm{kG}$. The expected demagnetisation rate is $-8.9\,{}^{\mathrm{G}}/_{^\circ\mathrm{C}}$ according to [55], thus the two numbers are in agreement.

The measured effective magnetic field does not match the optimised requirements from section 5.3. In order to correct the deviation the distance between the magnets is increased until the effective magnetic field is in the range of $\Delta B \approx -20\,\mathrm{G}$ to the desired field. Afterwards the magnets are cooled down to the temperature necessary to reach the optimised $B$-field, approximately 3 °C below ambient. Our setup reached $(7.365 \pm 0.001)$ kG. This process does not drastically affect the homogeneity of the magnetic field.

## 6.3 Design of the cell heater

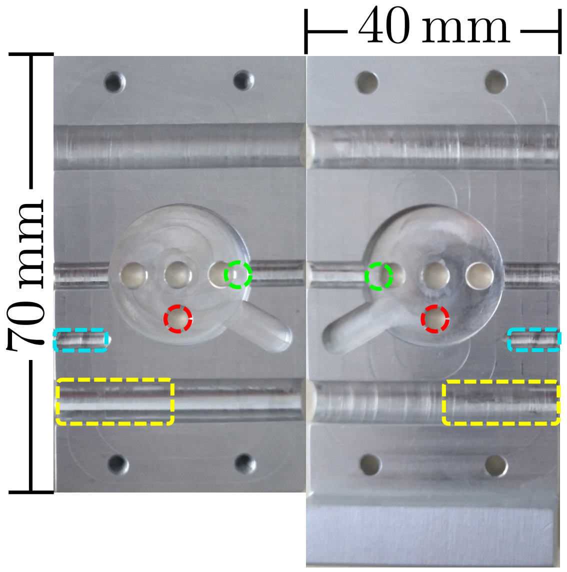

Figure 6.4: Photography of the cell heater. From top to bottom: Rubidium condensation site (green), entering and exit point laser beam (red), hole for the PT100 thermistor (blue) and position of the heating cartridge (yellow). Device dimensions are in the appendix in section 9.5.

The requirements of the heater are sometimes in contradiction to each other. For instance a low thermal mass can be beneficial in terms of temperature rise times, but is disadvantageous in terms of thermal stability. A higher thermal mass would lead to better thermal stability, but it could also heat up the magnets, causing demagnetisation. Therefore a low thermal mass with active temperature stabilisation approach is chosen. Similar designs have been demonstrated in [18]. Device dimensions and specifications are exhibited in the appendix in section 9.5. The temperature of the vapour cell is stabilised using a PID controller in combination with a PT100 thermistor.
The rubidium vapour will condense at the point in the cell with the lowest temperature. This is typically were the cell is exposed to air the most, for instance, were the laser beam enters. Over time this leads to degrading performance since the rubidium condensate forms a barrier for the light. In the design it is attempted to control were the condensation will occur by using a heating cartridge with a length of only half the heater's width. By placing it at the edge of the heater a point with maximal exposure to air is created while being further away from the heat source. Figure 6.4 shows the

finished cell heater. A temperature of $(162.87 \pm 0.01)$ °C is reached and maintained with this design. The temperature is also extracted from the spectrum in the same manner as the magnetic field, with shorter pause to reach thermal equilibrium ($\approx 10\,\mathrm{min}$).

# 7 Experimental results

## 7.1 Transmission spectroscopy

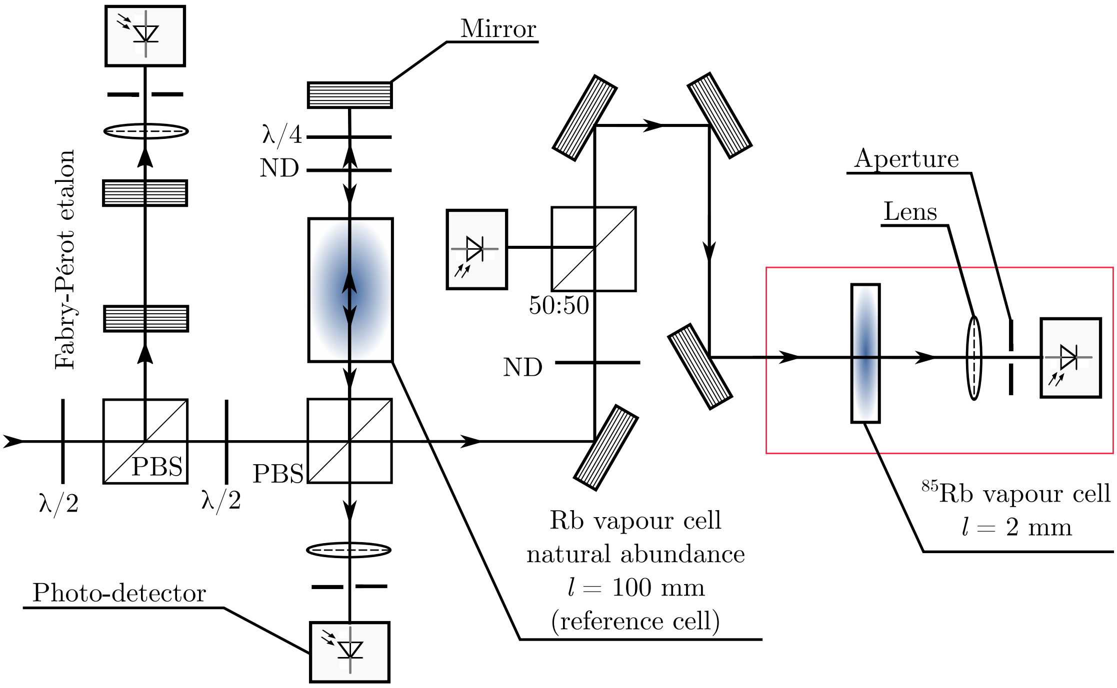

Figure 7.1: Setup for transmission spectroscopy. From left to right: Fabry–Pérot etalon consisting of two planar mirrors, Sub-Doppler spectroscopy reference setup for laser calibration as described in chapter 4.2, intensity shape monitoring setup of the scanned laser, transmission spectroscopy setup with the 2 mm rubidium-filled vapour cell. The $\lambda/2$-plates and the PBS's allow the amount of power directed in each direction to be controlled. The ND filter attenuates the laser to reach the weak probe regime [26]. The four mirrors are installed for better beam alignment control. The lens after the vapour cell collects the light and focuses it down to the photo-detector through a pinhole which blocks stray room light.

The setup shown in figure 7.1 is used to determine the actual $^{85}$Rb content in the 2 mm cell. The cell is heated to 148 °C. At this temperature the transitions associated with $^{85}$Rb become optically thick and the number density of $^{87}$Rb is high enough to be visible in the measurement. The spectra are recorded using an amplified photodiode connected to a LeCroy WaveRunner 44mxi-A oscilloscope. The laser scan profile was recorded separately as discribed in subsection 4.2.4. Five consecutive spectra are taken, calibrated and then fitted with *ElecSus*[16, 17]. The calibration process is described in section 4.2. Figure 7.2 shows one of the fitted data sets mentioned above. The rubidium content and temperature were fit parameters. Deviations from the theory can be attributed to imperfections in the compensation of the signal shape $V(\Delta) = R \cdot I_0(\Delta)$ of the laser scan profile, as well as the finite accuracy of the frequency calibration process. However, with an rms deviation of 1.01 % the theory shows very good agreement with the measurements. The resulting $^{85}$Rb content amounts to $(99.844 \pm 0.003)$ % (average of the abundance extracted from the five spectra).

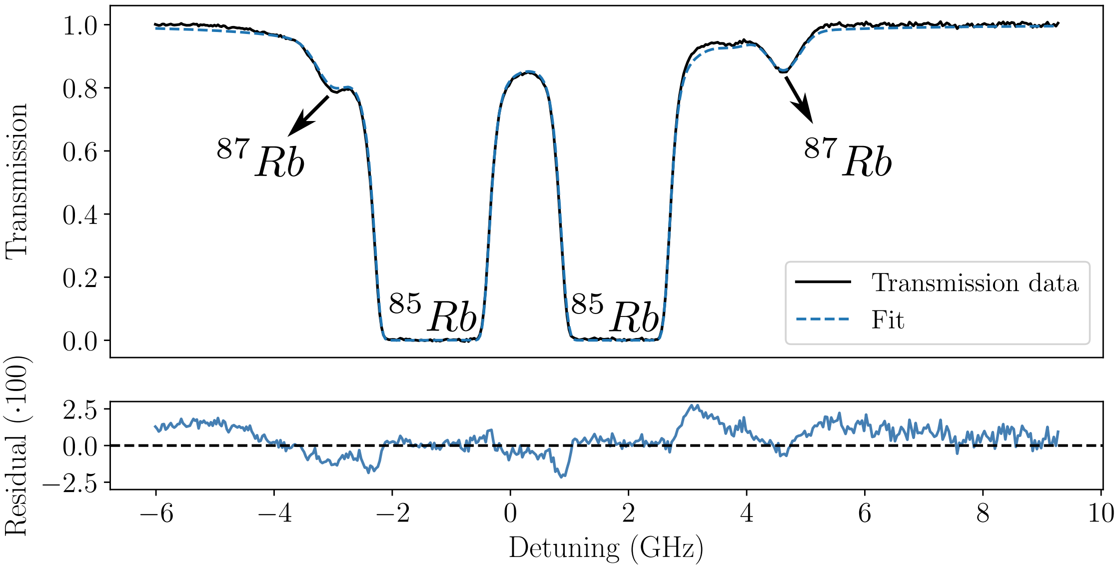

Figure 7.2: Above: Transmission spectrum of the 2 mm cell at 148 °C fitted to theory (dashed line). Below: Residual from fit, the rms deviations amounts to 1.01 %. This data is used to determine the $^{85}$Rb content. This spectrum is recorded by a Thorlabs DET36A/M photo-detector.

As a next step the setup is augmented with a magnetic field to test the quality of the custom magnet pair, as shown in figure 7.3. This is achieved by placing the cell heater in between the two permanent magnets designed in section 5.4. The magnets are embedded in the holder shown in figure 6.2. Five spectra are taken in fast succession and the average $B = (7.462 \pm 0.001)$ kG and $T = (147.2 \pm 0.3)$ °C are extracted from the fits. The resulting transmission spectrum is shown in figure 7.4. This experiment demonstrated that the magnet pair can reach the required magnetic field strengths for the operation of the atomic Faraday beam splitter.

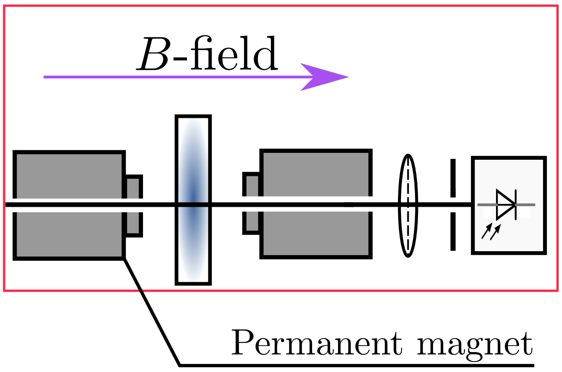

Figure 7.3: Augmented setup for transmission spectroscopy with applied magnetic field. The cell is positioned between the magnets in the magnet holder (from section 6.1) by an external mount.

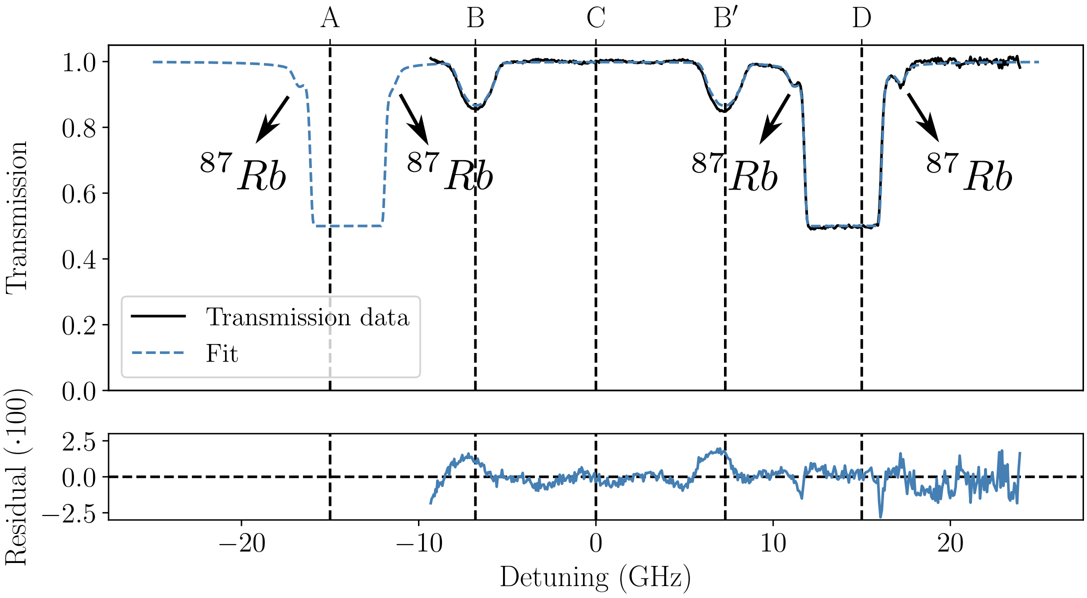

Figure 7.4: Transmission spectrum at the $D_1$-line. The vapour parameters are $(7.462 \pm 0.001)$ kG and $(147.22 \pm 0.26)$ °C. The prominent absorption lines (A,D) correspond to the $\sigma^{+,-}$ transitions of $^{85}$Rb. The smaller side peaks are due to the remaining $^{87}$Rb content while the additional two distinctive peaks (B,B′) are the weak transitions. C is the position of the weighted line center. The fit (dashed line) exhibits an rms deviation from the data of $= 0.75\,\%$. The dashed vertical lines labelled from A to D are the detunings marked in figure 7.5.

In the next paragraph it is attempted to explain the feature visible in the spectrum of the rubidium vapour in a magnetic field. The most prominent features in figure 7.4 are the absorption peaks at marker A and D. They originate from the transitions $\Delta m_J = -1, +1$ ($\sigma^-$,$\sigma^+$ respectively) shown in figure 7.6 and are the main transitions of $^{85}$Rb. The two absorption peak in the markers B and B' are the weak transitions. They originate from the admixture of the $m_J = 1/2$ and $m_J = -1/2$ states even in high $B-$fields. They are $\sigma^+$ and $\sigma^-$ from left to right respectively and disappear with increasing field strength. The transitions in figure 7.4 are therefore A: $\sigma^-$, B: $\sigma^+$, B$'$: $\sigma^-$ and D: $\sigma^+$. This behaviour is also visible in the theoretical plots in figure 5.8 in section 5.3. The wave function of the separate states is therefore written as $|\Psi\rangle = a\,|m_J\rangle + b\,|m'_J\rangle$. Stretched states with the quantum number $m_F = \pm 3$ do not display an admixture. The weak transitions and the corresponding eigenvectors are also displayed in figure 7.6. The signal from the remaining $^{87}$Rb content which amounts to $(0.15 \pm 0.01)\,\%$ is visible right next to the optically thick $^{85}$Rb transition which is $\sigma^+$ as well.

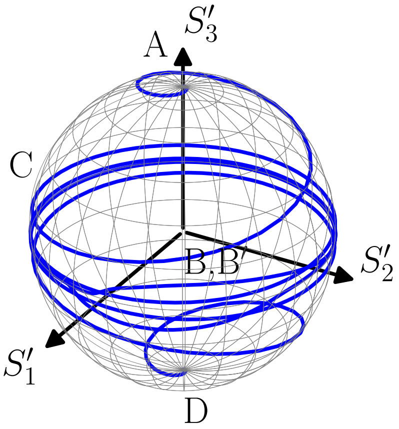

Figure 7.5: This figure shows the calculated development of the normalised Stokes parameters S$'_i$ of x-polarised light entering a cell with temperature and magnetic field of $(147.2 \pm 0.3)$ °C and $(7.462 \pm 0,001)$ kG while being scanned from $-15$ to 15 GHz detuning.

Since the incoming light is linearly polarised, half of the light gets transmitted at the markers A and D. The outcoming light is then left-circularly polarised while the medium is optically thick for the right-circularly polarised component and vice versa. Figure 7.5 shows the development of the Stokes parameter over a range from $-15$ GHz to 15 GHz in the shape of a Poincaré sphere calculated with the fit parameters from figure 7.3. It starts at $S'_3 = 1$ with the other components vanishing at marker A. With increasing detuning the circular polarised light becomes more elliptical, until it eventually turns into linear polarised light around marker C, therefore $\sqrt{S'^2_1 + S'^2_2} = 1$. The weak transitions are visible in the Poincaré sphere in figure 7.5 as small bumps. When the probe laser enters the blue detuned regime the linear polarisation begins to become elliptical again until it becomes circular with $S'_3 = -1$ at the marker D.

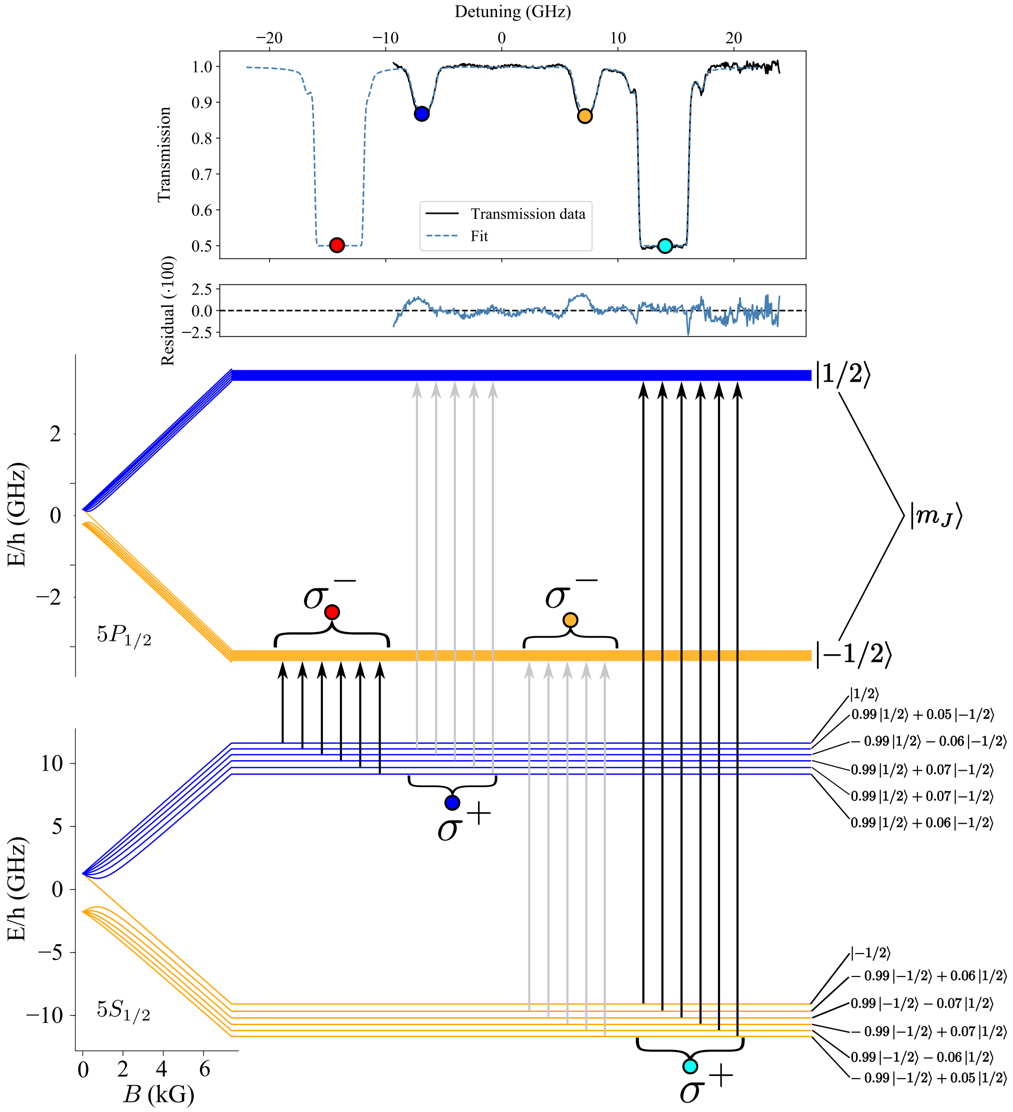

Figure 7.6: The transmission spectrum originates from figure 7.4. Bottom: Hyperfine Paschen-Back energy scheme for the $^{85}$Rb D$_1$-line at a magnetic field of 7.462 kG calculated by the Breit-Rabi formula (3.8). The excited manifold separates into 12 eigenstates which form groups of 6. Orange corresponds to $m_J = -1/2$ and blue to the $m_J = 1/2$ states. Within each group the separation of eigenstates is small compared to the ground state. The ground manifold on the other hand experiences a bigger separation also into 12 eigenstates in groups of 6. The black arrows mark the main transitions $\Delta m_J = \pm 1$ corresponds to $\sigma^+$ and $\sigma^-$ respectively. The weak transitions are represented by the grey arrows. They originate from the admixture of $m'_J$ with the main quantum number. The states of the ground manifold are labelled with the respective eigenvectors $|\Psi\rangle = a\,|m_J\rangle + b\,|m'_J\rangle$.

## 7.2 Polarisation dependent spectroscopy

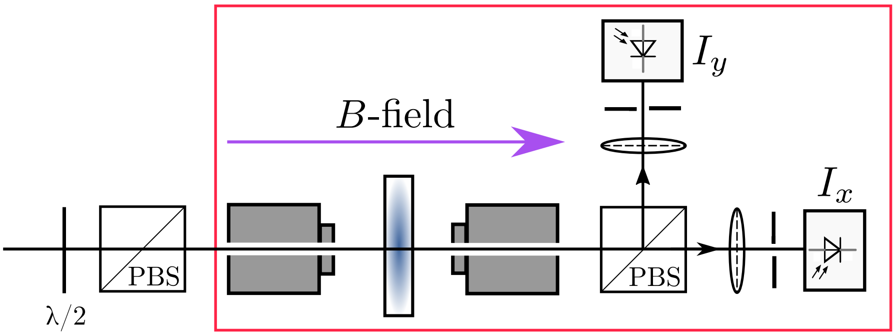

Figure 7.7: Setup to measure the polarisation dependent signal of the cell. The setup from figure 7.3 is augmented by a $\lambda/2$-plate and additional polarising beam splitters before and after the cell. The PBS defines the polarisation of the light emitted into the cell, while the plate is maximising the light transmitted through the PBS. It is mounted on a rotatable stage in order to align the polarisation plane of the two PBSs. The PBS after the cell separates the polarisation components and directs them to a separate photo-detector. The rest of the setup in figure 7.1 is unchanged.

The magnetic field is adjusted by moving the magnets further apart, since the previous chapter showed that it is too large. The remaining deviation from the optimum is mitigated by the temperature stabilisation of the magnets as discussed in section 6.2. The setup is augmented with a $\lambda/2$-plate, with a PBS on a rotatable stage and a PBS after the cell, as shown in figure 7.7. The PBS before the cell is defining the incoming polarisation. The PBS after the cell separates the light coming from the cell in its polarisation components, enabling the polarisation dependent spectroscopy.

To define the incoming polarisation accurately the power reflected on the PBS after the cell is minimised. This is achieved by rotating the first PBS until the polarisation plane defined by it matches the polarisation plane defined by the second PBS. The alignment is performed while the cell is at room temperature in order to partially correct for possible birefringent cell walls. The $\lambda/2$-plate is then adjusted to maximise the transmission through the cube before the cell. Then the PBS is reorientated recursively.

After the cell reached the aimed temperature the apparatus reaches thermal equilibrium within 2 h. Afterwards five spectra are recorded in fast succession and fitted with *ElecSus*. One of the data sets is visible in figure 7.8. An interesting feature of this figure is that the saturated $\sigma^+$ transitions split evenly with 25 % of the light being transmitted into both $I_x$ and $I_y$ arms. This confirms the circular nature of the remaining transmitted light at resonance. The parameters are extracted from the fit in the same manner as previously, resulting in a magnetic field of $(7.362 \pm 0.001)$ kG and a temperature of $(162.86 \pm 0.01)$ °C. The optimised field strength and temperature defined in section 5.3

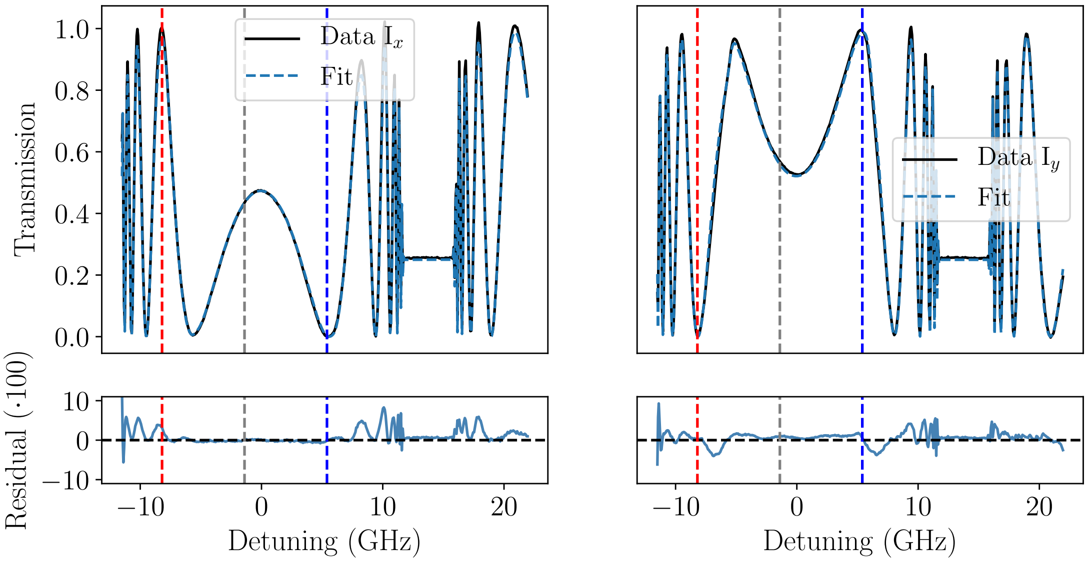

Figure 7.8: Transmission $I_x$ (left) and $I_x$ (right) with their respective fits around the position of the blue and red channels (vertical dashed lines, the pump detuning is indicated by the dashed line in the middle). The fit confirmed a magnetic field of $(7.362 \pm 0.001)$ kG and a temperature of $(162.86 \pm 0.01)$ °C. The rms deviation of the $I_x$ arm amounts to 2.09 % and 1.72 % in the $I_y$ arm.

are therefore reached. The impurities for this atomic Faraday filter are calculated using the parameters from the fits and equation (5.2). The impurity is $2.5 \cdot 10^{-3}$ for the red and $1.1 \cdot 10^{-3}$ for the blue channel. It is to note that the impurities stated in this thesis are a lower bound. The performance is limited by the linewidth of the incoming photons for each channel and the performance of the PBS.

## 7.3 Stability estimate

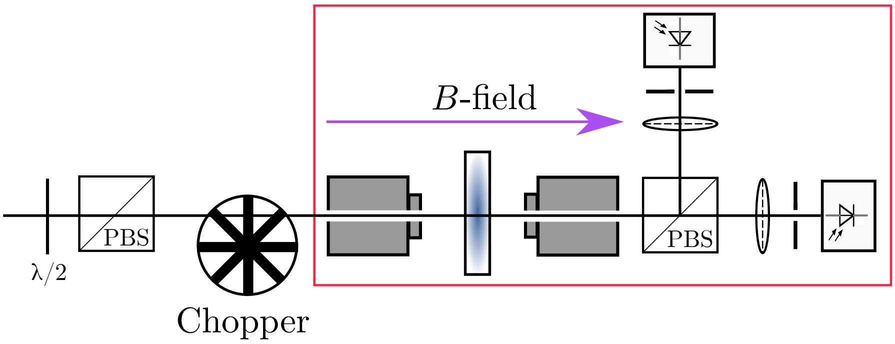

Figure 7.9: Setup for stability estimate. From left to right: $\lambda/2$-plate and PBS to define the polarisation of the incoming light, optical chopper operated at 430 Hz. The rest of the setup is identical to the one in figure 7.7.

With the experimental setup displayed in figure 7.9 the stability of the atomic Faraday beam splitter is determined. This is done by examining the attenuation of the blue channel in the wrong polarisation arm, as described in equation (5.3). It is to be noted that it is sufficient to only consider one of the channels, since we are only interested in stability. If the device is stable the attenuation stays constant as well. For the purpose of comparability the expected attenuation depending on the detuning is displayed in figure 7.10. The curve was calculated using the adapted optimised parameters of this cell. An optical chopper is used to modulate the signal. By fast-Fourier transforming (FFT) [15] the signal of each photo-detector the attenuation of the atomic Faraday filter can be calculated (equation (5.3)). The Fourier transformation has also the advantage, that any constant offset of the photo-detectors or any signals other than the chopper are not affecting the result. The optical chopper was set at a chopping frequency of 430 Hz. This frequency avoids multiples of 50 Hz, because signals from power lines and lighting in the room are at these frequencies.

To measure the maximal attenuation of the last PBS the two beam splitter were crossed. This is the configuration, were the least amount of light is transmitted by the PBS after the cell [54]. The vapour cell is kept at room temperature during this measurement. The probe laser is kept free running (no scanning), since no rotation of the light in the cell is expected. The oscillating signal was averaged 20 times. 10 waveforms were recorded in total in this measurement. A sample FFT signal is shown in figure 7.11. The resulting amplitudes at the 430 Hz indicate that this is the signal modulated by the chopper. It is to note, that the systematic error in this system is governed by how well the setup is aligned and by the difference in reactivity of the photo-detectors, which amount to $\approx 10\,\%$. The result is a systematic error of $\Delta L_{sys} \approx \pm 2\,\mathrm{dB}$ for the attenuation values obtained through this measurement. The attenuation is determined to be $(-82.00 \pm 0.03 \pm 2)\,\mathrm{dB}$ and is also marked in figure 7.10.

For the stability measurement the PBS's are returned into the previous position, where

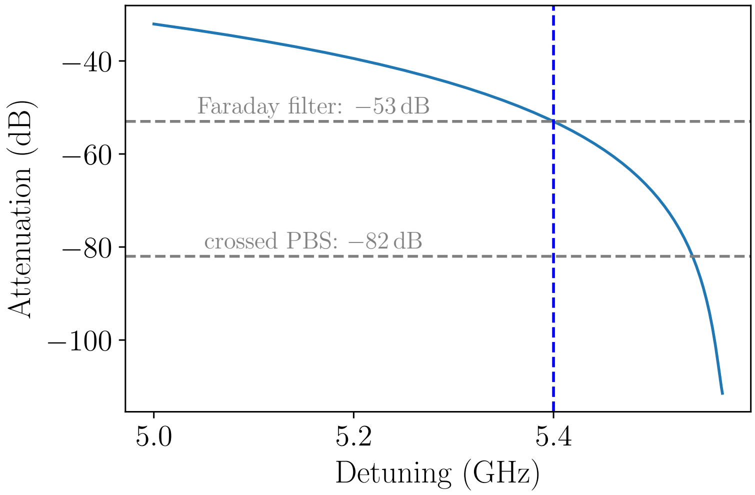

Figure 7.10: Expected attenuation in dB for optimised case. The levels of attenuation of the atomic Faraday filter at the blue channel, as well as the maximal measured attenuation of the PBS.

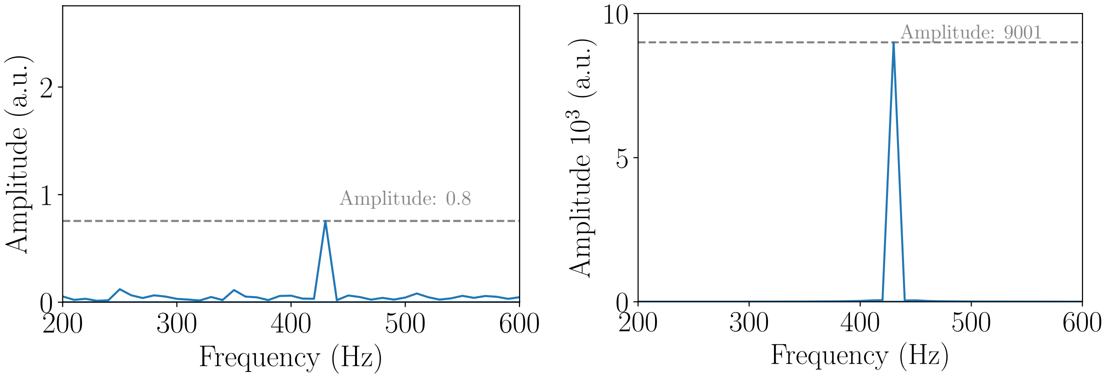

Figure 7.11: FFT signal of the two polarisation arms at 430 Hz with cell at room temperature. Left: For the reflected components. Right: For the transmitted components. The amplitude ratio is used to calculate the attenuation $(-82.00 \pm 0.03 \pm 2)$ dB.

the transmitted arm is $x$-polarised in each beam splitter. The cell is then heated to the optimal temperature and the laser is locked at the blue channel with the setup introduced in figure 6.1. The averaged waveform (20 times) is captured every three minutes. The measurement duration amounted to 15 h. The attenuation is extracted and the resulting profile is visible in figure 7.12. Notably the attenuation of the atomic Faraday filter is changing fast in the first 3 h. This can be attributed to the the fact, that the magnets have to be in thermal equilibrium to reach and stabilise the desired magnetic field strength. The drift in attenuation amounts to $(0.20 \pm 0.01)$ dB/h, therefore it can be concluded, that the atomic Faraday beam splitter is stable during the period under consideration.

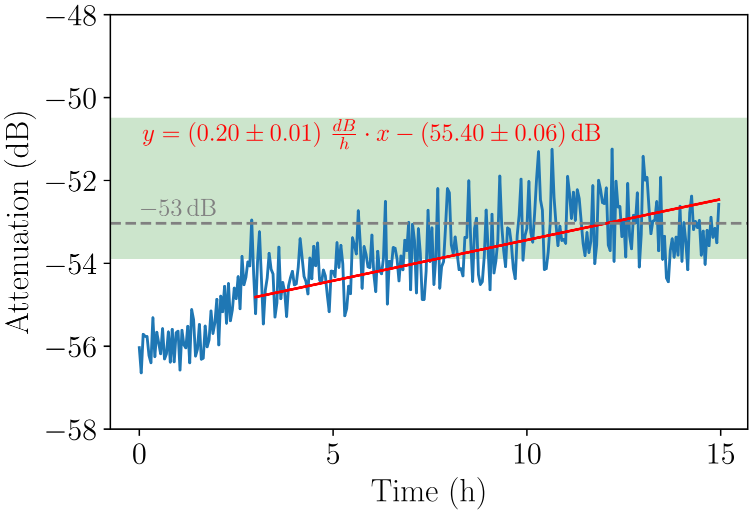

Figure 7.12: Estimate of the stability of the atomic Faraday filter by monitoring the attenuation of the blue channel. The green bar indicates the attenuation of the filter for a temperature fluctuation of $\Delta T = \pm 0.02\,°\mathrm{C}$ of the cell at the end of the series. The drift in attenuation is quantified to be $(0.20 \pm 0.01)$ dB/h. The grey line at −53 dB corresponds to the theoretically predicted attenuation from figure 7.10.

# 8 Conclusion

In conclusion this thesis has successfully demonstrated the use of computational optimisation to design a working atomic Faraday beam splitter for a heralded single photon source. This has been achieved by identifying a working scheme for an isotopicaly pure $(99.844 \pm 0.003)$ % $^{85}$Rb atomic rubidium vapour in a 2 mm cell and a high magnetic field environment.

The software *ElecSus* [16, 17] and *Scipy* [15] have been used to map and optimise the rubidium vapour in terms of performance. The Python library *Scipy* was also used to design the permanent neodymium magnets which generated the high magnetic field necessary for the operation of the atomic Faraday beam splitter. In the process this thesis showed that inhomogeneity in the magnetic field can be approximated with an effective homogeneous magnetic field. The magnitude of this effective field is the average of the field in the cell.

With the required parameters at hand the vapour cell heater and the magnet holder were designed. To mitigate for the drawbacks of the chosen design of the magnet holder active cooling solutions were implemented. This enabled a precise control of the magnetic field via the magnet temperature. Both of the devices were actively temperature stabilised with a PID controller.

This precise control over magnetic field and temperature has helped to achieve the optimised parameters. The reliability of the device has also been tested with a stability measurement over 15 h. This has shown that the device is capable of running stable over an extended period of time, thus making FWM in hollow core fibres feasible as a heralded single photon source.

## 8.1 Outlook

The atomic Faraday beam splitter will be interfaced with an FWM device in order to separate the produced photon pair. This will allow further characterisation of the atomic Faraday beam splitter in terms of measured purity of the channels. A proposal on how to achieve this, is to introduce an etalon or interference filter at one of the channel outputs and comparing the signal intensities, similar to what has been done in section 7.3 in this thesis and in [50].

The cost function used to design the rubidium vapour in equation (5.1) can be modified to account for the finite linewidth of the incoming photon pair. This will become necessary whenever the linewidth of the incoming light is not negligible compared to the minimum and maximum of the polarisation dependent rubidium spectrum it is located in. The new cost function can either include an impurity term by simply adding it to the end of each case in equation (5.1) or expand each term in the same equation to include the line shape.

Further investigation is needed in the high pump detuning regime, since it holds the promise of very high performance. Here a small teaser for the reader:

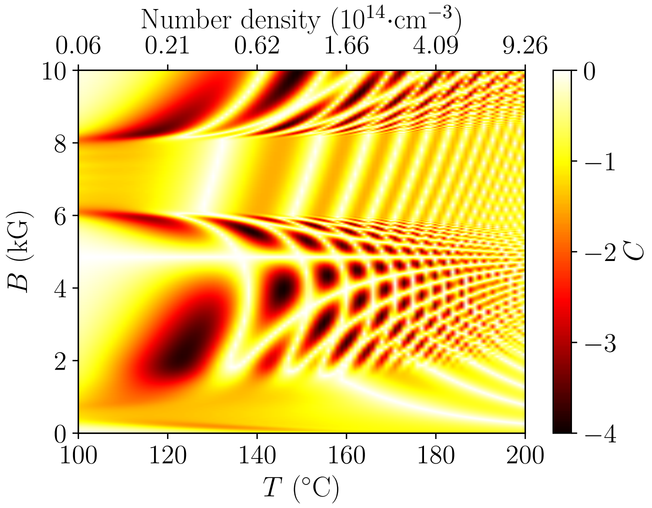

Figure 8.1: Teaser at a pump detuning of $\Delta_p = 6.4\,\text{GHz}$ and $\nu_s = 6.8\,\text{GHz}$ for a 99.89 % $^{85}$Rb cell. The lowest cost value is $C = -3.97$ at $B = 10.167\,\text{kG}$ and $T = 150.3\,°\text{C}$.

The author is convinced, that the popularity of light rotating devices, like the one presented in this theses, will be even grater than the popularity of rotisserie chicken in the future.

# 9 Appendix

## 9.1 Tables of important constants

Table 9.1: Constants used in equation 2.24 to calculate the atomic number density.

| Phase | A | B | C |
|---|---|---|---|
| Rb (solid) | 4.857 | -4215 | - |
| Rb (liquid) | 8.316 | -4275 | -1.3102 |

Table 9.2: Atomic data for rubidium and spectroscopic data for the $D_1$-line.

$^{85}$Rb

| Property | Symbol | Value | Reference |
|---|---|---|---|
| Atomic mass | $m$ | $84.911789732(14)\,\mathrm{u}$ | [61] |
| Nuclear spin | $I$ | $5/2$ | - |
| Nuclear spin $g$-factor | $g'_I$ | $-0.0002936400(6)$ | [62] |
| Magnetic dipole constant ($5S_{1/2}$) | $A_{hf}$ | $1011.910813(2)\,\mathrm{MHz}\cdot\mathrm{h}$ | [62] |
| Magnetic dipole constant ($5P_{1/2}$) | $A_{hf}$ | $120.640(20)\,\mathrm{MHz}\cdot\mathrm{h}$ | [63] |

$^{87}$Rb

| | | | |
|---|---|---|---|
| Atomic mass | $m$ | $86.909180520(15)\,\mathrm{u}$ | [61] |
| Nuclear spin | $I$ | $3/2$ | - |
| Nuclear spin $g$-factor | $g'_I$ | $-0.0009951414(10)$ | [62] |
| Magnetic dipole constant ($5S_{1/2}$) | $A_{hf}$ | $3417.34130545215(5)\,\mathrm{MHz}\cdot\mathrm{h}$ | [64] |
| Magnetic dipole constant ($5P_{1/2}$) | $A_{hf}$ | $406.147(15)\,\mathrm{MHz}\cdot\mathrm{h}$ | [63] |

$D_1$-line

| | | | |
|---|---|---|---|
| Wavelength (vacuum) | $\lambda$ | $794.979014933(96)\,\mathrm{nm}$ | [65] |
| Wavevector | $k$ | $7903586.371\,\mathrm{m}^{-}1$ | - |
| Frequency | $\nu$ | $377.107385690(46)\,\mathrm{THz}$ | [65] |
| Decay rate | $\Gamma$ | $2\pi\cdot 5.746\,\mathrm{MHz}$ | [66] |

Table 9.3: Fundamental constants used in manual calculations in this thesis[18]. *ElecSus* updates the constants it uses automatically [18].

| Quantity | Symbol | Value |
|---|---|---|
| Electron spin $g$-factor | $g_S$ | 2.00231930436153(53) |
| Bohr magneton | $\mu_B$ | $9.27400968(20) \cdot 10^{-24}\,{}^{J}\!/_{\mathrm{T}}$ |
| Boltzmann constant | $k_B$ | $1.3806488(13) \cdot 10^{-23}\,{}^{J}\!/_{\mathrm{K}}$ |
| Atomic mass unit | $m$ | $1.660538921(73) \cdot 10^{-27}\,\mathrm{kg}$ |
| Vacuum permittivity | $\epsilon_0$ | $8.854187817620389 \cdot 10^{-12}\,{}^{F}\!/_{\mathrm{m}}$ |
| Reduced Planck constant | $\hbar$ | $1.054571726(47) \cdot 10^{-34}\,\mathrm{J} \cdot \mathrm{s}$ |
| Speed of light | $c$ | $299792458\,{}^{m}\!/_{\mathrm{s}}$ |

## 9.2 Optimised parameters for 72.17 % and 1.8 % $^{85}$Rb abundance

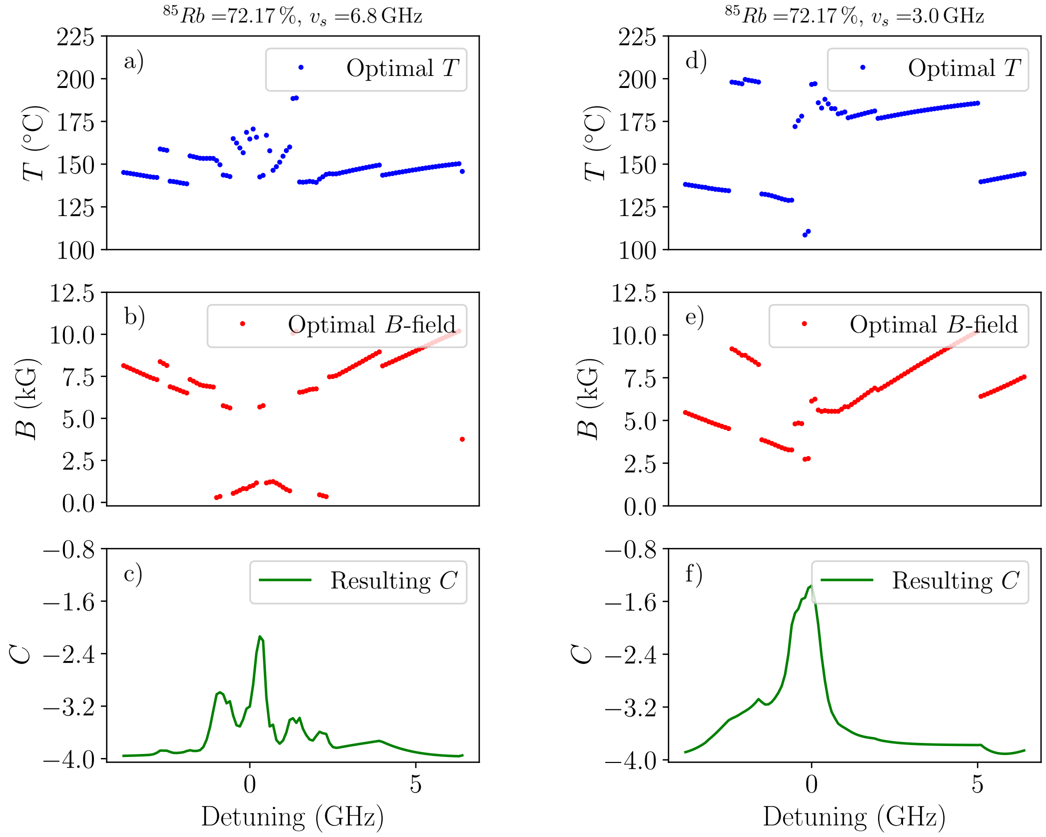

Figure 9.1: Optimized parameters for a 72.17 % $^{85}$Rb cell. a) - c): For $\nu_s$ = 6.8 GHz, d) - e): For $\nu_s$ = 3 GHz over the pump detuning. Each pump detuning is assigned a lowest possible cost value in c) and f) found by the optimisation routine described in section 5.1. a), d) and b), e) display the temperature and $B$-field to the corresponding lowest cost value of each pump detuning, respectively.

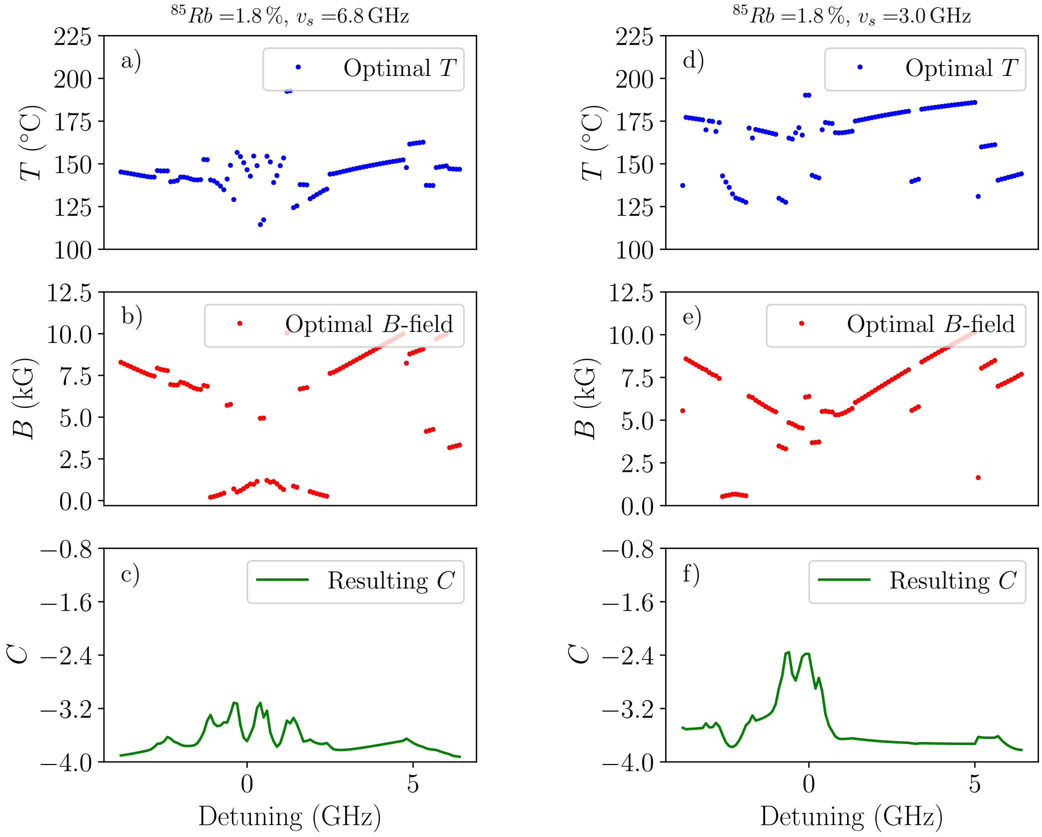

Figure 9.2: Optimized parameters for a 1.8 % $^{85}$Rb cell. a) - c): For $\nu_s = 6.8\,\mathrm{GHz}$, d) - e): For $\nu_s = 3\,\mathrm{GHz}$ over the pump detuning. Each pump detuning is assigned a lowest possible cost value in c) and f) found by the optimisation routine described in section 5.1. a), d) and b), e) display the temperature and $B$-field to the corresponding lowest cost value of each pump detuning, respectively.

Figure 9.1 and 9.2 show the optimised parameters over pump detuning for the 72.17 % abundances 1.8 % and $^{85}$Rb. Those abundances did not show the best performance at the desired pump detuning.

A parameter pair exists which allows the operation of the beam splitter at 0 GHz pump detuning in figure 9.2 c) ($T = 146.5\,°\mathrm{C}, B = 860\,\mathrm{kG}$).

The cost value at those parameters is $C = -3.69$. The possible reason for this relatively low cost value is the larger spectral distance between the channels and the transitions. This allows a non-zero magnetic field while still maintaining a low absorption at the red channel, as shown in figure, 9.3. Due to the low magnetic field the Zeeman splitting is not linear, which leads to a different magnitude of rotation.

The ratio ${}^{\phi(\nu_1)}/_{\phi(\nu_2)} = 1.95$ indicates the relative difference of the rotation magnitude. It therefore can be used as a measure for this effect. A value of 1.95 indicates enough rotation, since the red channel is rotated by $\phi\left(\nu_1\right) \approx {}^{\pi}/_{2}$ and the blue channel by $\phi\left(\nu_2\right) \approx$

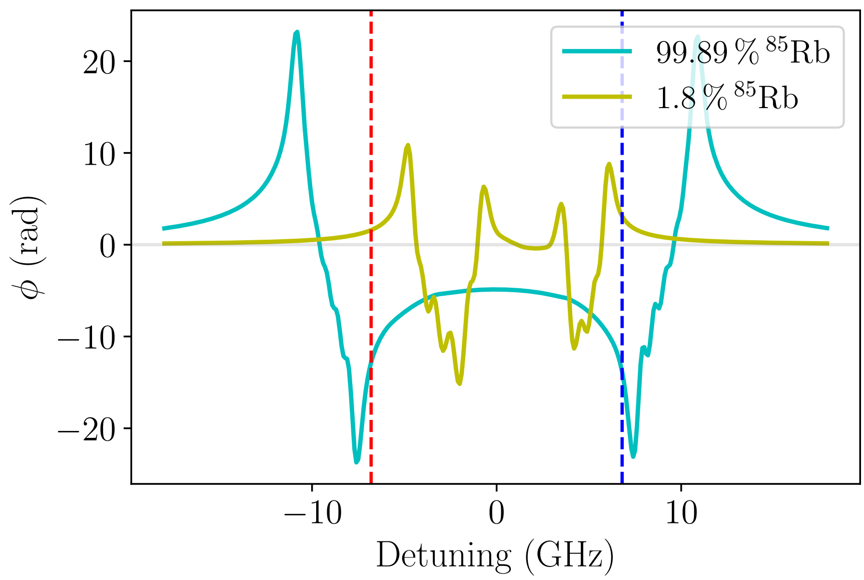

Figure 9.3: Rotation amplitude and direction at the end of the vapour cell for 1.8 % and 99.89 % $^{85}$Rb.

$\pi$. The proximity of the blue channel to the transition causes more absorption than desired.

## 9.3 Magnet design

Equation (9.1) is used to calculate the magnetic field of the top head shaped permanent magnets.

$$
\begin{aligned}
B(z) = {} & \frac{B_0}{2}\left(\frac{z+\frac{L_1}{2}}{\sqrt{\left(z+\frac{L_1}{2}\right)^2+R_1^2}} - \frac{z-\frac{L_1}{2}}{\sqrt{\left(z-\frac{L_1}{2}\right)^2+R_1^2}}\right)\\
& -\frac{B_0}{2}\left(\frac{z+\frac{L_1}{2}}{\sqrt{\left(z+\frac{L_1}{2}\right)^2+r^2}} + \frac{z-\frac{L_1}{2}}{\sqrt{\left(z-\frac{L_1}{2}\right)^2+r^2}}\right)\\
& +\frac{B_0}{2}\left(\frac{z-\frac{L_1}{2}}{\sqrt{\left(z-\frac{L_1}{2}\right)^2+R_2^2}} - \frac{z-\frac{L_1}{2}-L_2}{\sqrt{\left(z-\frac{L_1}{2}-L_2\right)^2+R_2^2}}\right)\\
& -\frac{B_0}{2}\left(\frac{z-\frac{L_1}{2}}{\sqrt{\left(z-\frac{L_1}{2}\right)^2+r^2}} + \frac{z-\frac{L_1}{2}-L_2}{\sqrt{\left(z-\frac{L_1}{2}-L_2\right)^2+r^2}}\right)\\
& +\frac{B_0}{2}\left(\frac{z-\frac{L_1}{2}-L_2-g}{\sqrt{\left(z-\frac{L_1}{2}-L_2-g\right)^2+R_2^2}} - \frac{z-\frac{L_1}{2}-2\cdot L_2-g}{\sqrt{\left(z-\frac{L_1}{2}-L_2-g\right)^2+R_2^2}}\right)\\
& -\frac{B_0}{2}\left(\frac{z-\frac{L_1}{2}-L_2-g}{\sqrt{\left(z-\frac{L_1}{2}-L_2-g\right)^2+r^2}} + \frac{z-\frac{L_1}{2}-2\cdot L_2-g}{\sqrt{\left(z-\frac{L_1}{2}-2\cdot L_2-g\right)^2+r^2}}\right)\\
& +\frac{B_0}{2}\left(\frac{z-\frac{L_1}{2}-2\cdot L_2-g}{\sqrt{\left(z-\frac{L_1}{2}-2\cdot L_2-g\right)^2+R_2^2}} - \frac{z-\frac{3\cdot L_1}{2}-2\cdot L_2-g}{\sqrt{\left(z-\frac{3\cdot L_1}{2}-2\cdot L_2-g\right)^2+R_2^2}}\right)\\
& -\frac{B_0}{2}\left(\frac{z-\frac{L_1}{2}-2\cdot L_2-g}{\sqrt{\left(z-\frac{L_1}{2}-2\cdot L_2-g\right)^2+r^2}} + \frac{z-\frac{3\cdot L_1}{2}-2\cdot L_2-g}{\sqrt{\left(z-\frac{3\cdot L_1}{2}-2\cdot L_2-g\right)^2+r^2}}\right).
\end{aligned}
\tag{9.1}
$$

$B_0$ represents the remanence of the magnets which is assumed to be $B_0 = 14\,\mathrm{kG}$. $L_1$ and $L_2$ represent the length of the two cylindrical segments composing the top head shape of the magnet. $R_1$ and $R_2$ are the outer radii respectively and $r$ is the radius of the bore through the segment. $g$ is the gap between the magnets were the cell is positioned.

### 9.3.1 Cost function: Magnets

Equation (9.2) shows the cost function used to optimize the magnet shape.

$$C_M = \left( \sqrt{\frac{\sum_{i}^{N} \left(B\left(z_i\right) - B_0\right)^2}{N}} - B_{dev} \right)^2 + 10^7 \cdot V_M \tag{9.2}$$

The variable $z_i$ refers to the z coordinates of the $B$-field inside the cell. $N$ refers to the number of $z_i$ values used to define the field. $B_0$ is the magnetic field target and $B_{dev}$ is the desired standard deviation from the target. Usually $B_{dev} = 0$ for the minimal inhomogeneity of the magnetic field in the cell. The volume $V_M = L_1 \cdot R_1^2 \cdot 2\pi + L_2 \cdot R_2^2 \cdot 2\pi$ of the magnets in $\mathrm{m}^3$ has also been made part of the cost function to try and reduce the material needed. Table 9.4 displays the increments used to map the cost function in equation (9.2). The minimization of the magnet cost function has been performed in the same manner as discussed in section 5.1.

Table 9.4: Table of increments used to map the magnet cost function in [mm].

| $z$ increment | $L_i$ increment | $R_i$ increment | $g$ increment | $r$ increment |
|---|---|---|---|---|
| 0.1 | 1.5 | 1.5 | 2.5 | 2 |

### 9.3.2 Finite element method (FEM)

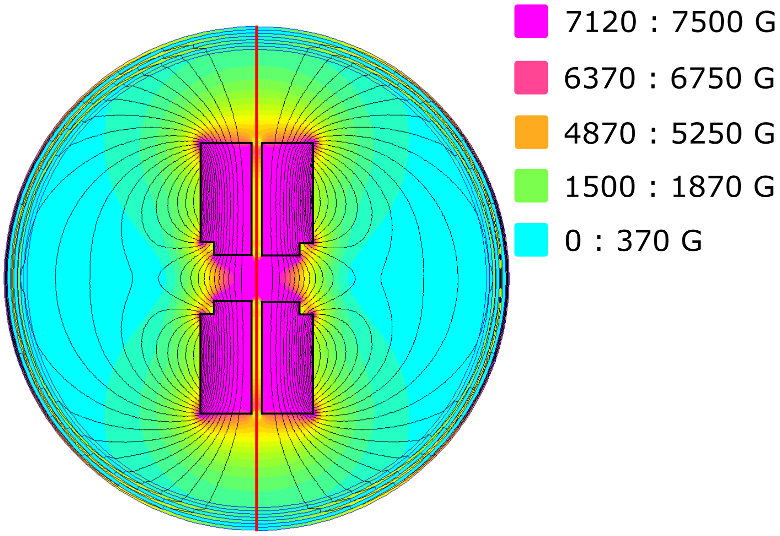

Figure 9.4: Colour plot of the magnetic field generated by the optimized magnet dimensions calculated by *FEMM v4.2*. The red line indicates the path of the probe laser and the axis of rotational symmetry. The Dirichlet boundary conductions were generated by the software to create a better approximation as stated in [67].

The force acting on magnets mentioned in section 6.1 was calculated using the model depicted in figure 9.4. Furthermore the radial and axial profiles were investigated and are depicted in figure 9.5. The axial profile shows good agreement with the magnetic profile calculated with equation (9.1). A tutorial is avalible in [68, 67] guiding the user through the software. The 'Open Boundary Builder' in the software was used to create open boundary conditions for a better fidelity as stated in [67]. The parameters used are listed in table 9.5.

Calculations with *FEMM v4.2* take a lot more material properties into consideration compared to the model represented in equation (9.1). Therefore the produced magnetic field is sensitive to changes in those properties. Source [69] lists the lower boundaries for the N52 grade neodymium magnets. By changing the material property 'coercivity' $\mathrm{H}_C$ of NdFeB 52 MGOe to $\mathrm{H}_C = 860\,\mathrm{kA/m}$ and the remanence to $14\,\mathrm{kG}$ the profile in figure 9.5 a) is calculated. Figure 9.5 b) shows that the magnetic field drops along a radial distance of $1.5\,\mathrm{mm}$ by $\approx 12\,\mathrm{G}$. The relative change in the magnetic field amounts to $\approx 0.16\,\%$. This corresponds to a shift in the spectrum by $\approx 50\,\mathrm{MHz}$. Photon at different positions in the Gauss-profile of the beam will therefore experience a slightly different amount of rotation. To mitigate for this effect a narrower beam waste would be advantageous. Since the transmission spectra in the weak probe regime are not affected in a noticeable manner this effect was neglected.

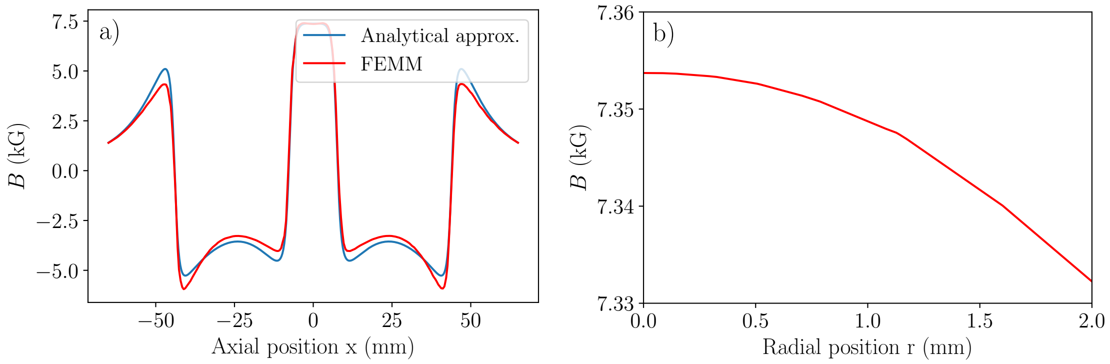

Figure 9.5: a) Axial magnetic field calculated by *FEMM* with the setting in table 9.5 and by the analytical approximation (equation (9.1)). Both approaches show similar profiles and similar magnetic field strengths at the position of the cell. b) Radial magnetic profile calculated by *FEMM*. The magnetic field drops by ≈ 12 G along a radial distance of 1.5 mm.

Table 9.5: Settings for the FEM calculations in *FEMM v4.2*

Problem definition

| Variable | Setting |
|---|---|
| Probe type | Axisymmetric |
| Length units | Millimeters |
| Frequency (Hz) | 0 |
| Solver precision | 1e-008 |
| Min angle | 30 |
| AC solver | Succ. Approx |
| Prev type | None |

Operation

| | |
|---|---|
| Node | ‘Active’ |
| Boundary | |
| BC type | Mixed |
| $c_0$ coeff. | 31329713.20706601 |
| $c_1$ coeff. | 0 |

Materials used

| | |
|---|---|
| Magnets | NdFeB 52 MGOe |
| Surrounding area | Air |

Open Boundary Builder

| | |
|---|---|
| Layers | 7 |
| Radius | 173.31 |
| Horizontal center | 0 |
| Vertical center | 0 |
| Edge type | Dirichlet |

## 9.4 Photo-detectors

The bandwidth of the initially used Thorlabs DET36A photo-detector is limited by the area of the photodiode (13 mm$^2$). This relatively big area leads to higher parasitic capacitance $C_p$, which introduces high-pass-properties into the circuit. To increase the bandwidth a termination resistor of $R_t = 100\,\mathrm{k\Omega}$ is introduced between the detector output and the oscilloscope input, as stated in [54]. The draw back of this method is a reduced amplification of the signal. Therefore a photodiode with a smaller area is advantageous.

The author chose to design a suited photo-detector himself, since this approach allows more freedom-of-choice in the amplification of the product. The home-build photo-detectors were designed with the help of [70] and the free software *fritzing* [71]. The photodiode used is the SFH 2400-Z with an active area of 1 mm$^2$ [72]. The operation-amplifier (OP-AMP) of choice is the AD8033 [73]. Figure 9.6 shows the simplified circuit-diagram used.

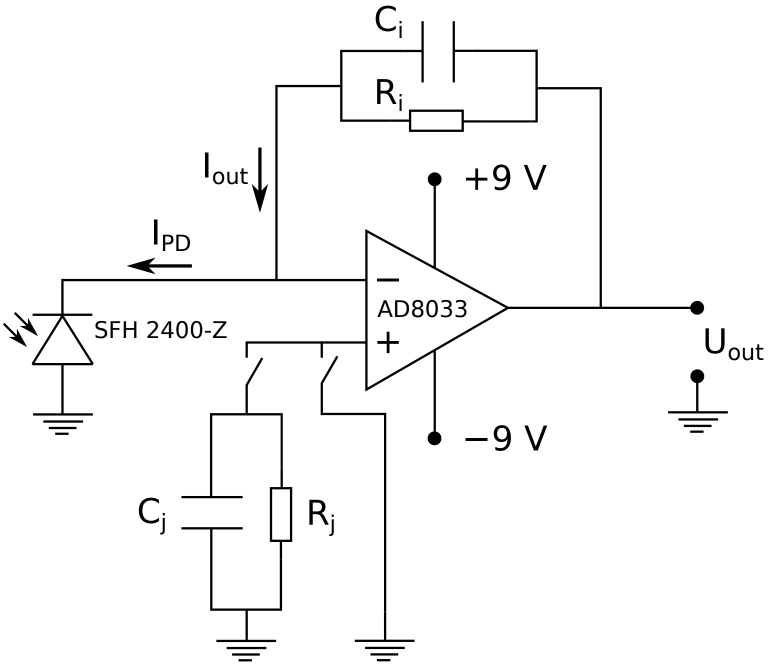

Figure 9.6: Transimpedance amplifier circuit with a SFH 2400-Z photodiode as input. Light shining onto the photodiode produces a current at the inverting input. As a result the output of the OP-AMP produces a potential $U_{out}$ to counteract the current introduced by the photodiode. Therefore $U_{out} = -R_i \cdot I_{PD}$ and $I_{PD} + I_{out} = 0$. $R_j$ has the same value as $R_i$. It reduces the offset of the output signal produced by $I_{PD}$. $C_j$ is the noise-shunt capacitor for $R_j$. The latter can be bypassed by a switch.

The capacitor $C_i$ and feedback-resistor R$_i$ define the amplification. $C_i$ in particular suppresses the gain-overshoot produced by the L-C tank formed by $C_p$ [70]. The following neglects the parasitic capacitance $C_p$ of the photodiode and describes the foundation of the transimpedance-amplifier. In case of a static signal and an ideal OP-AMP the amplification $\beta$ is given by:

$$\beta\,(f=0) = \frac{U_{out}}{I_{PD}} = -R_i. \tag{9.3}$$

For a time dependent signal the high-pass properties of $C_i$ begin to emerge. The factor changes to

$$\beta\,(f) = \frac{-R_i}{\left(1 + i \cdot {}^{f}\!/\!{}_{f_g}\right)}, \tag{9.4}$$

were

$$f_g = \frac{1}{2\pi R_i C_i}. \tag{9.5}$$

$f_g$ describes the $-3\,\mathrm{dB}$ cut-off-frequency of an ideal operation amplifier (amplification $\beta_{OP} = \infty$ and transit frequency $f_T = \infty$). The output signal then takes the shape

$$U_{out}\,(f) = \frac{-I_{PD} \cdot R_i}{\left(1 + i{}^{f}\!/\!{}_{f_g}\right)}. \tag{9.6}$$

Equations (9.3) to (9.5) show how a large feedback-resistor increases the amplification $\beta$ while also limiting the cut-off-frequency $f_g$. To conserve $f_g$, $C_i$ has to become very small. For example 1.59 fF if $f_g = 10\,\mathrm{MHz}$ and $R_i = 10\,\mathrm{M\Omega}$, therefore no $C_i$ was needed. The resistor $R_j$ at the non-inverting input of the OP-AMP reduces the offset of $U_{out}$ and $C_j$ shunts the noise of the resistor. In this thesis the value of $R_i$ and $R_j$ are fixed to $R_j = R_i = 10\,\mathrm{M\Omega}$.

## 9.5 Technical drawings

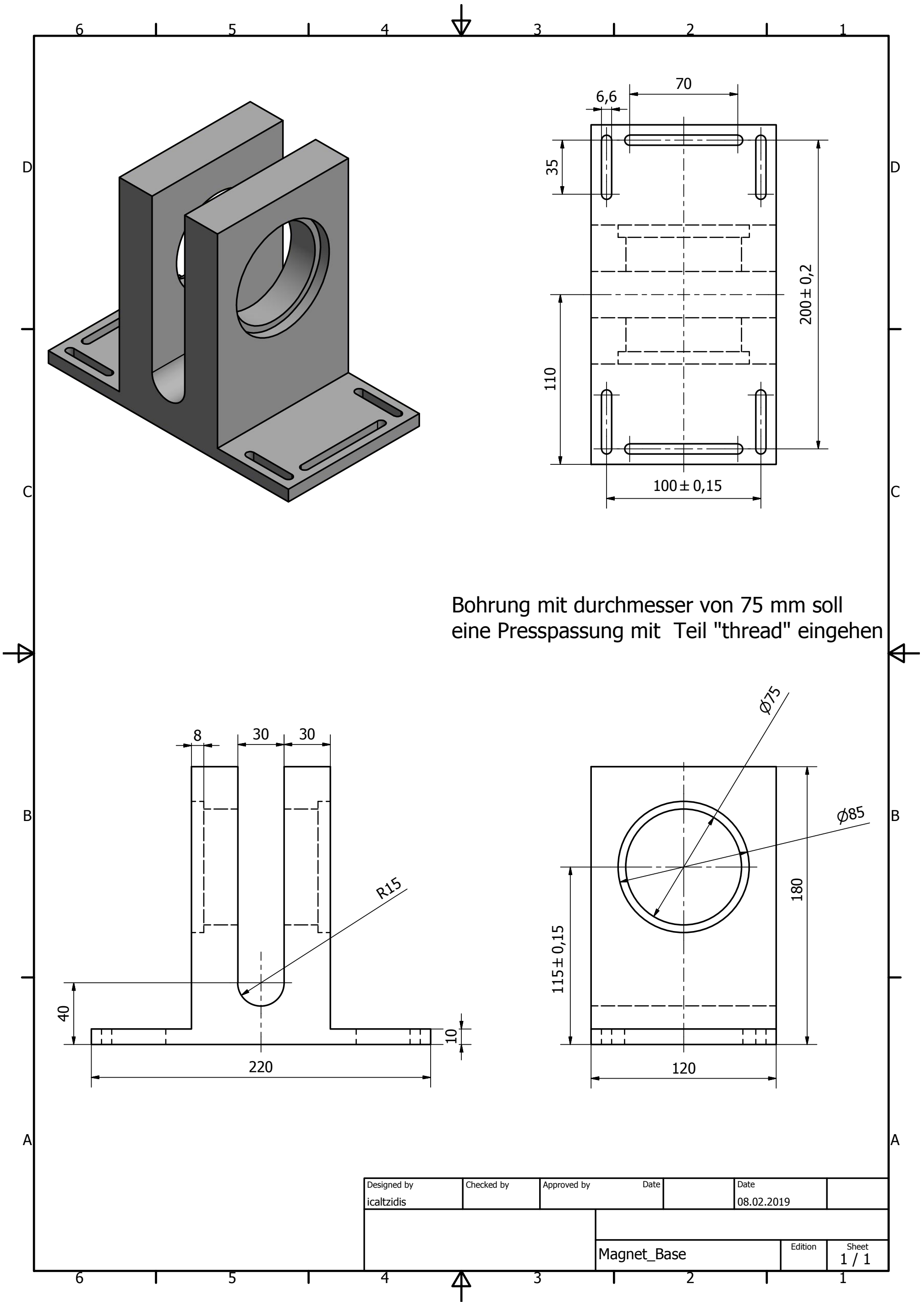

Bohrung mit durchmesser von 75 mm soll
eine Presspassung mit  Teil "thread" eingehen

| Designed by | Checked by | Approved by | Date | Date |
|---|---|---|---|---|
| icaltzidis | | | | 08.02.2019 |

| | Edition | Sheet |
|---|---|---|
| Magnet_Base | | 1 / 1 |

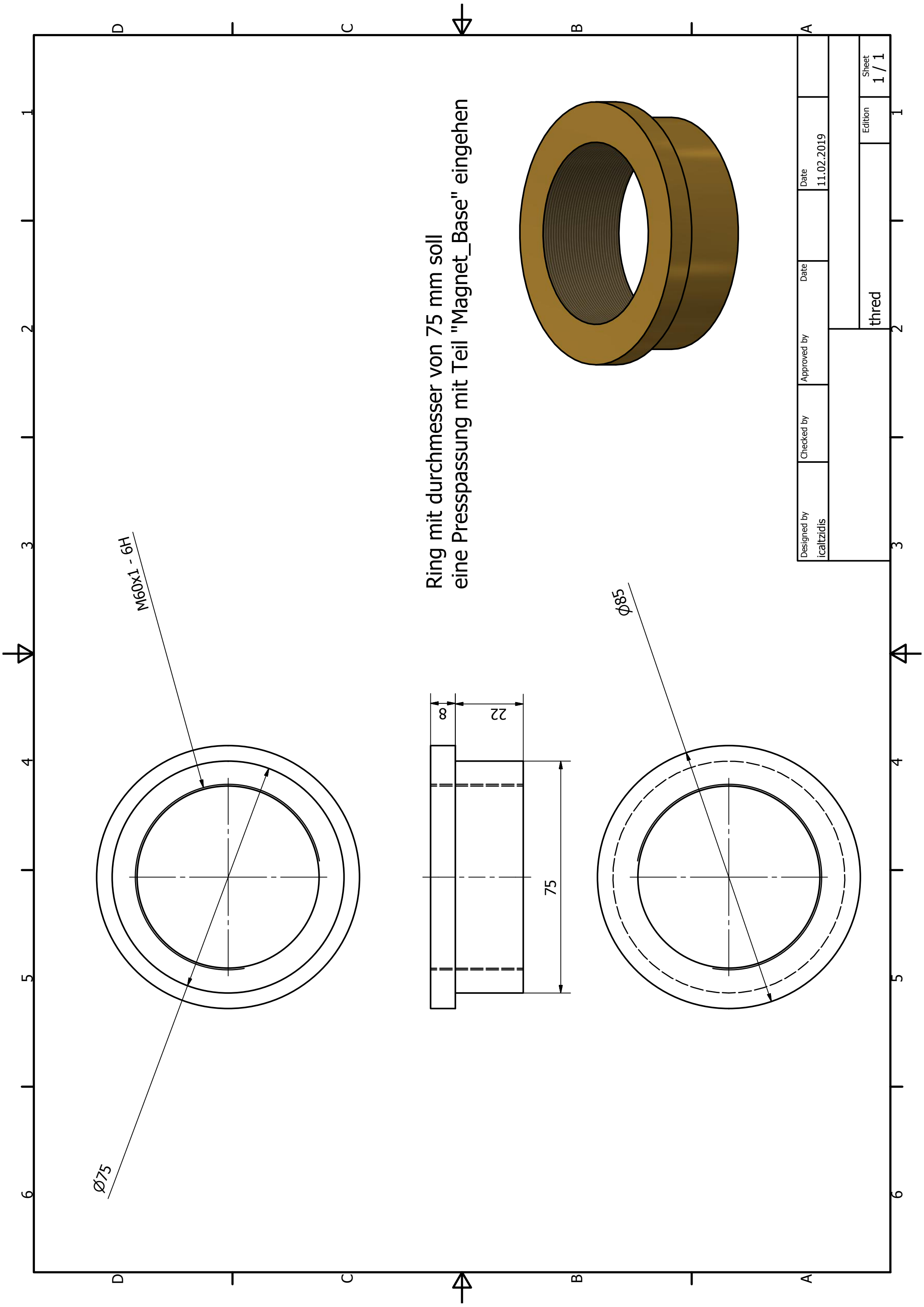

Ring mit durchmesser von 75 mm soll
eine Presspassung mit Teil "Magnet_Base" eingehen

Designed by: icaltzidis
Checked by:
Approved by:
Date:
Date: 11.02.2019
thred
Edition:
Sheet: 1 / 1

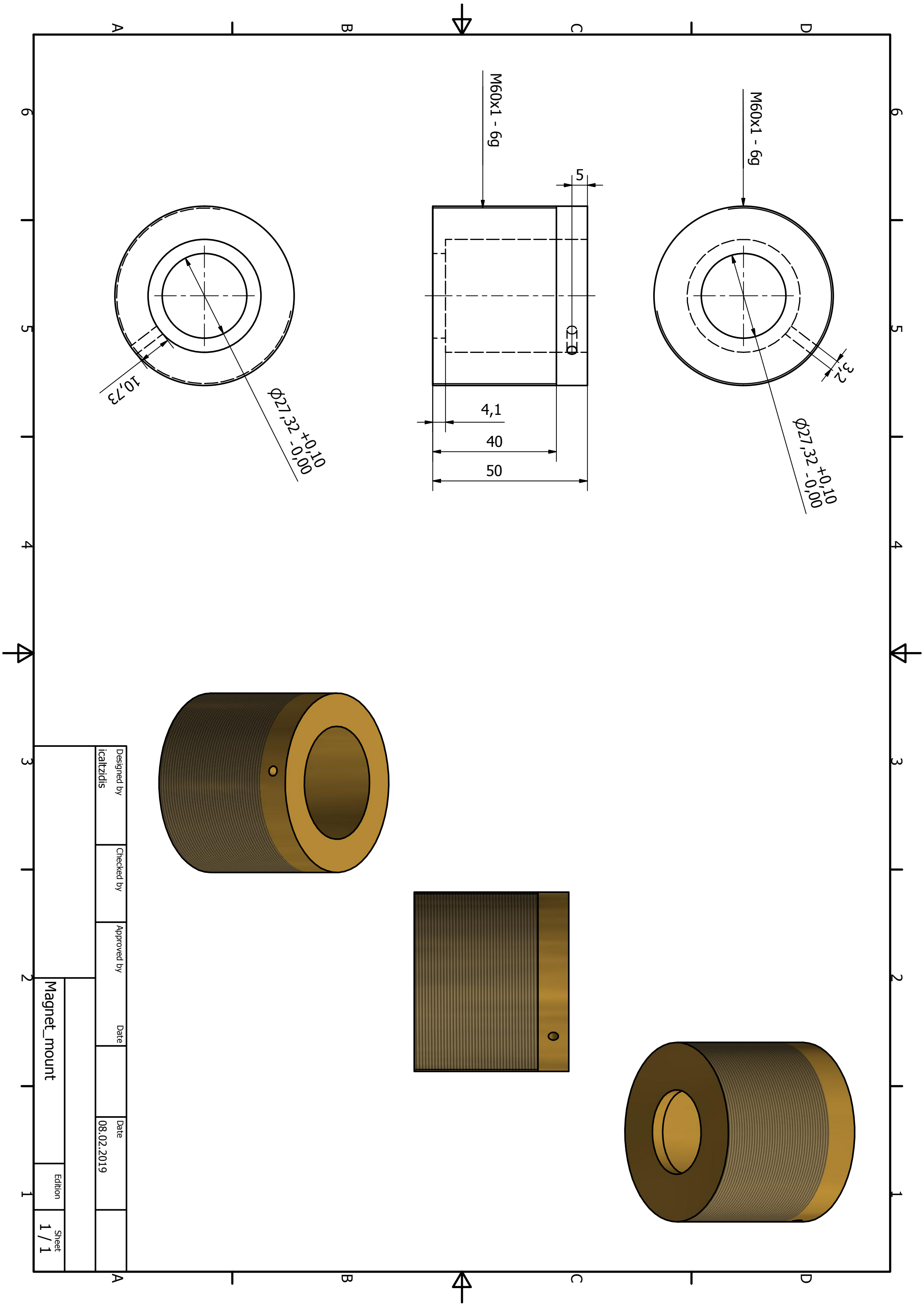
A
B
C
D
1
2
3
4
5
6
M60x1 - 6g
M60x1 - 6g
5
10,73
Ø27,32 +0,10 -0,00
Ø27,32 +0,10 -0,00
3,2
4,1
40
50
Designed by
icaltzidis
Checked by
Approved by
Date
Date
08.02.2019
Magnet_mount
Edition
Sheet
1 / 1

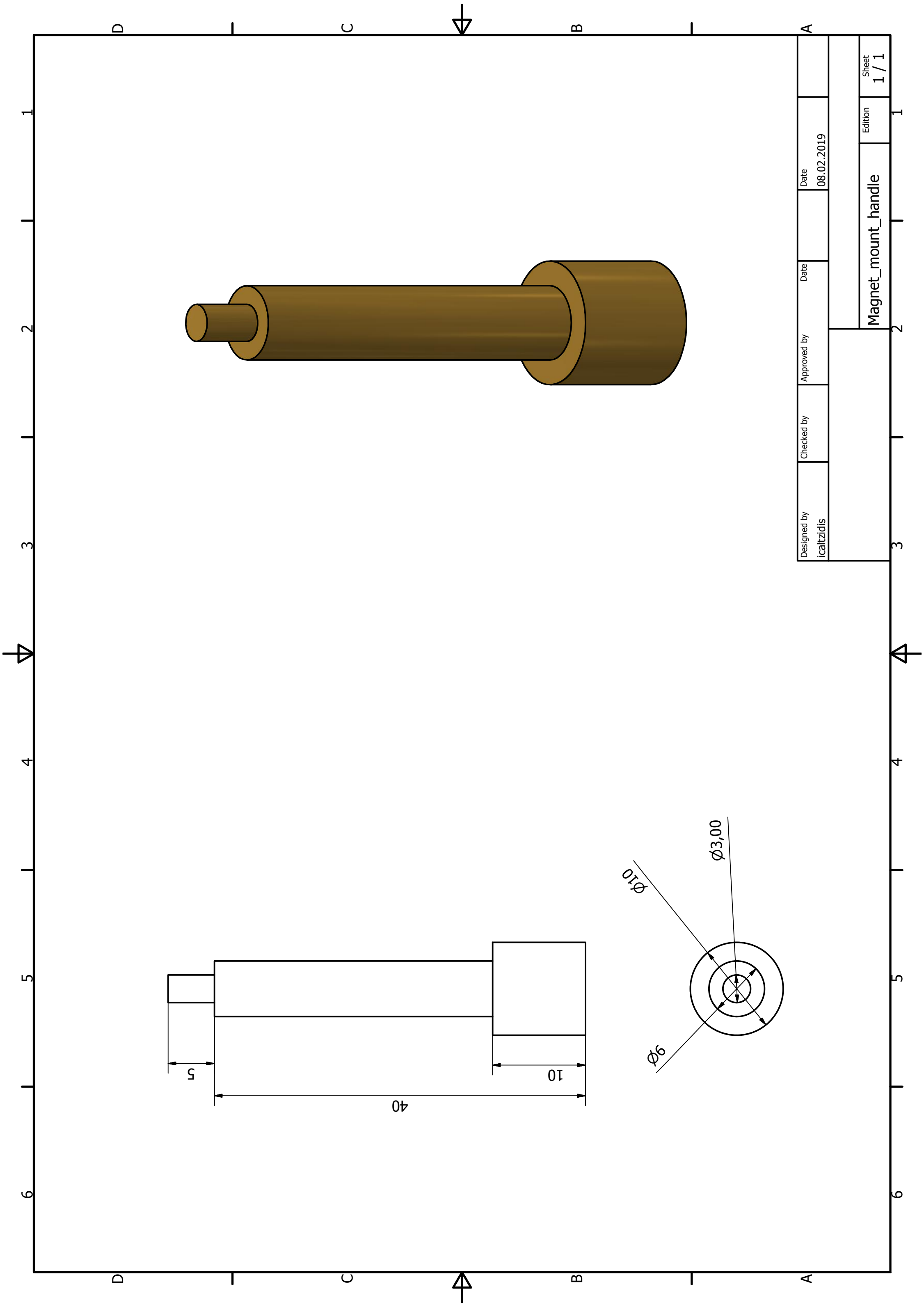
Designed by
icaltzidis
Checked by
Approved by
Date
Date
08.02.2019
Magnet_mount_handle
Edition
1
Sheet
1 / 1
5
40
10
Ø10
Ø6
Ø3,00

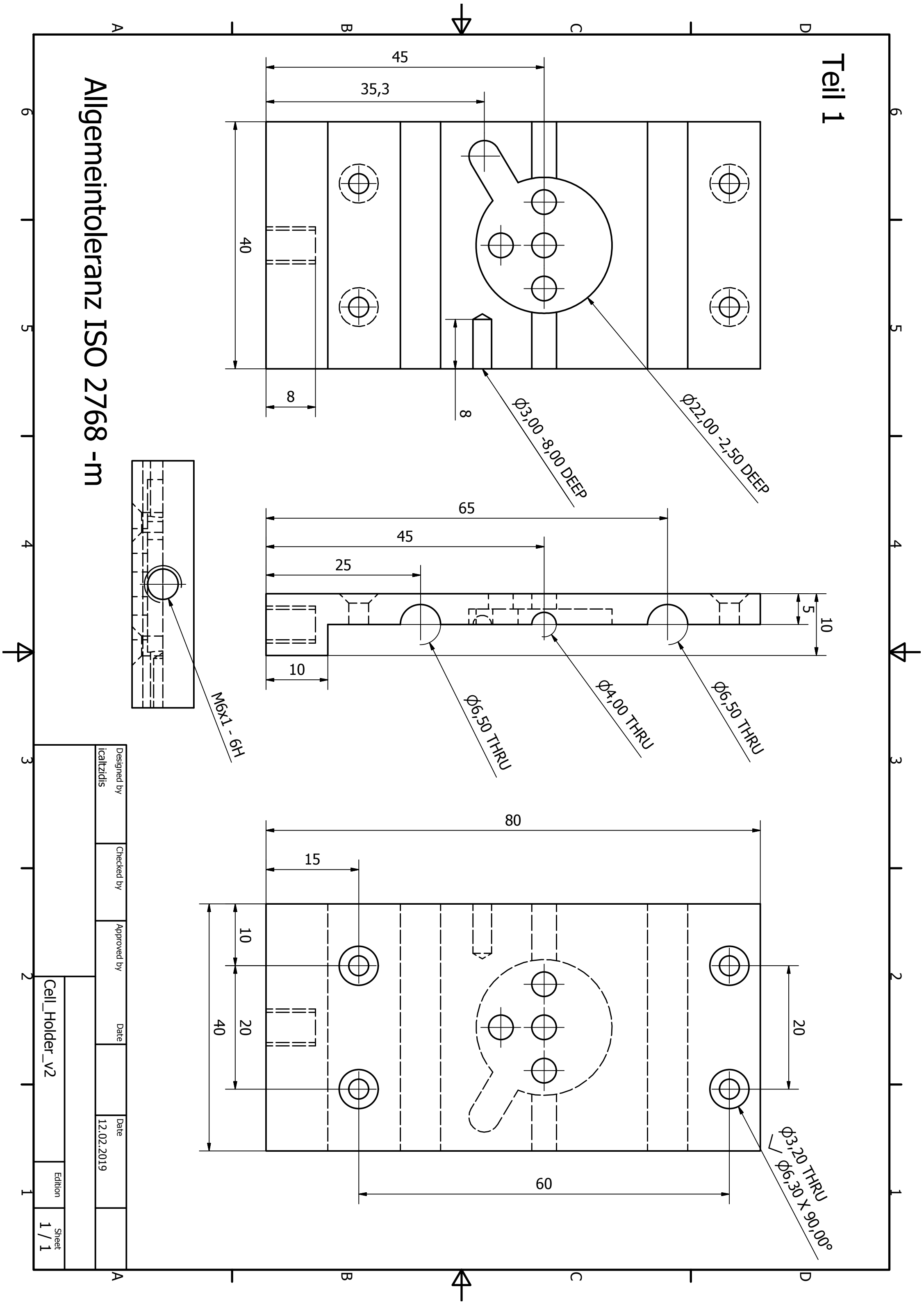
Teil 1
Allgemeintoleranz ISO 2768 -m
45
35,3
40
8
8
Ø3,00 -8,00 DEEP
Ø22,00 -2,50 DEEP
65
45
25
5
10
10
Ø6,50 THRU
Ø4,00 THRU
Ø6,50 THRU
M6x1 - 6H
80
15
10
20
40
20
60
Ø3,20 THRU
⌵ Ø6,30 X 90,00°
Designed by
icaltzidis
Checked by
Approved by
Date
Date
12.02.2019
Cell_Holder_v2
Edition
Sheet
1 / 1
A
B
C
D
1
2
3
4
5
6

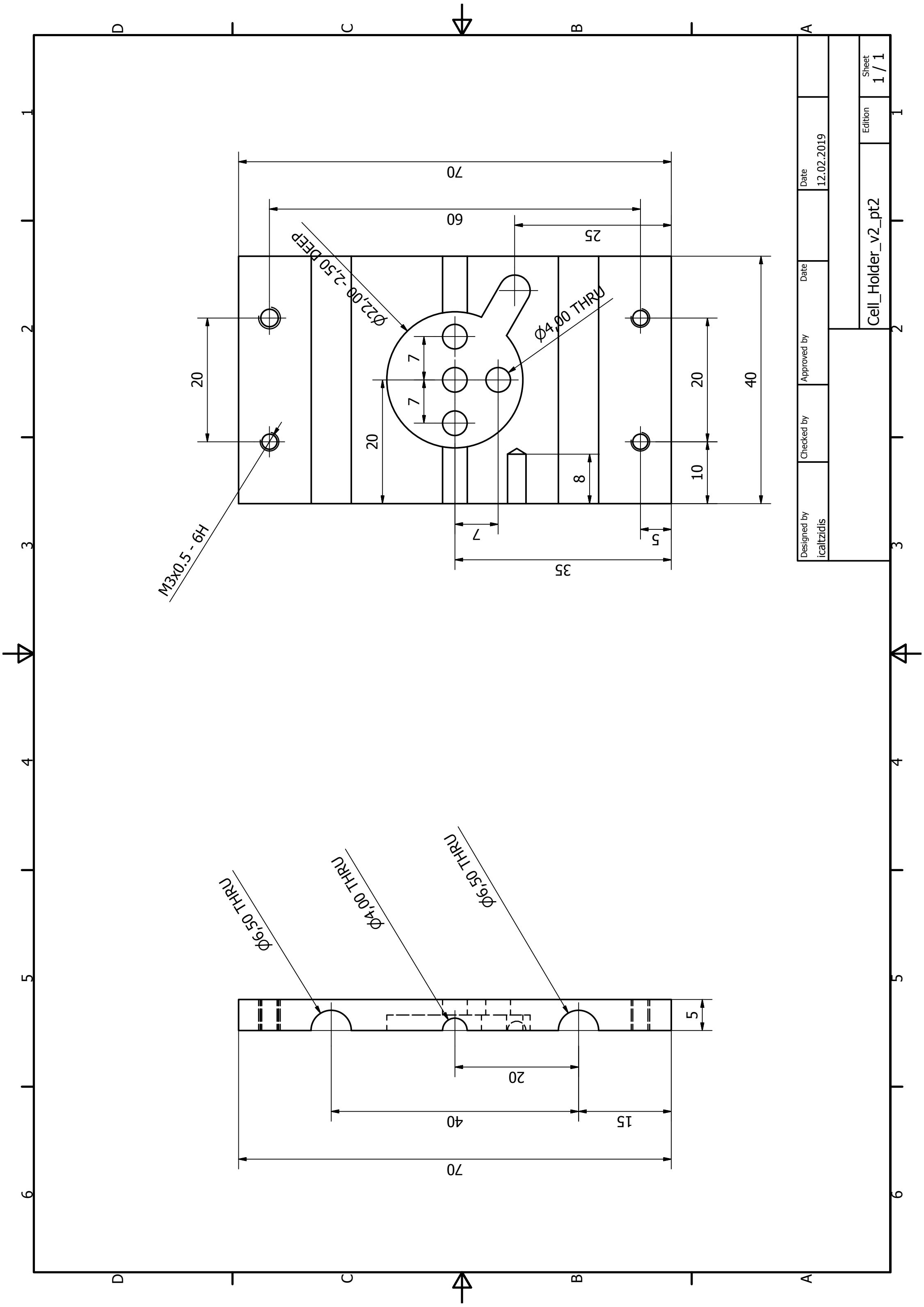

Designed by
icaltzidis
Checked by
Approved by
Date
Date
12.02.2019
Cell_Holder_v2_pt2
Edition
Sheet
1 / 1
70
60
25
Ø22,00 -2,50 DEEP
Ø4,00 THRU
M3x0.5 - 6H
20
20
40
7
7
20
8
10
7
5
35
Ø6,50 THRU
Ø4,00 THRU
Ø6,50 THRU
5
20
40
15
70
A
B
C
D
1
2
3
4
5
6

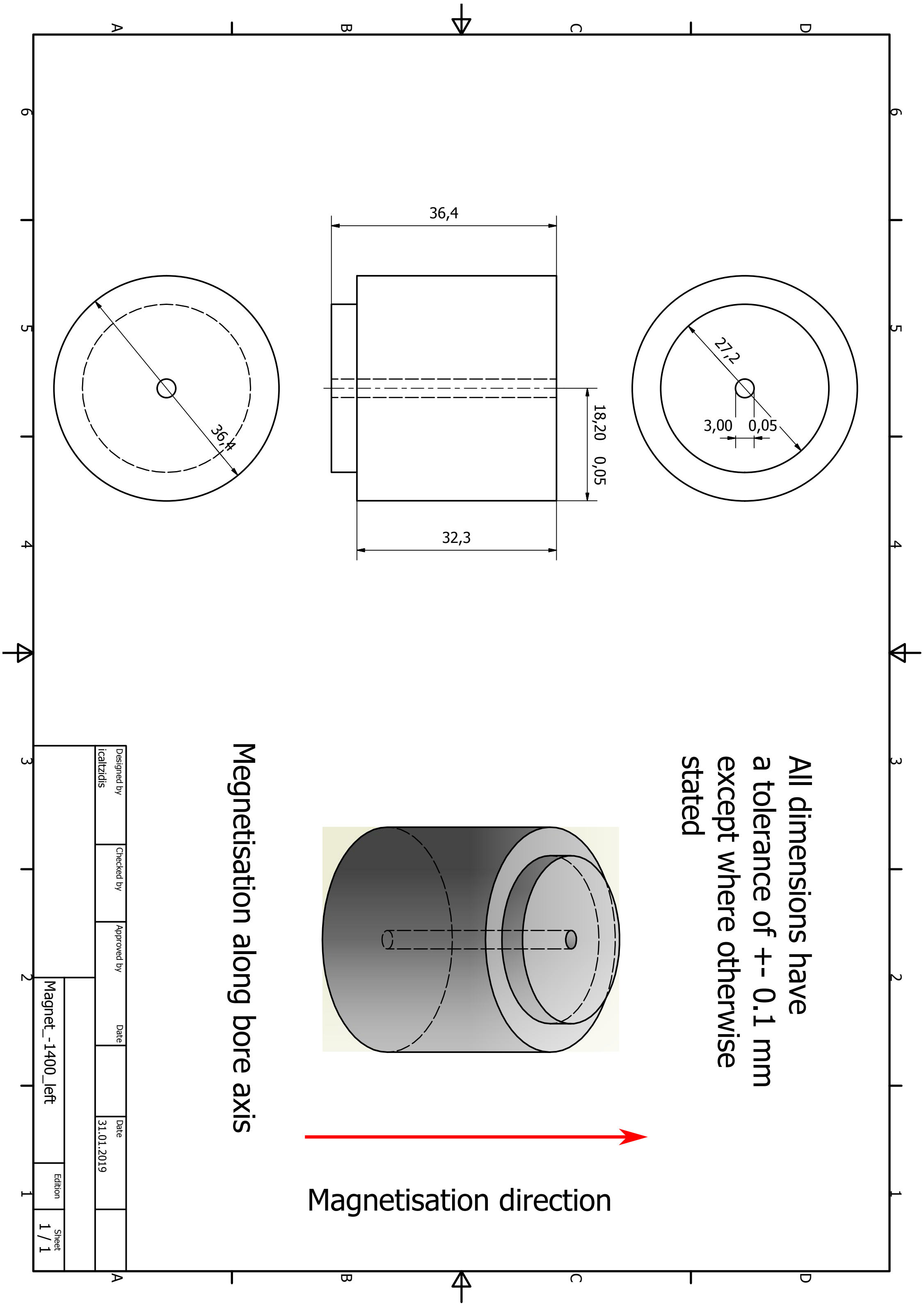

All dimensions have a tolerance of +- 0.1 mm except where otherwise stated

Magnetisation along bore axis

Magnetisation direction

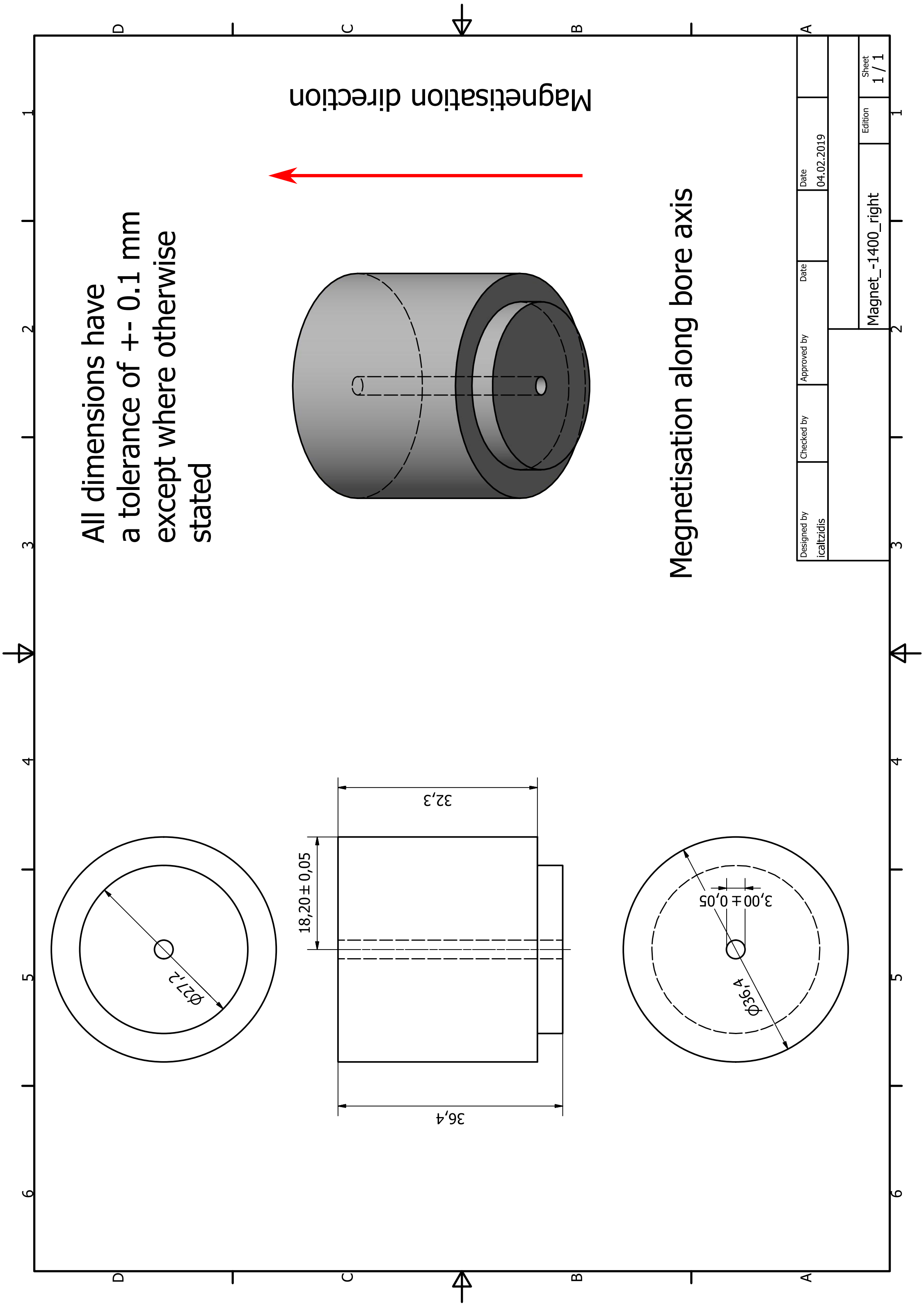
All dimensions have
a tolerance of +- 0.1 mm
except where otherwise
stated
Magnetisation direction
Megnetisation along bore axis
32,3
36,4
18,20 ± 0,05
3,00 ± 0,05
Φ27,2
Φ36,4
Designed by
icaltzidis
Checked by
Approved by
Date
Date
04.02.2019
Magnet_-1400_right
Edition
1
Sheet
1 / 1

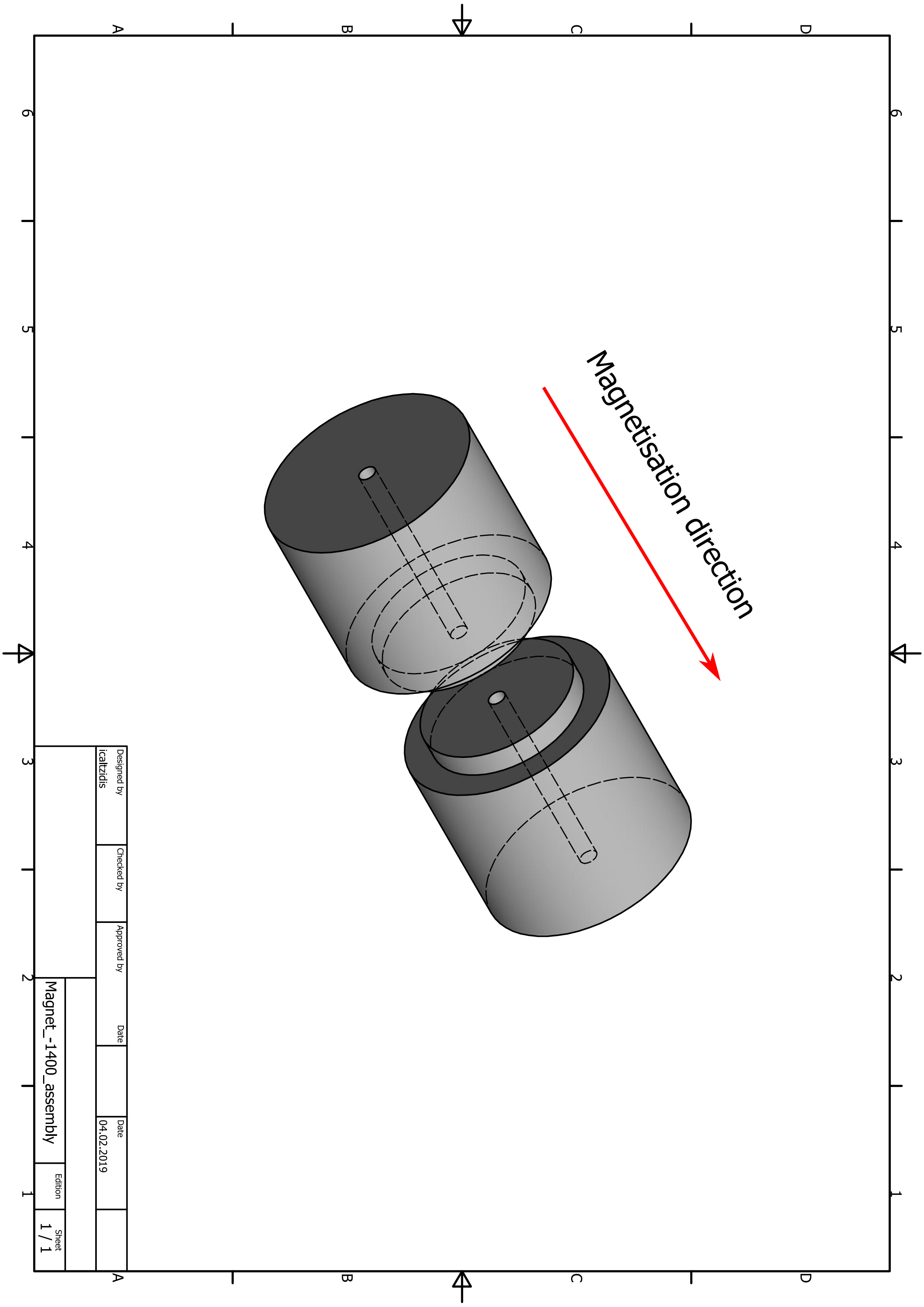
Magnetisation direction
Designed by
icaltzidis
Checked by
Approved by
Date
Date
04.02.2019
Magnet_-1400_assembly
Edition
Sheet
1 / 1

# Acknowledgements

After this long journey called studying physics I would like to thank my colleagues and friends for their continuous support.

First of all, I would like to thank Prof. Tilman Pfau for the opportunity to do my master's thesis here at the 5th Physics Institute.

To Dr. Harald Kübler who always found some time in his busy everyday life to help me when I was looking for things again.

Furthermore I would like to thank Dr. Mark Zentile, who always had an open ear for all my personal and professional questions and somehow managed to loosen up the hard working day with his British humour.

Also the colleagues Florian Christaller and Alexander Currle for energetic support with various small things.

Furthermore I would like to thank Patrik Zielinski and Michael Scharwächter, who were always available for a short break.

A special thank you to my family, Charalambos Caltzidis, Dimitra Caltzidou, Kiriaki Kaltzidou and Karlo Lorusso, Ioannis Caltzidis (senior) and Evangelia Caltzidou who always supported me.

Finally I would like to thank Julia Kingsbury and her family, Marco Kingsbury, Karin Kingsbury, Carolina Kingsbury and Luzius Paprotta, who always had room for one more at the table.

# Bibliography

[1] Simone Luca Portalupi et al. "Simultaneous Faraday filtering of the Mollow triplet sidebands with the Cs-D 1 clock transition". In: *nature communications* 13632.7 (2016).

[2] A. Ulhaq et al. "Cascaded single-photon emission from the Mollow triplet sidebands of a quantum dot". In: *Nature Photonics* 6.4 (2012), pp. 238–242.

[3] Mark A. Zentile et al. "Atomic Faraday filter with equivalent noise bandwidth less than 1 GHz". In: *Optics Letters* 40.9 (2015), p. 2000.

[4] Brian Julsgaard, Alexander Kozhekin, and Eugene S. Polzik. "Experimental long-lived entanglement of two macroscopic objects". In: *Nature* 413.6854 (2001), pp. 400–403.

[5] Anna L. Marchant et al. "Off-resonance laser frequency stabilization using the Faraday effect". In: *Optics Letters* 36.1 (2011), p. 64.

[6] Mark A. Zentile et al. "The hyperfine Paschen-Back Faraday effect". In: *Journal of Physics B: Atomic, Molecular and Optical Physics* 47.7 (2014).

[7] O. Alibart et al. "High-performance guided-wave asynchronous heralded single-photon source". In: *Optics Letters* 30.12 (2005), p. 1539.

[8] Sylvain Fasel et al. "High-quality asynchronous heralded single-photon source at telecom wavelength". In: *New Journal of Physics* 6 (2004), pp. 1–11.

[9] P. Michler et al. "A quantum dot single-photon turnstile device". In: *Science* 290.5500 (2000), pp. 2282–2285.

[10] Christian Kurtsiefer et al. "Stable solid-state source of single photons". In: *Physical Review Letters* 85.2 (2000), pp. 290–293.

[11] A. Macrae et al. "Tomography of a high-purity narrowband photon from a transient atomic collective excitation". In: *Physical Review Letters* 109.3 (2012), pp. 1–4.

[12] S O Konorov, A B Fedotov, and A M Zheltikov. "Enhanced four-wave mixing in a hollow-core photonic-crystal fiber". In: *Optics Letters* 28.16 (2003), pp. 1448–1450.

[13] Pablo Londero et al. "Ultralow-Power Four-Wave Mixing with Rb in a Hollow-Core Photonic Band-Gap Fiber". In: *Physical Review Letters* 103 (2009), p. 043602.

[14] R. T. Willis et al. "Photon statistics and polarization correlations at telecommunications wavelengths from a warm atomic ensemble". In: *Optics Express* 19.15 (2011), p. 14632.

[15] Jones Eric et al. *Python, SciPy: Open source scientific tools for.* 2001. URL: `http://www.scipy.org/`.

[16] M. A. Zentile et al. “ElecSus: A program to calculate the electric susceptibility of an atomic ensemble”. In: *Computer Physics Communications* 189 (2015), pp. 162–174.

[17] James Keaveney, Charles S. Adams, and Ifan G. Hughes. “ElecSus: Extension to arbitrary geometry magneto-optics”. In: *Computer Physics Communications* 224 (2018), pp. 311–324.

[18] Mark A. Zentile. “Applications of the Faraday Effect in Hot Atomic Vapours”. PhD thesis. Durham University, 2015.

[19] Lee Weller. “Absolute Absorption and Dispersion in a Thermal Rb Vapour at High Densities and High Magnetic Fields”. PhD thesis. Durham University, 2013.

[20] John David Jackson. *Classical Electrodynamics.* 3rd. John Wiley and sons, Inc., 2012.

[21] Syed Abdullah Bin Syed Abdul Rahman Aljunid. “Interaction of a strongly focused light beam with single atoms”. PhD thesis. National University of Singapour, 2012.

[22] Wolfgang Demtröder. *Experimentalphysik 2.* 7th. Springer-Verlag GmbH Deutschland, 2017.

[23] C J Foot. *Atomic Physics Department of Physics.* Oxford University Press, 2005.

[24] Claude Cohen-Tannoudji, Jacques Dupont-Roc, and Gilbert Grynberg. *Atom-Photon Interactions: Basic Processes and Applications.* Wiley-VCH, 1998. ISBN: 0-471-29336-9. URL: `http://adsabs.harvard.edu/abs/1998aibp.book.....C`.

[25] Margaret L Harris. “Realisation of a Cold Mixture of Rubidium and Caesium”. PhD thesis. Durham University, 2008.

[26] Ben E. Sherlock and Ifan G. Hughes. “How weak is a weak probe in laser spectroscopy?” In: *American Journal of Physics* 77.2 (2009), pp. 111–115.

[27] Robert W. Boyd. *Nonlinear Optics.* 2nd. Elsevier Science, 2003.

[28] Rodney Loudon. *The Quantum Theory of Light.* 3rd ed. Oxford University Press, 2003.

[29] Seo Ro Shin and Heung Ryoul Noh. “Calculation and measurement of absolute transmission in rubidium”. In: *Journal of the Physical Society of Japan* 78.8 (2009), pp. 1–4.

[30] Taek Jeong, Jun Yeon Won, and Heung Ryoul Noh. “Line shapes in polarization spectroscopy for the rubidium D1 line in an external magnetic field”. In: *Optics Communications* 292 (2013), pp. 106–110.

[31] David A. Smith and Ifan G. Hughes. “The role of hyperfine pumping in multilevel systems exhibiting saturated absorption”. In: *American Journal of Physics* 72.5 (2004), pp. 631–637.

[32] David R. Lide and Henry V. Kehiaian. *CRC Handbook of Chemistry and Physics.* 85th ed. CRC Press, 2005, pp. 4–80.

[33] Stephen J. Blundell and Katherine M. Blundell. *Concepts in Thermal Physics*. 2nd ed. Oxford University Press, 2010.

[34] Thomas M. Stace et al. “Power-dependent line-shape corrections for quantitative spectroscopy”. In: *Physical Review A - Atomic, Molecular, and Optical Physics* 86.1 (2012), pp. 1–5.

[35] P N Schatz. “The Faraday effect”. In: *Royal Society of Chemistry* 4 (1969), pp. 1–17.

[36] W. Farr and E. W. Otten. “A Rb-magnetometer for a wide range and high sensitivity”. In: *Applied Physics* 3.5 (1974), pp. 367–378.

[37] C. W. White et al. “Determination of g-factor ratios for free Cs133 and Rb87 atoms”. In: *Physical Review A* 7.3 (1973), pp. 1178–1182.

[38] G. Breit and I. I. Rabi. “Measurement of nuclear spin”. In: *Physical Review* 38.11 (1931), pp. 2082–2083.

[39] G.G. Stokes. “On the Composition and Resolution of Streams of Polarized Light from different Sources”. In: *Transactions of the Cambridge Philosophical Society* 9 (1851), p. 399.

[40] Beth Schaefer, Beth Collett, Edward Smyth, Robert Barrett, Daniel Fraher. “Measuring the stokes polarization parameters”. In: *IFMBE Proceedings* 63.2007 (2018), pp. 593–596.

[41] Lee Weller et al. “Measuring the Stokes parameters for light transmitted by a high-density rubidium vapour in large magnetic fields”. In: *Journal of Physics B: Atomic, Molecular and Optical Physics* 45.5 (2012).

[42] P. D. Atherton, N. K. Reay, and J. Ring. “Tunable Fabry-Perot filters”. In: *OPTICAL ENGINEERING* 20.December 1981 (1981), pp. 806–814.

[43] P. Juncar et al. “Absolute determination of the wavelengths of the sodium D1 and D2 lines by using a CW tunable dye laser stabilized on iodine”. In: *Metrologia* 17.3 (1981), pp. 77–79.

[44] R. Wynands et al. “A compact tunable 60-dB Faraday optical isolator for the near infrared”. In: *American Institute of Physics* 63.12 (1992), pp. 5586–5590.

[45] K. Benson et al. “Ultranarrow line filtering using a Cs Faraday filter at 852 nm”. In: *Optics Letters* 16.11 (2008), p. 846.

[46] L. Weller et al. “An optical isolator using an atomic vapor in the hyperfine Paschen-Back regime”. In: 37.16 (2012), pp. 3405–3407.

[47] H. Chen et al. “Sodium-vapor dispersive Faraday filter”. In: *Optics Letters* 18.12 (2008), p. 1019.

[48] Joanna A. Zielińska et al. “Ultra-Narrow Faraday Rotation Filter at the Rb D1 Line”. In: 37.4 (2011), pp. 524–526.

[49] Andreas Rudolf and Thomas Walther. "High-transmission excited-state Faraday anomalous dispersion optical filter edge filter based on a Halbach cylinder magnetic-field configuration". In: *Optics Letters* 37.21 (2012), p. 4477.

[50] Richard P Abel et al. "Faraday dichroic beam splitter for Raman light using an isotopically pure alkali-metal-vapor cell." In: *Optics letters* 34.20 (2009), pp. 3071–3073.

[51] K. J. Reed, D. J., Simbalic, N., Whiting, D. J., Kondo, J. M., Adams, C. S., Weatherill. "Low-drift Zeeman shifted atomic frequency reference". In: *OSA Continuum 1* 1.1 (2018), pp. 4–12.

[52] Fuchang Gao and Lixing Han. "Implementing the Nelder-Mead simplex algorithm with adaptive parameters". In: *Computational Optimization and Applications* 51.1 (2012), pp. 259–277.

[53] Ilja Gerhardt. "How anomalous is my Faraday filter?" In: *Optics Letters* 43.21 (2018), p. 5295.

[54] Thorlabs. *Broadband Polarizing Beamsplitter Cubes*. URL: `https://www.thorlabs.com/newgrouppage9.cfm?objectgroup_id=739` (visited on 10/21/2019).

[55] Bunting Ltd Magnetics Europe Company. *Temperature Ratings, Temperature Effects on Neodymium Iron Boron, NdFeB, magnets*. URL: `https://e-magnetsuk.com/neodymium_magnets/temperature_ratings.aspx` (visited on 06/18/2019).

[56] Lee Weller et al. "Absolute absorption and dispersion of a rubidium vapour in the hyperfine Paschen-Back regime". In: *Journal of Physics B: Atomic, Molecular and Optical Physics* 45.21 (2012).

[57] Armen Sargsyan et al. "Hyperfine Paschen–Back regime realized in Rb nanocell". In: *Optics Letters* 37.8 (2012), p. 1379.

[58] Renju S. Mathew et al. "Simultaneous two-photon resonant optical laser locking (STROLLing) in the hyperfine Paschen–Back regime". In: *Optics Letters* 43.17 (2018), p. 4204.

[59] D. C. Meeker. *Finite Element Method Magnetics (FEMM v4.2)*. 2018. URL: `http://www.femm.info`.

[60] Manfred Merkel and Karl-Heinz Thomas. *Taschenbuch der Werkstoffe*. 7th ed. München; Wien: Fachbuchverl. Leipzig im Carl-Hanser-Verl., 2008, pp. 294–295.

[61] Michael P. Bradley et al. "Penning trap measurements of the masses of 133Cs, 87,85Rb, and 23Na with uncertainties 0.2 ppb". In: *Physical Review Letters* 83.22 (1999), pp. 4510–4513.

[62] E. Arimondo, M. Inguscio, and P. Violino. "Experimental determinations of the hyperfine structure in the alkali atoms". In: *Reviews of Modern Physics* 49.1 (1977), pp. 31–75.

[63] A. Banerjee, D. Das, and V. Natarajan. "Absolute frequency measurements of the D1lines in 39K, 85Rb, and 87Rb with 0.1 ppb uncertainty". In: *Europhysics Letters* 65.2 (2004), pp. 172–178.

[64] S. Bize et al. “High-accuracy measurement of the 87Rb ground-state hyperfine splitting in an atomic fountain”. In: *Europhysics Letters* 45.5 (1999), pp. 558–564.

[65] Jun Ye et al. “Hyperfine structure and absolute frequency of the 87Rb 5P3/2 state”. In: *Optics Letters* 21.16 (1996), p. 1280.

[66] U Volz and H Schmoranzer. “Precision lifetime measurements on alkali atoms and on helium by beam–gas–laser spectroscopy”. In: *Physica Scripta* T65 (1996), pp. 48–56.

[67] D. C. Meeker. *Finite Element Method Magnetics : PermanentMagnetExample.* 2014. URL: `http://www.femm.info/wiki/PermanentMagnetExample` (visited on 09/30/2019).

[68] D. C. Meeker. *FEMM 4.2 Magnetostatic Tutorial.* Tech. rep. 2006.

[69] Bunting Ltd Magnetics Europe Company. *Grades of Neodymium.* URL: `https://e-magnetsuk.com/neodymium_magnets/neodymium_grades.aspx` (visited on 10/21/2019).

[70] Jerald Graeme. *Photodiode Amplifiers OP AMP Solutions.* McGraw-Hill.

[71] Friends-of-Fritzing Foundation. *Fritzing v0.9.3.* 2007. URL: `http://fritzing.org/home/`.

[72] Osram Semiconductors. *Silicon PIN Photodiode.* 2016.

[73] Analog Devices. *Low Cost, 80 MHz FastFET ™ Op Amps AD8033/AD8034.*